

Electronic Theses and Dissertations, 2020-

2020

Study on Ductile Fracture with Anisotropic and Strain Rate Effects in Manufacturing Processes

Hao Pan
University of Central Florida

 Part of the [Mechanical Engineering Commons](#)
Find similar works at: <https://stars.library.ucf.edu/etd2020>
University of Central Florida Libraries <http://library.ucf.edu>

This Doctoral Dissertation (Open Access) is brought to you for free and open access by STARS. It has been accepted for inclusion in Electronic Theses and Dissertations, 2020- by an authorized administrator of STARS. For more information, please contact STARS@ucf.edu.

STARS Citation

Pan, Hao, "Study on Ductile Fracture with Anisotropic and Strain Rate Effects in Manufacturing Processes" (2020). *Electronic Theses and Dissertations, 2020-*. 264.
<https://stars.library.ucf.edu/etd2020/264>

STUDY ON DUCTILE FRACTURE WITH ANISOTROPIC AND STRAIN RATE EFFECTS IN
MANUFACTURING PROCESSES

by

HAO PAN

M.S. Masdar Institute of Science and Technology, UAE, 2012
B.S. Shandong University, China, 2010

A dissertation submitted in partial fulfillment of the requirements
for the degree of Doctor of Philosophy
in the Department of Mechanical and Aerospace Engineering
in the College of Engineering and Computer Science
at the University of Central Florida
Orlando, Florida

Summer Term
2020

Major Professor: Yuanli Bai

© 2020 Hao Pan

ABSTRACT

Ductile fracture is a topic of great importance in automotive and aerospace industries. Prediction of ductile fracture in engineering structures relies on developing robust material models under complex loading conditions. This dissertation addresses the anisotropic and strain rate effects in constitutive and ductile fracture models of lightweight metals. In the present modeling framework, the anisotropic plasticity behavior is modeled by combination of an initial anisotropic yield function and an isotropic hardening correction by Lode dependence. A new all-strain based anisotropic fracture model is proposed based on the approach of linear transformation on plastic strain rate tensor. The strain rate effects in ductile fracture is considered as an extension of the modified Mohr-Coulomb (MMC) fracture model by coupling strain rate with stress state in terms of Lode angle parameter. The rate-dependent MMC model provides a well-bound solution up to the intermediate strain rate range ($<1000/s$) for metal forming and crashworthiness applications. The present modeling framework is calibrated from coupon tests of aluminum alloy and advanced high strength steel (AHSS) sheets using digital image correlation (DIC) technique and validated through correlations by finite element (FE) simulations. This study also demonstrates the applications of ductile fracture modeling in manufacturing processes. The thermo-mechanical FE simulations of orthogonal cutting processes using the Johnson-Cook constitutive and damage models show that the highly damaged regions in zones of material separation form a thin boundary layer at the tool tip. The numerical simulation results explain the success of analytical model with uncoupled component works of plasticity, friction and separation. The FE modeling results of

formability and component-level testing suggest that part behavior and material failure is well predicted using calibrated ductile fracture models under different loading conditions.

KEYWORDS: Plasticity, Ductile Fracture, Anisotropy, Strain Rate, Finite Element Analysis, AHSS, Aluminum Alloys, Metal Forming, Machining

ACKNOWLEDGMENT

First and foremost, I would like to express my sincere gratitude to my academic advisor, Professor Yuanli Bai, for his guidance, encouragement, and patience through years of my PhD studies at Lab of Solid and Structure Mechanics (LSSM) at the University of Central Florida (UCF). I'm extremely grateful for his suggestions and daily discussions throughout my doctoral research. This dissertation would not have been possible without his persistent help. The funding supports from UCF and Auto/Steel Partnership (A/SP) are greatly appreciated.

For this dissertation, I gratefully acknowledge Professor Tony Atkins at the University of Reading for his guidance and discussions on the topic of mechanics and ductile fracture in metal cutting. I sincerely appreciate my Ph.D. committee members, Professor Alain Kassab, Professor Jihua Gou, and Professor Boo Hyun Nam for their valuable feedback on this dissertation.

I would also like to thank all my colleagues from the Lab of Solid and Structure Mechanics (LSSM). Particularly I would like to acknowledge Dr. Yueqian Jia and Dr. Yangyang Qiao, for their assistance of experimental and modeling work. I sincerely appreciate the research team at AK Steel for providing me with valuable industrial experience. Special thanks to Dr. Le Zhou, Dr. Xinke Xiao, Dr. Gang Huang for their collaboration on various research topics.

Lastly, I would like to thank my family for all their love, support and encouragement on this memorable journey.

TABLE OF CONTENTS

LIST OF FIGURES	x
LIST OF TABLES	xxi
CHAPTER 1 INTRODUCTION.....	1
1.1 Background	1
1.2 Motivation and Objectives	1
1.3 Outline of the thesis.....	2
CHAPTER 2 LITERATURE REVIEW.....	5
2.1 Anisotropic Plasticity Models	5
2.2 Anisotropic Fracture Models.....	8
2.3 Strain Rate Dependent Fracture Models	11
CHAPTER 3 ANISOTROPIC PLASTICITY AND FRACTURE MODELING OF ALUMINUM ALLOYS	14
3.1 Anisotropic Plasticity and Fracture Models.....	14
3.1.1 Definition of stress triaxiality η and Lode angle θ	15
3.1.2 Anisotropic plasticity model.....	16
3.1.3 Generalized anisotropic plastic flow parameter.....	18
3.1.4 Anisotropic fracture model eMMC-Srp.....	19
3.2 Experimental Results and Analysis.....	23
3.2.1 Uniaxial tension	24
3.2.2 Notch tension	25

3.2.3	Shear	26
3.2.4	Compression tests	28
3.2.5	Strain analysis in DIC	30
3.3	Calibration of Anisotropic Material Models	32
3.3.1	Equivalent stress-strain curve based on J2 plasticity	32
3.3.2	Calibration of anisotropic plasticity model with BW correction	34
3.3.3	Calibration of anisotropic fracture model	39
3.4	Finite Element Analysis	43
3.4.1	Uniaxial tension	43
3.4.2	Notch tension	44
3.4.3	Shear	47
3.4.4	Summary of strain path to fracture	49
3.5	Discussions.....	50
CHAPTER 4 STRAIN RATE DEPENDENT FRACTURE MODELING OF ADVANCED HIGH STRENGTH STEELS		53
4.1	Experimental results and analysis	53
4.1.1	Experiments at quasi-static and high-speed conditions	54
4.1.2	Experimental results of fracture strain.....	57
4.2	Rate-dependent MMC model and fracture strain analysis.....	65
4.3	Finite element analysis.....	74
4.3.1	FE simulation results of high-speed tests of QP980 sheets	74
4.3.2	FE simulation results of MP980, DP1180 and PHS1300	78

4.4	Discussions.....	86
CHAPTER 5 ZONES OF MATERIAL SEPARATION IN CUTTING SIMULATIONS		87
5.1	Algebraic and slip line field analysis	87
5.2	Review of FEM modeling.....	90
5.3	Finite element model.....	95
5.4	Material constitutive model.....	97
5.5	Finite element simulation results.....	102
5.5.1	Forces	102
5.5.2	Deformation fields of stress, strain and temperature	103
5.5.3	Separation zones	108
5.5.4	Conversion of incremental tool tip work into fracture toughness values	112
5.6	Comparison with algebraic models.....	114
5.7	Discussions and summary	124
CHAPTER 6 APPLICATIONS OF DUCTILE FRACTURE MODELING IN METAL FORMING PROCESSES		129
6.1	Formability and fracture tests.....	130
6.1.1	Square punch tests.....	130
6.1.2	Nakazima and three-point bending tests.....	132
6.2	Material model calibration	134
6.2.1	Material model	134
6.2.2	GISSMO fracture model in LS-DYNA	139
6.3	Finite Element Simulations	142

6.3.1	Finite element model setup	142
6.3.2	FE Simulations of Square Punch Tests	144
6.3.3	FE Simulations of Nakazima and three-point bending Tests.....	149
CHAPTER 7 CONCLUSIONS AND FUTURE STUDIES		153
REFERENCES		156

LIST OF FIGURES

Figure 3-1. Definition of anisotropic parameter ϕ and its relationship with stress triaxiality η based on J2 plasticity (courtesy of (Jia & Bai, 2016b)).....	19
Figure 3-2. Test specimens cut from the 7075 aluminum alloy sheet	23
Figure 3-3. Uniaxial tension test results (a) engineering stress-strain (b) Lankford ratio (r-value)	24
Figure 3-4. Notch tension test results (a) force-displacement curves (b) local strain paths at the notch center	26
Figure 3-5 Shear test results (a) force-displacement curves (b) local strain paths from the shear zone center	27
Figure 3-6. Experimental results of (a) uniaxial compression test (b) through-thickness compression test.....	30
Figure 3-7. Strain paths to fracture in the space of $\epsilon p - \phi$ from uniaxial tension, notch tension and shear tests	31
Figure 3-8. Contour plots of the plastic flow parameter ϕ in the DIC software VIC-2D	32
Figure 3-9. von Mises equivalent stress-equivalent plastic strain curves (a) uniaxial tension and shear (c) uniaxial tension and uniaxial compression	33
Figure 3-10. von Mises equivalent stress-plastic strain curves for all loading conditions along rolling direction.....	34
Figure 3-11. Yld2000-2d initial yield locus of Al7075 aluminum alloy sheet.....	35
Figure 3-12. Swift-Voce hardening curve law for extrapolation after necking.....	36

Figure 3-13. Lode dependence parameter $c\theta_s$ as evolution of equivalent plastic strain ϵ_p	37
Figure 3-14. Evolution of hardening curve Yld2000-2d model with and without BW plasticity model correction	38
Figure 3-15. Evolution of Yld2000-2d yield locus with BW plasticity model correction	38
Figure 3-16. Anisotropic fracture model eMMC-Srp: Srp48, Srp93 and Srp2004. The solid line represents the eMMC fracture locus. The red markers denote the fitting results using isotropic coefficients in a strain rate potential function. The blue markers denote the fitting results using optimized anisotropic coefficients in a strain rate potential function.	42
Figure 3-17. FE simulations of uniaxial tension: engineering stress-strain curve	44
Figure 3-18. FE simulation results of uniaxial tension: anisotropic plastic flow measure angle ϕ (SDV18).....	44
Figure 3-19. FE simulations of notch tension (a) using Yld2000 only (b) using Yld2000 and BW plasticity correction.....	46
Figure 3-20. FE simulation results from notch tension tests along rolling direction (SDV1: equivalent plastic strain)	46
Figure 3-21. FE simulation results of shear test along RD using Yld2000 and BW plasticity model correction.	48
Figure 3-22. FE simulation results of shear test (a) contour plot of equivalent plastic strain (SDV1) (b) contour plot of damage parameter D (SDV3) (c) Fracture initiation in the shear zone	49
Figure 3-23. FEA results of strain paths to fracture for uniaxial tension, plane strain tension and shear tests	50

Figure 3-24. Mesh size effect in FE simulations of (a) shear test (b) uniaxial tension test. 51

Figure 4-1. Schematic drawings of specimens tested under quasi-static conditions for MP980, DP1180 and PHS1300. (1) UT: uniaxial tension (2) UH: uniaxial tension with central hole (3) NT: notch tension (4) SH: shear (5) BX: biaxial punch (6) BE: plane strain bending (7) BU: hydraulic bulging. 54

Figure 4-2. Schematic drawings of specimens tested under high-speed conditions for MP980, DP1180 and PHS1300. (1) UT: uniaxial tension (2) BE: plane strain bending (3) BX: biaxial punch. 55

Figure 4-3. Schematic drawings of specimens tested under quasi-static and high-speed conditions for QP980. (a)(b) UT: uniaxial tension (c) NT: notch tension (d) SH: shear (e) BX: biaxial punch 55

Figure 4-4. Strain paths for QP980 steel sheets at quasi-static, slow-speed and high-speed dynamic tests under different loading conditions (from left to right): (1) shear (2) uniaxial tension (3) notch tension (4) Nakazima punch test..... 58

Figure 4-5. Strain paths to fracture for all 7 types of quasi-static tests of MP980: (1) SH: shear (2) UH: uniaxial tension with central hole (3) UT: uniaxial tension (4) NT: notch tension (5) BE: plane strain bending (6) BU: hydraulic bulging (7) BX: biaxial punch. The test results are along rolling direction of the samples..... 59

Figure 4-6. Strain paths to fracture for all 7 types of quasi-static tests of DP1180: (1) SH: shear (2) UH: uniaxial tension with central hole (3) UT: uniaxial tension (4) NT: notch tension (5) BE: plane strain bending (6) BU: hydraulic bulging (7) BX: biaxial punch. The test results are along rolling direction of the samples..... 59

Figure 4-7. Strain paths to fracture for all 7 types of quasi-static tests of PHS1300: (1) SH: shear (2) UH: uniaxial tension with central hole (3) UT: uniaxial tension (4) NT: notch tension (5) BE: plane strain bending (6) BU: hydraulic bulging (7) BX: biaxial punch. The test results are along rolling direction of the samples..... 60

Figure 4-8. Fracture strain for high-speed uniaxial tests of MP980 (a) fracture strain from physical measurement (b) fracture strain from physical measurement of bending (BE) and punch (BX) tests (c) fracture strain from physical measurement of uniaxial tension (UT) tests (d) fracture strain from DIC analysis of uniaxial tension (UT) tests..... 62

Figure 4-9. Fracture strain for high-speed uniaxial tests of DP1180 (a) fracture strain from physical measurement (b) fracture strain from physical measurement of bending (BE) and punch (BX) tests (c) fracture strain from physical measurement of uniaxial tension (UT) tests (d) fracture strain from DIC analysis of uniaxial tension (UT) tests..... 63

Figure 4-10. Fracture strain for high-speed uniaxial tests of PHS1300 (a) fracture strain from physical measurement (b) fracture strain from physical measurement of bending (BE) and punch (BX) tests (c) fracture strain from physical measurement of uniaxial tension (UT) tests (d) fracture strain from DIC analysis of uniaxial tension (UT) tests..... 64

Figure 4-11. Fracture model plot for QP980: (a) MMC fracture locus at quasi-static condition (b) Fracture forming limit diagram (FFLD) at quasi-static and dynamic conditions in strain space (c) S-curve model $g(\epsilon)$ from quasi-static to intermediate strain rate and comparison with Johnson-Cook model (d) Lode angle coupling term $h\theta$ in Eq.(4-5)..... 68

Figure 4-12. 3D fracture envelopes of QP980 under plane stress condition (a) Fully uncoupled rate-dependent MMC fracture model by Eq.(4-4). (b) Coupled rate-dependent MMC fracture model by replacing Eq.(4-4) with Eq.(4-6).....	69
Figure 4-13. Full decoupled S-curve model $g(\varepsilon)$ of MP980, DP1180 and PHS1300 from quasi-static to intermediate strain rate conditions	70
Figure 4-14. Fracture forming limit diagram (FFLD) of MP980 at (1) Quasi-static (QS) (2) Low strain rate and (3) Intermediate strain rate conditions. Strain ratio $\alpha = d\varepsilon_2/d\varepsilon_1$	71
Figure 4-15. MMC fracture locus of MP980 at (1) Quasi-static (QS) (2) Low strain rate and (3) Intermediate strain rate conditions.....	71
Figure 4-16. Fracture forming limit diagram (FFLD) of DP1180 at (1) Quasi-static (QS) (2) Low strain rate and (3) Intermediate strain rate conditions. Strain ratio $\alpha = d\varepsilon_2/d\varepsilon_1$	72
Figure 4-17. MMC fracture locus of DP1180 at (1) Quasi-static (QS) (2) Low strain rate and (3) Intermediate strain rate conditions.....	72
Figure 4-18. Fracture forming limit diagram (FFLD) of PHS1300 at (1) Quasi-static (QS) (2) Low strain rate and (3) Intermediate strain rate conditions. Strain ratio $\alpha = d\varepsilon_2/d\varepsilon_1$	73
Figure 4-19. MMC fracture locus of PHS1300 at (1) Quasi-static (QS) (2) Low strain rate and (3) Intermediate strain rate conditions.....	73
Figure 4-20. FEA results of (left) uniaxial tension and (right) punch tests of QP980 sheets at different speeds	76
Figure 4-21. FEA results of rate-dependent loading paths to fracture of QP980 for uniaxial tension (solid lines) and punch (dashed lines) tests at 3 different speeds: quasi-static (black),	

slow speed (green) and high speed (red). Note that the strain rate range for the highest speed of uniaxial tension (intermediate ϵ) is different than punch test (low ϵ). 78

Figure 4-22. An example (MP980) of rate-dependent hardening curve input by *MAT_224 in LS-DYNA 79

Figure 4-23. FEA results of high speed tests in uniaxial tension at different target nominal strain rates for MP980. The test results are shown in solid lines and the FEA results are shown in dashed lines. 80

Figure 4-24. FEA results of high speed tests in uniaxial tension at different target nominal strain rates for DP1180. The test results are shown in solid lines and the FEA results are shown in dashed lines. 81

Figure 4-25. FEA results of high speed tests in uniaxial tension at different target nominal strain rates for PHS1300. The test results are shown in solid lines and the FEA results are shown in dashed lines. 81

Figure 4-26. FEA results of high speed bending tests for MP980 at punch velocity of (a) 50 mm/s and (b) 100 mm/s. The test results are shown in color lines and the FEA results are shown in black lines. 82

Figure 4-27. FEA results of high speed bending tests for DP1180 at punch velocity of 50 mm/s. The test results are shown in color lines and the FEA results are shown in black lines. 83

Figure 4-28. FEA results of high speed bending tests for PHS1300 at punch velocity of 50 mm/s. The test results are shown in color lines and the FEA results are shown in black lines. 83

Figure 4-29. FEA results of high speed punch tests for MP980 at punch velocity of (a) 50 mm/s and (b) 100 mm/s. The test results are shown in solid lines and the FEA results are shown in dashed lines.	84
Figure 4-30. FEA results of high speed punch tests for DP1180 at punch velocity of (a) 50 mm/s and (b) 100 mm/s. The test results are shown in solid lines and the FEA results are shown in dashed lines.	85
Figure 4-31. FEA results of high speed punch tests for PHS1300 at punch velocity of (a) 50 mm/s and (b) 100 mm/s. The test results are shown in solid lines and the FEA results are shown in dashed lines.	85
Figure 5-1. Piispanen’s ‘deck of cards’ model. If slip occurs in plane strain in a finite width band along the primary shear plane, plastic volume cannot be conserved unless a gap occurs in the region of XY. Otherwise ZWV is an increase in plastic volume (Atkins, 2009) (adapted from (Cook et al., 1954)).	87
Figure 5-2. Configuration and boundary condition of the FEM model for orthogonal cutting simulations in this study.	96
Figure 5-3. Flow chart of the user material subroutine VUMAT in Abaqus/Explicit	101
Figure 5-4. cutting force vs. tool travel distance at different depths of cut and rake angles	104
Figure 5-5. von Mises stress distribution of chip formations at different rake angles and selected depths of cut.	106
Figure 5-6. Equivalent plastic strain distribution of chip formations at different rake angles and selected depths of cut. Blue means 0 and red means 1.0	107
Figure 5-7. Temperature distribution in three representative chip types (unit: K)	108

Figure 5-8. Damage distribution on the contour plot of deformed shape at different rake angles and selected depths of cut. Blue means 0 and red means 1.0.	110
Figure 5-9. Damage distribution on the contour plot of undeformed shape ($t_0 = 0.3 \text{ mm}$).....	111
Figure 5-10. Evolutions of plastic strain, stress triaxiality and damage indicator for an element on the underside of the chip ($\alpha = 40^\circ$, $t_0 = 0.25 \text{ mm}$)	111
Figure 5-11. A representation of highly-deformed boundary layer on the contour plot of damage distribution at cutting instant of (a)150 μs (b)200 μs . Figures on the right shows an extruded 3D representation of the model.....	113
Figure 5-12. FEM simulation result of averaged incremental plastic strain energy density (dU_{pl}) $_{avg}$ at each depth of cut and rake angle in cases of continuous chip formation	114
Figure 5-13. An iterative process of determination of shear angle ϕ , rigid-plastic yield stress τ_y , and specific work of surface formation R in the algebraic model from F_c vs. t_0 plot	116
Figure 5-14. Cutting force F_c vs. depth of cut t_0 plot and linear curve fitting within the regime of continuous chip formation only	118
Figure 5-15. A comparison of shear angle ϕ between calculations from analytical model and measurements from FE simulations.....	118
Figure 5-16. Analytical results of (a) shear strain γ (b) friction correction parameter Q (c) ratio γ/Q with respect to different depths of cut t_0 at each rake angle α	119
Figure 5-17. (a) Elements along primary shear plane were used for calculating the shear yield stress τ_y (b) Comparison of shear yield stress τ_y between FEM simulations and analytical model	120

Figure 5-18. (a) Boundary layer zone on a contour plot of deformed shape. Sublayer (2) is invisible due to element deletion. (b) An upper-bound value of h ($60\ \mu\text{m}$) in the boundary layer zone. The boundary layer zone contains three sublayers on the contour plot of undeformed shape. 122

Figure 5-19. Comparison of specific work of new surface formation R (fracture toughness) between simulation results and analytical solutions using three h values. The magnitude of error bar at each rake angle indicates the range of R at different t_0 converted from $(dU_{pl})_{avg}$ in simulations. 123

Figure 5-20. (a) Damage evolution and chip morphology in the present study ($\alpha = 17.5^\circ$, $V_c = 800\ \text{m/min}$) (b) FEM simulation result of damage evolution in Mabrouki et al. (2008) (c) chip morphology in real experiment ($t_0 = 0.4\ \text{mm}$, $V_c = 800\ \text{m/min}$) in Mabrouki et al. (2008).. 124

Figure 5-21. Friction coefficient μ calculated from Atkins algebraic model for all α and t_0 125

Figure 5-22. Proportions of plasticity, friction and fracture work at rake angle $\alpha = 30^\circ$ 126

Figure 6-1. (a) Schematic diagram of the square punch test (front view) (b) top view of square punch test with 0° sheet orientation (c) top view of square punch test with 45° sheet orientation 131

Figure 6-2. Strain paths to fracture of Nakazima tests of QP980 133

Figure 6-3. (a) B-pillar bending example (2016 Tesla Model S side IIHS crash test) (b) an example of three-point bending test on a hat section sample 134

Figure 6-4. (a) Illustration of the post-critical regime after necking in the engineering stress-strain curve (b) an example of post-necking extrapolation by combined Swift-Voce law..... 136

Figure 6-5. The MMC fracture locus and the fracture forming limit diagram (FFLD) calibrated from uniaxial tension and square punch tests of DP780 sheets.	138
Figure 6-6. The MMC fracture locus and the fracture forming limit diagram (FFLD) of QP980 sheets.	138
Figure 6-7. Demonstration of a simplified stress softening and damage accumulation for QP980 in GISSMO. The material instability and fracture strain are simplified as a fixed value of $ECRIT = 0.16$ and $\epsilon_f = 0.4$. Non-linear damage accumulation exponent $n = 2$ and exponent for damage-related stress fadeout $FADEXP = 2$. The softening factor is the term in the bracket of Eq. (6-15).	141
Figure 6-8. An example of MMC fracture locus and Swift instability curve of QP980 in GISSMO	142
Figure 6-9. Finite element analysis and experimental results of square punch tests for case DP-0. Fracture initiates at the corner of punch radius. PEEQ denotes the equivalent plastic strain.	145
Figure 6-10. Finite element analysis and experimental results of square punch tests for case DP-45. Fracture initiates at the corner of die radius. PEEQ denotes the equivalent plastic strain. ..	145
Figure 6-11. Experimental and numerically predicted force-displacement curves for test case DP-45 and DP-0.	145
Figure 6-12. Illustration of the mechanism of generating in-plane shear in square punch test. .	146
Figure 6-13. Strain histories extracted from the critical element at fracture initiation site for the case of (a) green: DP-45 (b) blue: DP-0 (c) orange: uniaxial tension in the space of principal strain. The solid, dashed and dotted lines represent the integration point on the middle, positive and negative surface, respectively.	147

Figure 6-14. Damage evolution of the three integration points through thickness extracted from the critical element for case DP-45 and DP-0. The solid, dashed and dotted lines represent the integration point on the middle, positive and negative surface, respectively.	148
Figure 6-15. Thickness history of the critical element for case DP-0 and DP-45.	149
Figure 6-16. FE simulation results of Nakazima Tests of QP980 sheets.....	150
Figure 6-17. (a) Fracture samples in Nakazima Test (b) Fracture in FE simulations (c) Equivalent plastic strain contour plot before fracture	151
Figure 6-18. Three-point bending of hat section (a) using cylinder punch (b) using cross-punch. The different punch design demonstrates the use of GISSMO damage model for stress state dependent fracture modeling in LS-DYNA.....	152

LIST OF TABLES

Table 3-1. Yld2000-2d anisotropic yield function parameters for Al7075-T6.....	35
Table 3-2. Anisotropic fracture model parameters for Al7075-T6.....	40
Table 4-1. AHSS sheets investigated in the present study.....	53
Table 4-2. Fracture test summary of AHSS sheets at quasi-static and high-speed conditions.....	57
Table 4-3. Local fracture strain estimation from physical measurements	60
Table 4-4. Plasticity and fracture parameters for QP980 steel	75
Table 4-5. Plasticity and fracture parameters for MP980, DP1180 and PHS1300.....	79
Table 5-1. Johnson-Cook plasticity parameter values for AA2024-T351	97
Table 5-2. Physical properties of the workpiece material AA2024-T351	98
Table 5-3. Material parameters in Johnson-Cook damage model	99
Table 6-1. Summary of square punch tests on DP780 sheet.....	132
Table 6-2. Isotropic hardening parameters of DP780 and QP980	136
Table 6-3. MMC fracture model parameters for DP780 and QP980.....	139

CHAPTER 1 INTRODUCTION

1.1 Background

In automotive industry, significant efforts are being put forth to design lightweight vehicles to meet fuel economy requirements. The applications of lightweight alloy materials in automotive structures offer great potentials for mass reduction while maintaining strength and other performance properties. Advanced high strength steels (AHSS) are widely used in automotive industry attributed to their better performance in crash energy management and significant achievement in mass reduction. AHSS are less ductile than conventional steels, which imposes challenges on accurate prediction of material fracture under different loading conditions. This, in turn, requires accurate material models throughout the part loading history at elevated strain rates, ranging from a typical strain rate of 10/s in stamping practices, to approximately 1000/s in full vehicle crash events (Keeler & Kimchi, 2015). For aluminum alloy sheets, material anisotropy has an important effect on sheet formability in the process chain. The key in improving the modeling accuracy of aluminum sheet forming processes and structural performance in design relies on accurate anisotropic plasticity and fracture models under multi-axial loading conditions.

1.2 Motivation and Objectives

In the last decade, various state-of-the-art ductile fracture models were developed with considerable effort on investigating the relation between fracture strain and multi-axial stress state under isotropic and quasi-static condition. The current work extends the isotropic modified Mohr-Coulomb (MMC) stress-state dependent ductile fracture model with anisotropic and strain rate effects. The discussion in this work is limited to the scope of macroscopic phenomenological

modeling of a crack free body. The micromechanics modeling frameworks based on the micro-void theory and continuum damage mechanics are beyond the scope of this thesis and hence not discussed.

The present thesis work includes analytical models, experimental studies, and finite element (FE) simulations. In experiments, different types of coupon samples were designed and tested over a wide range of loading conditions. The digital image correlation (DIC) technique was used for full field measurement of displacement and strain analysis. The analytical models are proposed from the experimental findings. FE simulations are used to predict the deformation fields of parts and validate material models by comparing the global load-displacement responses and local fracture modes with experimental results. The overview of this thesis is summarized as follows:

- Develop an integrated anisotropic modeling approach under multi-axial stress states, including anisotropic yield, anisotropic hardening and anisotropic fracture.
- Develop a new strain rate dependent fracture model for dynamic loading event up to the intermediate strain rate range, including the coupling effect of strain rate and stress state.
- Demonstrate the application of ductile fracture in manufacturing processes by predicting the deformation field and ductile fracture under complex part loading conditions.

1.3 Outline of the thesis

The present thesis consists of seven chapters. Chapter 1 gives a brief introduction of the background, motivations and objectives of the thesis. Chapter 2 reviews the phenomenological models of anisotropic plasticity and fracture, and strain rate dependent ductile fracture models.

Chapter 3 develops an anisotropic modeling framework for aluminum alloys. The anisotropic plasticity and fracture behaviors of 7075 aluminum alloy sheets are investigated by both experiments and finite element (FE) simulations. Different sheet samples were designed and tested under various loading conditions along three material directions. The full field displacement and strain was measured and analyzed by the digital image correlation (DIC) technique. The anisotropic plasticity is modeled by the Yld2000-2d yield function with flow stress correction by Lode dependence. For anisotropic fracture, the strain rate potential functions are revisited, and the methodology of linear transformation is used for developing the all-strain based anisotropic fracture model. The FE simulation results using shell elements demonstrate that the current modeling method offers a simple and efficient solution for solving anisotropic problems of aluminum alloys under proportional loading conditions.

Chapter 4 proposes a new strain rate dependent ductile fracture model. The model was developed based on comprehensive experimental data analysis on several grades of AHSS sheets under quasi-static and high speed test conditions. The original modified Mohr-Coulomb (MMC) fracture model is extended with a strain rate dependent term either fully uncoupled or coupled with stress-state characterized by Lode angle. The new rate-dependent MMC model provides a bounded solution for modeling rate-dependent fracture problems up to the intermediate strain rate range for stamping and crash simulations. Finite element simulations are performed to correlate the test results under dynamic loading conditions.

Chapter 5 discusses the finite element analysis of the high speed orthogonal cutting process of 2024-T351 aluminum alloys using the Johnson-Cook constitutive and damage models. The 2D explicit dynamic simulations demonstrate that the damaged regions, in which separation of

material occurs at the tool tip, form thin boundary layers on the top of the machined surface and on the underside of the chip. The simulation results explain the success of variable-separable algebraic models of cutting with continuous chips in which the component works of chip plasticity, friction and separation are uncoupled. The FE simulations predict the same quasi-linear relation between the cutting force and the uncut chip thickness as in the analytical model of continuous chip cutting under the assumption of sharp tool tip. The fracture toughness and the size of the boundary layers of damage are shown to be quantitatively related.

Chapter 6 demonstrates the applications of ductile fracture modeling for predicting material failure in simulations of forming and component tests: (1) square punch tests (2) Nakazima tests and (3) three point bending tests of hat-sections. The square punch tests introduce a practical calibration approach of ductile fracture locus by transforming the stress-based fracture locus into the strain-based fracture forming limit diagram (FFLD) under the proportional loading assumption. Shear-induced fracture was correctly predicted which cannot be tackled by conventional forming limit diagram (FLD). The Nakazima tests and the three point bending tests validated the ductile fracture model calibration from the coupon tests. The applications of ductile fracture modeling demonstrate great potential as an engineering tool for industrial practices of formability tests and crashworthiness simulations.

Chapter 7 summaries the main contributions of the present thesis and suggests some topics for future research.

CHAPTER 2 LITERATURE REVIEW

2.1 Anisotropic Plasticity Models

Anisotropy of sheet metals indicates the directional dependence of mechanical properties due to their crystallographic structures from the rolling process. Three sources of anisotropy must be distinguished: (1) anisotropic yield, (2) anisotropic hardening, and (3) anisotropic fracture. The anisotropic yield of sheet metals has been extensively investigated in the past decades. Hill (1948) first proposed a quadratic anisotropic yield function for orthotropic materials. With the advent of more advanced steel alloys and non-ferrous metals, the Hill yield criterion was generalized with a non-quadratic form in principal stresses (Hill, 1979) and further developed for solving plane stress problems with planar anisotropy (Hill, 1990, 1993). Besides the Hill yield criteria family, the anisotropic yield functions are mainly developed based on the general approach of linear transformation. The Barlat anisotropic yield functions (Barlat et al., 2005; Barlat, Becker, et al., 1997; Barlat et al., 2003; Barlat, Lege, & Brem, 1991; Barlat & Lian, 1989; Barlat, Maeda, et al., 1997) were developed from the non-quadratic isotropic yield function proposed by Hosford (1972) and some were particularly intended for aluminum alloy sheets. Barlat and Lian (1989) proposed the Yld89 anisotropic yield function on a generalized tricomponent plane stress yield surface by introduction of shear stress component. Later, Barlat et al. (1991) proposed a six-component anisotropic yield criterion Yld91 for general stress states. In the meanwhile, Karafillis and Boyce (1993) proposed an original method of linear transformation to extend the proposed generalized isotropic yield function to an anisotropic yield function. The convexity was assured by the isotropic yield function and preserved by the linear transformation on Cauchy stress tensor. The

methodology of linear transformation by Karafillis and Boyce (1993) was further adopted to establish the anisotropic yield functions Yld94 and Yld96 (Barlat, Becker, et al., 1997; Barlat, Maeda, et al., 1997) tailored particularly for aluminum alloys. The convexity limitation of Yld96 leads to the development of Yld2000-2d (Barlat et al., 2003). The Yld2000-2d anisotropic yield function provides a simple formulation with two linear transformations on the Cauchy stress tensor for plane stress state. Using the same method, Yld2004-18p (Barlat et al., 2005) was proposed to describe the anisotropic behavior for general 3D stress states. The linear transformation-based anisotropic yield functions for FCC and BCC materials were reviewed and discussed in Barlat, Yoon, and Cazacu (2007). The approach of linear transformation was further extended to HCP metals by Cazacu, Plunkett, and Barlat (2006) to account for the strength differential effect and plastic deformation governed by both slip and twinning.

Instead of using stress potential functions, an alternative approach to describe material anisotropy is by strain rate potential functions. The strain rate potential can be approximated with analytic expressions by crystallographic analysis of polycrystals with cubic crystal structure (e.g. Arminjon, Bacroix, Imbault, and Raphanel (1994); (Rabahallah et al., 2009)). It is worth noting that analytic expressions of the strain rate potentials conjugated to stress potentials are available for simple yield functions such as von Mises, Tresca, Drucker-Prager, and the Hill anisotropic yield function (Cazacu, Ionescu, & Yoon, 2010). Despite that the conjugate strain rate potential can be derived from the corresponding yield stress potential by utilizing the principle of plastic work equivalence, it is very challenging to obtain a closed-form solution for non-quadratic yield functions. However, as formally identical to develop phenomenological yield functions, strain rate potential functions were developed in parallel to describe the anisotropic plastic flow as an

independent definition of the material behavior. Barlat and co-workers (Barlat & Chung, 1993); Barlat, Chung, and Richmond (1993); (Cazacu et al., 2010; Chung, Lee, Barlat, Keum, & Park, 1996; Kim et al., 2007; Kim, Lee, Barlat, Wagoner, & Chung, 2008) have proposed a series of non-quadratic anisotropic strain rate potentials (Srp) for orthotropic materials, which are named as Srp93, Srp98, Srp2003-2d, Srp2004-18p and Srp2006-18p. The non-quadratic strain rate potentials are pseudo-conjugate to the corresponding anisotropic yield stress potentials, Yld91, Yld96, Yld2000-2d and Yld2004-18p, respectively (Kim et al., 2008). The strain rate potentials have been also implemented in finite element analysis of forming simulations (e.g. (Yoon, Barlat, Dick, Chung, & Kang, 2004; Yoon, Song, Yang, Chung, & Barlat, 1995)), and results suggest comparable accuracy to those obtained by the stress potentials.

In sheet forming simulations, it appears a reasonable choice to define the constitutive model based on an anisotropic yield function and isotropic hardening. This is mainly because for industrial practices, the complexity of material model and computational time are two important factors to consider; while the deformation-induced anisotropy is small and negligible compared to the initial anisotropy induced by rolling and heat treatment (Yoon et al., 2004). However, the experimental results in tube hydroforming (Korkolis & Kyriakides, 2008a, 2008b) indicate that even under proportional loading condition, the deformation-induced anisotropy should be taken into account for more accurate description of yield surface evolution. Modeling of deformation-induced anisotropy in finite element code can be very complex if the crystallographic texture evolution is considered as a rigorous solution. The polycrystalline models (e.g. (Rousselier, Barlat, & Yoon, 2009, 2010)) are more appealing from a theoretical point of view, but the computational cost is high for practical forming analysis. The anisotropic hardening problem can be solved in a

variety of methods, such as the efforts in developing continuum models by changing the initial anisotropic parameters with plastic work (Ha, Baral, & Korkolis, 2018; Korkolis & Kyriakides, 2008a), or by defining a non-associated flow rule (Stoughton, 2002; Stoughton & Yoon, 2009). After the connection between loading conditions and Lode angle was discovered by Bai and Wierzbicki (2008), the anisotropic hardening problem can be potentially solved by correction of flow stresses with pressure and Lode dependence. Such a new modeling scheme is proposed in this work, with aim to provide a simple and flexible solution for monotonic loading conditions. More sophisticated constitutive models considering cross-hardening and Bauschinger effect under stress reversal conditions can be found in homogeneous anisotropic hardening (HAH) models (Barlat, Gracio, Lee, Rauch, & Vincze, 2011; Barlat et al., 2013).

2.2 Anisotropic Fracture Models

Unlike the advancement of anisotropic plasticity models in the last few decades, the research interest on developing anisotropic fracture models arises very recently. Here, the scope of discussion on fracture models is limited to the macroscopic phenomenological models. These models are calibrated based on an extensive test program on metal sheets or bulks and have become well-accepted in metal forming industry. One of the most comprehensive fracture tests was reported by Bao and Wierzbicki (2004) on aluminum alloy bulk material. Bai and Wierzbicki (2010) proposed the modified Mohr-Coulomb (MMC) fracture model by combined effects of normal stress and shear stress. The MMC fracture model reveals that other than the hydrostatic pressure effect, the Lode angle is another key factor controlling the ductile fracture. Since the MMC model, the early anisotropic fracture models were introduced to make use of the work-

conjugate anisotropic plastic strain rate in the fracture model. Such an anisotropic fracture model was proposed in (Beese, Luo, Li, Bai, & Wierzbicki, 2010) based on the closed-form solution of the Hill'48 anisotropic equivalent plastic strain rate within the MMC framework. The model partially-coupled the plasticity and fracture models by using the work-conjugate anisotropic plastic strain increment to calibrate the isotropic fracture locus in 2D space. Similarly, Luo, Dunand, and Mohr (2012) presented an anisotropic fracture model based on a work-conjugate Yld2000-3D equivalent plastic strain. The anisotropic MMC fracture envelop was associated with anisotropic plasticity model in the 3D space characterized by stress triaxiality and Lode angle calibrated along the extrusion direction. Both the partially-coupled (Beese et al., 2010) and the associated (Luo et al., 2012) anisotropic fracture models aim to provide a bridge between plasticity and fracture.

The development of anisotropic fracture models then diverges into two paths: (1) by linear transformation of strain or stress tensors and (2) by interpolation functions between multiple fracture loci. The methodology of linear transformation was first proposed by Luo et al. (2012) in the same paper introduced above. In close analogy to the anisotropic yield function, a non-associated anisotropic fracture model was proposed by linear transformation on plastic strain rate tensor. The linear transformation on strain tensors provides an effective solution for solving anisotropic fracture problems uncoupled from plasticity, particularly when the plasticity model is very complex. For example, in a comprehensive study of Magnesium alloy sheets by Jia and Bai (2016a, 2016b), the plasticity model is very complex including strong anisotropy and strength differential effect with sophisticated hardening behavior. Obviously, it is not efficient in practical for developing a coupled anisotropic fracture model to associate the plasticity features. Therefore, an all-strain-based anisotropic fracture locus eMMC was proposed in (Jia & Bai, 2016a, 2016b)

using a non-conjugated anisotropic equivalent plastic strain in the similar form of Hill'48 yield potential function. Inspired from the eMMC model, Lou and Yoon (2017) proposed an anisotropic ductile fracture criterion based on an isotropic damage equivalent strain increment from linear transformation of plastic strain increment. The isotropic damage equivalent strain defined by Lou and Yoon (2017) is in fact identical to the effective plastic strain rate in the strain rate potential defined for anisotropic materials proposed by Barlat et al. (1993). Similar idea of linear transformation has been pursued by other researchers based on the argument of stress tensor. Gu and Mohr (2015) proposed an anisotropic extension of the isotropic Hosford-Coulomb fracture model (developed by Mohr and Marcadet (2015)) by applying the linear transformation matrix on the normalized Cauchy stress tensor. The anisotropic effect on the fracture envelope was shown from the polar plots in $(\sigma_{11} - \sigma_{22})$ plane with radius of anisotropic equivalent plastic strain to fracture. The same approach of linear transformation on stress tensor was further explored in recent studies (Gu, He, Li, & Lin, 2020; Li et al., 2018) by extending the stress invariants based isotropic ductile fracture models to its anisotropic form.

The second group of anisotropic fracture models are developed based on interpolation (or weight) functions. The key idea is to apply an interpolation function among multiple fracture loci calibrated from different loading directions. The first part of work in this category is the anisotropic fracture models proposed in Park et al. (2017); Park, Huh, and Yoon (2018); Park, Stoughton, and Yoon (2020). Since the existing isotropic fracture models are stress invariant-based (e.g. (Bai & Wierzbicki, 2010; Luo et al., 2012; Mohr & Marcadet, 2015)), it is impossible to generate directional dependent fracture loci using the original definition of stress invariant. Therefore, Park et al. (2017) proposed an “anisotropic stress triaxiality” based on the anisotropic Hill'48 criterion

and incorporated it into the Lou-Huh isotropic fracture criterion (Lou, Yoon, & Huh, 2014). Subsequently, the “anisotropic stress triaxiality” was further extended to a more complex form in (Park et al., 2018) using the Yld2004-18p model. In both studies, the interpolation function proposed by Stoughton and Yoon (2011) was applied to the anisotropic fracture models, similarly as in the original study on forming limit diagram (FLD). The interpolation function was introduced as a function of the rotation angle θ_s which represents the direction from the maximum principal stress to the rolling direction. Park et al. (2020) proposed an anisotropic fracture modeling approach based on the decoupled formulation with the use of the magnitude of principal stress vector and the Lagrangian interpolation function. The second part of application of interpolation functions is the eGISSMO framework in LS-DYNA. Conceptually similar but essentially different to Park’s work, the modeling framework for anisotropic fracture in eGISSMO framework is treated as an anisotropic damage process. In eGISSMO, the isotropic fracture loci are calibrated from different directions along maximum principal stress, but damage accumulation is under material coordinate system. The method is based on decomposition of strain tensors with principal strains on three directions and interpolation functions, so that the fracture loci were limited to only three for plane stress application. Even though there are some potential open questions about the limitations, the eGISSMO model provides more possibilities open up with the simplicity of anisotropic fracture modeling.

2.3 Strain Rate Dependent Fracture Models

Over the years, there have been a large number of investigations carried out in understanding the integrated constitutive equations incorporating strain hardening with strain rate

and temperature effects. Reviews of existing visco-plasticity models in literature can be found in (Liang & Khan, 1999; Sung, Kim, & Wagoner, 2010). Strain rate effects on ductile fracture of metal sheets, on the other hand, is of equal importance as rate-dependent constitutive relations, but such effects have not been widely investigated. The main limiting factor is the inadequate amount of test data. Under quasi-static condition, the fracture strain requires not only a large number of tests under various stress states, but also accurate measurement of local fracture strain. Such experimental difficulties further arise in dynamic testing using servo-hydraulic testing machines or split Hopkinson pressure bar system.

The most well-known strain rate dependent fracture model is the Johnson-Cook (JC) model (Johnson & Cook, 1983). It was developed based on axisymmetric tension and torsion tests on bulk metals. The JC fracture model has found many applications, for example in modeling high velocity perforation problems (Teng & Wierzbicki, 2006). Khan and Liu (2012) proposed a stress-based magnitude of stress vector (MSV) fracture model by incorporating strain rate and temperature dependences for Al and Ti alloys. Both JC and MSV models only consider hydrostatic pressure effect on ductile fracture and neglect the influence of Lode angle. Recently, Roth and Mohr (2014) proposed a rate-dependent Hosford-Coulomb (H-C) fracture model for multi-axial stress states characterized by stress triaxiality and Lode angle. The term of strain rate dependency is incorporated into the fracture model in close analogy to the JC model. The proposed model was subsequently applied for modeling dynamic fracture of tensile samples of AHSS using split Hopkinson pressure bar system (Dunand & Mohr, 2017; Erice, Roth, & Mohr, 2018). The rate dependent H-C model is however, limited to a uniform scaling of quasi-static fracture locus without consideration of coupling effect with stress state. The strain rate coupling effect with

multi-axial stress state is firstly investigated by Walters (2009). A dynamic modified Mohr-Coulomb (MMC) fracture locus was extended with strain rate dependency in the form of the Cowper-Symonds law. The proposed model is developed based on dynamic Hasek test results using a drop tower. The important finding is that as strain rate increases, the fracture locus twists in a non-monotonic manner with respect to Lode angle. The conclusion about Lode angle coupling with strain rate on phenomenological ductile models in (Walters, 2009) is also supported by the findings in this study.

CHAPTER 3 ANISOTROPIC PLASTICITY AND FRACTURE MODELING OF ALUMINUM ALLOYS

In this chapter, the plasticity and fracture behavior of 7075 aluminum alloy sheets is investigated by both experiments and FE simulations. The anisotropic plasticity and fracture model framework are first introduced in Section 3.1, The anisotropic plasticity is modeled by the Yld2000-2d yield function with flow stress correction by Lode dependence. For anisotropic fracture, the strain rate potential functions are revisited, and the methodology of linear transformation is used for developing the all-strain based anisotropic fracture model. Section 3.2 describes the details of mechanical tests under various loading conditions: (1) uniaxial tension (2) notch tension (3) shear and (4) uniaxial compression, along 0° , 45° and 90° with respect to rolling direction of metal sheets. From the test results and digital image correlation (DIC) analysis, the anisotropic models are calibrated in Section 3.3. The present material model is implemented in a user-defined material subroutine using shell element for FE simulations. The FE simulation results in Section 3.4 demonstrate that the current modeling method offers a simple and efficient solution for solving anisotropic problems of aluminum alloys under proportional loading conditions.

3.1 Anisotropic Plasticity and Fracture Models

In this section, an anisotropic modeling framework is proposed for the anisotropic aluminum alloy sheets. In the current framework, anisotropic plasticity is modeled by the anisotropic yield function Yld2000-2d (Barlat et al., 2003) in combination of isotropic hardening with hydrostatic pressure and Lode angle corrections (Bai & Wierzbicki, 2008). For anisotropic fracture, inspired by the strain rate potential functions for describing anisotropic yield, a new

generalized all-strain based anisotropic fracture model is proposed based on the modified Mohr-Coulomb fracture locus (Bai & Wierzbicki, 2010) and linear transformations of plastic strain rates. In addition, the generalized anisotropic plastic flow parameter ϕ from previous studies (Jia & Bai, 2016b) is also introduced here as an integral part of the all-strain based anisotropic fracture model.

3.1.1 Definition of Stress triaxiality η and Lode angle θ

The definition of stress triaxiality and Lode angle will be used throughout this paper. Given the stress tensor $\boldsymbol{\sigma}$, the three stress invariants are defined by

$$\sigma_m = \frac{1}{3}I_1 = \frac{1}{3}(\sigma_1 + \sigma_2 + \sigma_3) \quad (3-1)$$

$$q = \bar{\sigma} = \sqrt{3J_2} = \sqrt{\frac{1}{2}[(\sigma_1 - \sigma_2)^2 + (\sigma_2 - \sigma_3)^2 + (\sigma_3 - \sigma_1)^2]} \quad (3-2)$$

$$r = \left(\frac{27}{2}J_3\right)^{1/3} = \left[\frac{27}{2}(\sigma_1 - \sigma_m)(\sigma_2 - \sigma_m)(\sigma_3 - \sigma_m)\right]^{1/3} \quad (3-3)$$

where σ_1 , σ_2 , and σ_3 denote the principal stresses, I_1 is the first invariant of the stress tensor $\boldsymbol{\sigma}$, and J_2 and J_3 are the second and third invariants of the deviatoric stress tensor \boldsymbol{s} . The stress triaxiality η is defined as the normalized first stress invariant $\eta = \sigma_m/\bar{\sigma}$. The Lode angle θ is related to the normalized third deviatoric stress invariant through

$$\xi = \left(\frac{r}{q}\right)^3 = \cos(3\theta) \quad (3-4)$$

The Lode angle θ is normalized in Bai and Wierzbicki (2008),

$$\bar{\theta} = 1 - \frac{6\theta}{\pi} \quad (3-5)$$

The parameter $\bar{\theta}$ is called the Lode angle parameter. The range of the Lode angle θ is $0 \leq \theta \leq \pi/3$, and the range of the $\bar{\theta}$ is $-1 \leq \bar{\theta} \leq 1$.

3.1.2 Anisotropic Plasticity Modeling Framework

The anisotropic yield function with generalized hardening rule with pressure and Lode angle dependence is in the form of

$$f = \bar{\sigma}_{Yld2000} - \bar{\sigma}_{BW} \quad (3-6)$$

The Yld2000-2d anisotropic equivalent stress is

$$\bar{\sigma}_{Yld2000} = \left\{ \frac{1}{2} (|\tilde{S}'_1 - \tilde{S}'_2|^a + |2\tilde{S}''_2 + \tilde{S}''_1|^a + |2\tilde{S}''_1 + \tilde{S}''_2|^a) \right\}^{1/a} \quad (3-7)$$

In Eq.(3-7), $\tilde{S}'_1, \tilde{S}'_2$ and $\tilde{S}''_1, \tilde{S}''_2$ are principal values of stress tensor $\tilde{\mathbf{s}}'$ and $\tilde{\mathbf{s}}''$, respectively.

The stress tensor $\tilde{\mathbf{s}}$ is from a linear transformation of the Cauchy stress tensor $\boldsymbol{\sigma}$, by $\tilde{\mathbf{s}}' = \mathbf{L}'\boldsymbol{\sigma}$ and $\tilde{\mathbf{s}}'' = \mathbf{L}''\boldsymbol{\sigma}$. The linear transformation matrix \mathbf{L}' and \mathbf{L}'' contain the 8 anisotropic coefficients $\alpha_{1\sim 8}$.

$$[\mathbf{L}'] = \begin{bmatrix} L'_{11} & L'_{12} & 0 \\ L'_{21} & L'_{22} & 0 \\ 0 & 0 & L'_{66} \end{bmatrix} = \frac{1}{3} \begin{bmatrix} 2\alpha_1 & -\alpha_1 & 0 \\ -\alpha_2 & 2\alpha_2 & 0 \\ 0 & 0 & 3\alpha_7 \end{bmatrix} \quad (3-8)$$

$$[\mathbf{L}''] = \begin{bmatrix} L''_{11} & L''_{12} & 0 \\ L''_{21} & L''_{22} & 0 \\ 0 & 0 & L''_{66} \end{bmatrix} \quad (3-9)$$

$$= \frac{1}{9} \begin{bmatrix} 8\alpha_5 - 2\alpha_3 - 2\alpha_6 + 2\alpha_4 & 4\alpha_6 - 4\alpha_4 - 4\alpha_5 + \alpha_3 & 0 \\ 4\alpha_3 - 4\alpha_5 - 4\alpha_4 + \alpha_6 & 8\alpha_4 - 2\alpha_6 - 2\alpha_3 + 2\alpha_5 & 0 \\ 0 & 0 & 9\alpha_8 \end{bmatrix}$$

The Yld2000-2d anisotropic equivalent stress describes only the initial yield anisotropy. In order to accommodate the effects of loading conditions on evolution of yield surface, the pressure and Lode angle dependent correction terms are suggested to incorporate into the isotropic

hardening function (Bai & Wierzbicki, 2008). The Bai-Wierzbicki equivalent yield stress $\bar{\sigma}_{BW}$ is in the form of

$$\begin{aligned}\bar{\sigma}_{BW} &= \sigma_0(\bar{\varepsilon}^p)h(\eta, \theta) \\ &= \sigma_0(\bar{\varepsilon}^p)\left[1 - c_\eta(\eta - \eta_0)^2\right]\left[c_\theta^s - \frac{m+1}{m}(c_\theta^{ax} - c_\theta^s)\left(\gamma - \frac{\gamma^{m+1}}{m+1}\right)\right]\end{aligned}\quad (3-10)$$

The first term $\sigma_0(\bar{\varepsilon}^p)$ in Eq.(3-10) defines the isotropic hardening function calibrated from a reference test. In practice, it is common to use the hardening curve from a uniaxial tension test extrapolated by a linear combination of Swift-Voce law using a weighting factor, as shown in Eq.(3-11)

$$\sigma_0(\bar{\varepsilon}_p) = \alpha[A(\varepsilon_0 + \bar{\varepsilon}_p)^n] + (1 - \alpha)[k_0 + Q(1 - e^{-\beta\bar{\varepsilon}_p})] \quad (3-11)$$

The second term $h(\eta, \theta)$ in Eq.(3-10) defines the flow stress correction term dependent on the stress triaxiality η and the Lode angle θ . Note that $h(\eta, \theta)$ is slightly modified from the original model of Bai and Wierzbicki (2008), by adding a constant of $(m+1)/m$ to ensure $h(\eta, \theta) = 1$ when using uniaxial tension as the reference. The parameter γ is a function of the Lode angle θ defined by

$$\gamma(\theta) = \frac{\cos(\pi/6)}{1 - \cos(\pi/6)} \left[\frac{1}{\cos(\theta - \pi/6)} - 1 \right] \quad (3-12)$$

The Lode angle θ is defined through the normalized third deviatoric stress invariant in Eq.(3-4). The term $\cos(\theta - \pi/6)$ in the definition of parameter γ represents the difference between von Mises and Tresca in the deviatoric stress plane. Since the range of Lode angle θ is $0 \leq \theta \leq \pi/3$, γ is bounded between zero and unity. $\gamma = 0$ is corresponding to plane strain or shear condition, and $\gamma = 1$ corresponds to the axial symmetry loading condition.

In Eq.(3-10), c_η , η_0 , c_θ^s , c_θ^{ax} and m are material constants. As will be shown in the next sections, if only using the initial anisotropic yield, the results overestimated the force predictions for shear and notch tension tests. This can be solved by defining the Lode angle dependent term c_θ^s as an evolutionary function of equivalent plastic strain. The present anisotropic framework provides a flexible and elegant solution for solving anisotropic hardening problems of metal sheets under proportional loading. Particularly in finite element simulations, the benefit of this method becomes apparent compared to other methods such as changing the anisotropic coefficients (e.g. (Korkolis & Kyriakides, 2008a)) or the exponential term in the non-quadratic yield function (e.g. (Ha et al., 2018)) with the evolution of plastic work.

3.1.3 Generalized Anisotropic Plastic Flow Parameter

In our recent work (Jia & Bai, 2016b), a new plastic strain based parameter ϕ was defined to represent the effect of in-plane anisotropic flow under all loading conditions.

$$\phi = \frac{180^\circ}{\pi} \text{atan2}(-\dot{\epsilon}_2^p, \dot{\epsilon}_1^p) + 90^\circ \quad (3-13)$$

The parameter ϕ denotes the angle of strain path to the positive minor strain direction in the forming fracture limit diagram (FFLD). Figure 3-1 illustrates the definition of ϕ for describing plastic flow under the assumption of isotropic J2 plasticity. For an anisotropic material deformed under a specific loading condition, the anisotropic plastic flow is measured by an angle offset from the isotropic condition. For example, for the uniaxial tension test results, $\phi = 110^\circ, 112^\circ, 116^\circ$ for the rolling, diagonal and transverse direction, respectively. The corresponding Lankford ratio is $r_0 = 0.575$, $r_{45} = 0.755$, and $r_{90} = 0.990$. For the rolling direction, the angle offset is -6° , indicating

strong anisotropic effect similar as the Lankford ratio. Unlike the Lankford ratio only defined for uniaxial tension, the parameter ϕ describes the generalized anisotropic in-plane plastic flow under all possible loading conditions. The parameter ϕ represents an attractive option in developing an all-strain-based anisotropic fracture model: (1) it overcomes the limitations of assuming an anisotropic yield function in coupling with the stress invariant-based anisotropic fracture models, such as in Park et al. (2017); Park et al. (2018). (2) the all strain-based anisotropic fracture model can be directly calibrated from strain analysis in the DIC software, which is important for practical applications.

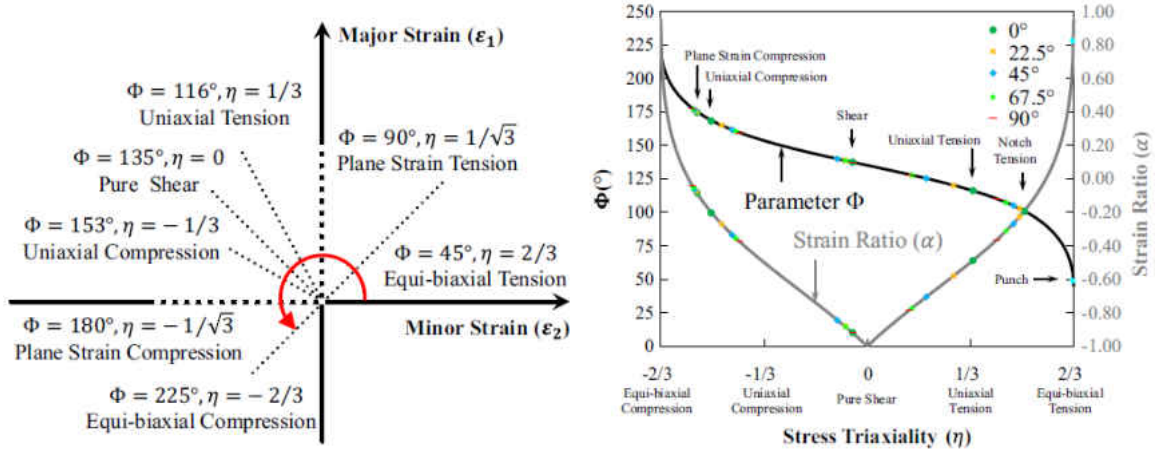


Figure 3-1. Definition of anisotropic parameter ϕ and its relationship with stress triaxiality η based on J2 plasticity (courtesy of (Jia & Bai, 2016b))

3.1.4 Anisotropic Fracture Model eMMC-Srp

The original modified Mohr-Coulomb (MMC) fracture locus based on work of (Bai & Wierzbicki, 2010) reads

$$\bar{\epsilon}_f(\eta, \bar{\theta}) = \left\{ \frac{A}{C_2} \left[C_\theta^s + \frac{\sqrt{3}}{2 - \sqrt{3}} (C_\theta^{ax} - C_\theta^s) \left(\sec \frac{\bar{\theta}\pi}{6} - 1 \right) \right] \left[\sqrt{\frac{1 + C_1^2}{3}} \cos \frac{\bar{\theta}\pi}{6} + C_1 \left(\eta + \frac{1}{3} \sin \frac{\bar{\theta}\pi}{6} \right) \right] \right\}^{-\frac{1}{n}} \quad (3-14)$$

For plane stress condition, Lode angle parameter $\bar{\theta}$ and stress triaxiality η are uniquely linked by

$$\cos\left[\frac{\pi}{2}(1-\bar{\theta})\right] = -\frac{27}{2}\eta\left(\eta^2 - \frac{1}{3}\right) \quad (3-15)$$

The strain and stress ratio are defined as

$$\alpha = \frac{d\varepsilon_2}{d\varepsilon_1} \quad \beta = \frac{\sigma_2}{\sigma_1} \quad (3-16)$$

Assuming Mises-Levy flow rule, the stress and strain ratio are related as

$$\beta = \frac{2\alpha + 1}{2 + \alpha} \quad (3-17)$$

The stress triaxiality is obtained from

$$\eta = \frac{\beta + 1}{3\sqrt{\beta^2 - \beta + 1}} \quad (3-18)$$

From the definition of ϕ , it can be expressed as a function of strain ratio α by

$$\phi = \frac{360^\circ}{\pi} \tan^{-1} \frac{-\alpha}{\sqrt{1 + \alpha^2} + 1} + 90^\circ \quad (3-19)$$

By combining Eq.(3-17)-(3-19), the all-strain-based eMMC fracture locus (Jia & Bai, 2016a, 2016b) based on the generalized plastic flow parameter ϕ is transformed from the original MMC in stress space, i.e.

$$\bar{\varepsilon}_f(\eta, \bar{\theta}) = \tilde{\varepsilon}_f(\phi) \quad (3-20)$$

In order to calibrate the all-strain based eMMC anisotropic fracture model, it is proposed here to use a strain rate potential function to rotate the plastic strain rate tensor to the sheet rolling direction by linear transformation. The all strain based MMC anisotropic fracture model based on linear transformation from strain rate potential function is named as eMMC-Srp hereafter. In this

study, three strain rate potentials are attempted: (1) Srp48 (Hill, 1987), (2) Srp93 (Barlat et al., 1993), and (3) Srp2004-18p (Barlat & Chung, 2005; Kim et al., 2007; Kim et al., 2008).

For the quadratic Hill'48 anisotropic yield function, there exists an analytical strain rate potential conjugated to the anisotropic stress potential function. Eq.(3-21) defines the anisotropic strain rate potential function Srp48. The linear transformation matrix $\boldsymbol{\beta}$ is shown in Eq.(3-22).

$$\dot{\boldsymbol{\varepsilon}}_p = \sqrt{\frac{2}{3}}(\boldsymbol{\beta}\dot{\boldsymbol{\varepsilon}}_p) \cdot (\boldsymbol{\beta}\dot{\boldsymbol{\varepsilon}}_p) \quad (3-21)$$

$$\boldsymbol{\beta} = \begin{bmatrix} \beta_1 & 0 & 0 & 0 \\ 0 & \beta_2 & 0 & 0 \\ 0 & 0 & \beta_3 & 0 \\ 0 & 0 & 0 & \sqrt{2}\beta_4 \end{bmatrix}, \quad \dot{\boldsymbol{\varepsilon}}^p = [\dot{\varepsilon}_{xx}^p \quad \dot{\varepsilon}_{yy}^p \quad \dot{\varepsilon}_{zz}^p \quad \dot{\varepsilon}_{xy}^p]^T \quad (3-22)$$

The linear transformation matrix $\boldsymbol{\beta}$ is positive semi-definite. The anisotropic coefficients β_{ij} can be linked with the parameters F, G, H, N in the Hill'48 anisotropic yield function. For the non-quadratic yield functions Yld91 and Yld2004-18p, it is difficult to find the analytical dual conjugate of the stress potentials. However, it is possible to define the strain rate potentials independently in a similar mathematical form.

The strain rate potential function of Srp93 (Barlat et al., 1993) is defined as:

$$|\xi_1|^\mu + |\xi_2|^\mu + |\xi_3|^\mu = 2\dot{\varepsilon}_e^\mu \quad (3-23)$$

In Eq.(3-23), $\dot{\varepsilon}_e$ denotes the effective strain rate, and $\xi_{i=1,2,3}$ are the principal values of anisotropic plastic strain rates calculated from the linear transformation matrix in Srp93. The exponent $\mu = 3/2$ and $4/3$ are suggested for BCC and FCC material (Barlat et al., 1993). The Srp93 model was developed for a full stress state with 6 parameters. In Srp93, the following matrix transforms the strain rate tensor $\dot{\varepsilon}_{ij}^p$ with anisotropic coefficients $c_{1\sim 6}$.

$$\mathbf{L} = \begin{bmatrix} \frac{c_3(\dot{\epsilon}_{11} - \dot{\epsilon}_{22}) - c_2(\dot{\epsilon}_{33} - \dot{\epsilon}_{11})}{3} & c_6\dot{\epsilon}_{12} & c_5\dot{\epsilon}_{31} \\ c_6\dot{\epsilon}_{12} & \frac{c_1(\dot{\epsilon}_{22} - \dot{\epsilon}_{33}) - c_3(\dot{\epsilon}_{11} - \dot{\epsilon}_{22})}{3} & c_4\dot{\epsilon}_{23} \\ c_5\dot{\epsilon}_{31} & c_4\dot{\epsilon}_{23} & \frac{c_2(\dot{\epsilon}_{33} - \dot{\epsilon}_{11}) - c_1(\dot{\epsilon}_{22} - \dot{\epsilon}_{33})}{3} \end{bmatrix} \quad (3-24)$$

The strain rate potential function of Srp2004-18p (Barlat & Chung, 2005; Kim et al., 2008) is defined as:

$$|\tilde{E}'_1|^b + |\tilde{E}'_2|^b + |\tilde{E}'_3|^b + |\tilde{E}''_2 + \tilde{E}''_3|^b + |\tilde{E}''_3 + \tilde{E}''_1|^b + |\tilde{E}''_1 + \tilde{E}''_2|^b = (2^{2-b} + 2)\dot{\epsilon}^b \quad (3-25)$$

In Eq.(3-25), $\dot{\epsilon}$ denotes the effective strain rate, and $\tilde{E}'_{i=1,2,3}$ and $\tilde{E}''_{i=1,2,3}$ are the principal values of the anisotropic plastic strain rates calculated from the linear transformation matrix in Srp2004-18p. Similar to the Srp93, the exponent $b = 3/2$ and $4/3$ are suggested for BCC and FCC materials (Barlat et al., 1993). The Srp2004-18p model was developed for a full stress state with 18 anisotropic coefficients in general 3D formulation. Under the plane stress conditions for orthogonal incompressible plasticity, the transformed strain rate tensors are defined as

$$\tilde{\boldsymbol{\epsilon}}' = \mathbf{B}'\mathbf{T}\dot{\boldsymbol{\epsilon}}^p, \quad \tilde{\boldsymbol{\epsilon}}'' = \mathbf{B}''\mathbf{T}\dot{\boldsymbol{\epsilon}}^p \quad (3-26)$$

In Eq.(3-26), the linear transformation matrices \mathbf{B}' and \mathbf{B}'' contain 14 anisotropic coefficients in total under plane stress conditions, as represented by

$$\mathbf{B}' = \begin{bmatrix} 0 & -b'_{21} & -b'_{13} & 0 \\ -b'_{21} & 0 & -b'_{23} & 0 \\ -b'_{31} & -b'_{32} & 0 & 0 \\ 0 & 0 & 0 & b'_{66} \end{bmatrix}, \quad \mathbf{B}'' = \begin{bmatrix} 0 & -b''_{21} & -b''_{13} & 0 \\ -b''_{21} & 0 & -b''_{23} & 0 \\ -b''_{31} & -b''_{32} & 0 & 0 \\ 0 & 0 & 0 & b''_{66} \end{bmatrix} \quad (3-27)$$

The matrix \mathbf{T} transforms the four-component strain rate tensor $\dot{\boldsymbol{\epsilon}}^p$ shown as follows

$$\mathbf{T} = \begin{bmatrix} 1 & 0 & 0 \\ 0 & 1 & 0 \\ -1 & -1 & 0 \\ 0 & 0 & 1 \end{bmatrix}, \quad \dot{\boldsymbol{\epsilon}}^p = [\dot{\epsilon}_{xx}^p \quad \dot{\epsilon}_{yy}^p \quad \dot{\epsilon}_{zz}^p \quad \dot{\epsilon}_{xy}^p]^T \quad (3-28)$$

3.2 Experimental Results and Analysis

The tested material is an aluminum alloy 7075-T6 sheet with 2.0 mm thickness provided by Alcoa. The material samples were tested under four loading conditions: (1) uniaxial tension (UT), (2) notch tension (NT), (3) Shear (SH), and (4) uniaxial compression (UC). The tensile tests (1)-(3) were designed for calibration and validating both plasticity and fracture models, and the compression tests were used only for material plasticity calibration. Figure 3-2 shows that all specimens were machined parallel to three material orientations with respect to the rolling direction: 0° (RD), 45° (DD), and 90° (TD). Three specimens were prepared along each orientation for test repeats.

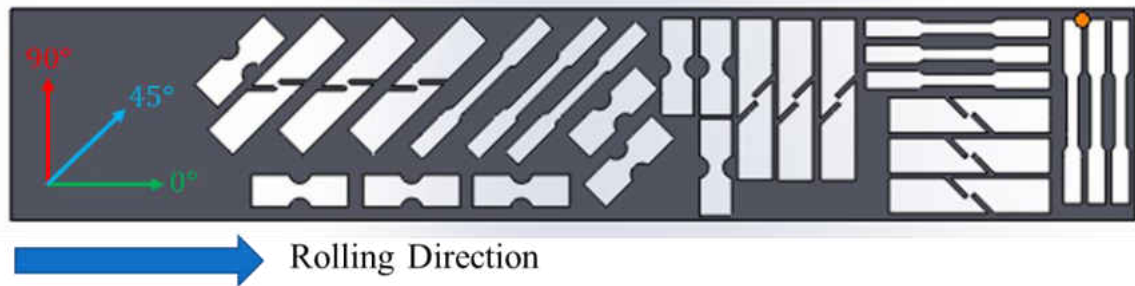


Figure 3-2. Test specimens cut from the 7075 aluminum alloy sheet

All tests were conducted under quasi-static condition on an MTS servo-hydraulic universal testing machine with a 100 kN load cell at room temperature. The displacement and strain fields are in-situ monitored using a digital image correlation (DIC) system throughout the tests. The system is consisting of a Tokina lens with a resolution of 2448×2048 and VIC-2D software by Correlated Solutions, Inc. The test program and the DIC system were triggered simultaneously at the beginning of each test, and the load signals from the testing machine were synchronized with the DIC images at the same sampling rate of 1 Hz.

3.2.1 Uniaxial Tension

The uniaxial tension samples were cut into dogbone shape. The tests were conducted at a nominal strain rate of $10^{-3}/s$. The test results in Figure 3-3(a) suggest that the strength anisotropy in uniaxial tension is not significant. The flow stress curve along 90° is slightly higher than the rolling direction and the flow stress curve along 45° is slightly lower than the rolling direction. The anisotropic plastic flow in uniaxial tension is measured by Lankford ratio (or r-value), defined as the ratio of incremental plastic strains along the width and thickness directions: $r = d\varepsilon_w^p/d\varepsilon_t^p$. It is well-known that the r-value does not maintain a constant during plastic deformation. In the present study, the r-value is determined by the slope of the plastic strains along the width and thickness directions before necking, hence it is regarded as an average value over plastic strain. As shown in Figure 3-3(b), in contrast to the negligible strength anisotropy in uniaxial tension, the present aluminum alloy sheet exhibits strong anisotropic plastic flow in uniaxial tension. The lower r-value along the rolling direction indicates that the material is less resistance to thinning during plastic deformation.

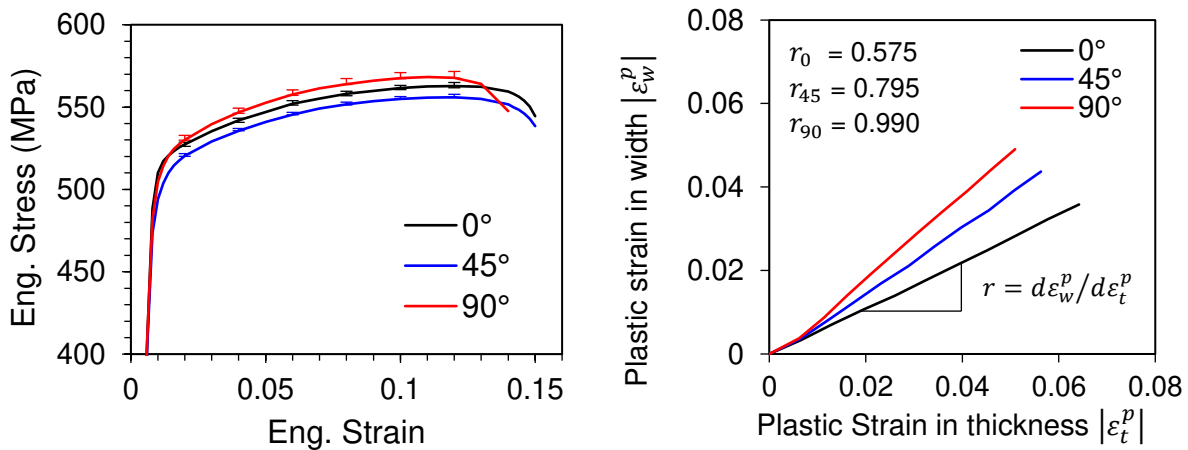


Figure 3-3. Uniaxial tension test results (a) engineering stress-strain (b) Lankford ratio (r-value)

3.2.2 Notch Tension

Notch tension tests were performed on tensile specimens with circular cut-outs along the width direction. The notch tension samples were loaded under displacement control at a constant crosshead speed of 0.02 mm/s. The force-displacement curves of notch tension tests are shown in Figure 3-4. The difference of global force responses can be clearly seen: (1) the force curve along 90° is remarkably higher than the other two directions; (2) the force curve along 45° is also slightly higher than the curve along rolling direction. This indicates that material anisotropy in strength increases when the stress state transits from uniaxial tension to biaxial tension. For notch tension samples, the stress state is biaxial tension in the center and uniaxial tension at the edge. Under plane stress condition, the stress triaxiality at the center point inside the neck is given by the following analytical equation derived in Bai (2007):

$$\eta = \frac{1 + 2\Lambda}{3\sqrt{\Lambda^2 + \Lambda + 1}} \quad (3-29)$$

where $\Lambda = \ln[1 + a/(2R)]$, where a is the half width at the center in the notch, and R is the radius of the notch. The biaxial stress state in the center of the notch sample is related to the width to radius ratio a/R . Readers are referred to Bai (2007) for more detailed derivations of stress distribution inside the neck of a plane strain specimen. In an extreme case for infinitely large radius R , the stress triaxiality $\eta = 1/3$ according to Eq.(3-29), which is exactly the case for uniaxial tension. Eq.(3-29) gives an estimation of stress triaxiality using the initial geometry of the notched samples. During notch tension tests, due to sample geometry change and strain concentration, the deformation is non-uniform and sample thickness distribution is uneven along the width direction. Therefore, it is impossible to obtain an equivalent strain-stress curve which is converted based on

the assumption of uniform deformation. Figure 3-4(b) shows the local strain paths extracted from the center of the specimen in the DIC analysis. The anisotropy in plastic flow of notch tension test can be quantitatively determined by the parameter ϕ . The angle ϕ for notch tension sample is commonly between 90° (uniaxial tension) and 116° (plane strain tension). For the present notch tension sample design, the angle ϕ is 97° along rolling direction (RD), and slightly shifts $\pm 2^\circ$ for diagonal direction (DD) and transverse direction (TD).

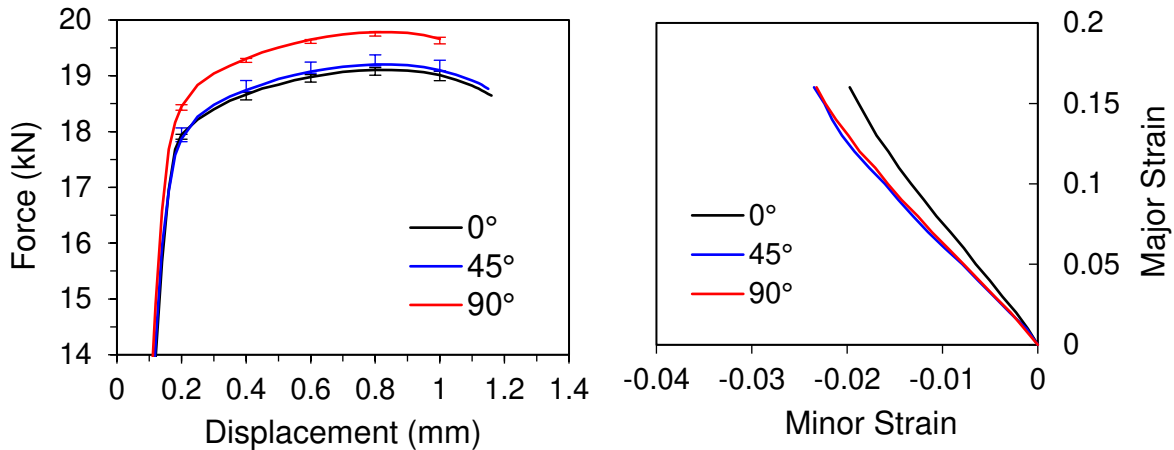


Figure 3-4. Notch tension test results (a) force-displacement curves (b) local strain paths at the notch center

3.2.3 Shear

The simple shear specimen design was originally from Peirs, Verleysen, and Degrieck (2012). The design was later modified as mini-shear specimen in various experimental studies (for example, Abedini, Butcher, and Worswick (2017); (Rahmaan, Abedini, Butcher, Pathak, & Worswick, 2017)) on constitutive modeling and fracture characterization for different metal sheets at University of Waterloo. In this study, the mini-shear sample design was adopted due to its relatively uniform shear strain distribution and simple machining process. The mini-shear samples were loaded vertically with pin-hole gripping at a constant cross-head speed of 0.01 mm/s. The

shear test results in Figure 3-5 suggest that both strength and plastic flow in shear are nearly isotropic. Also, no necking was observed from the abrupt drop in the force-displacement curves, indicating the shear dominated deformation.

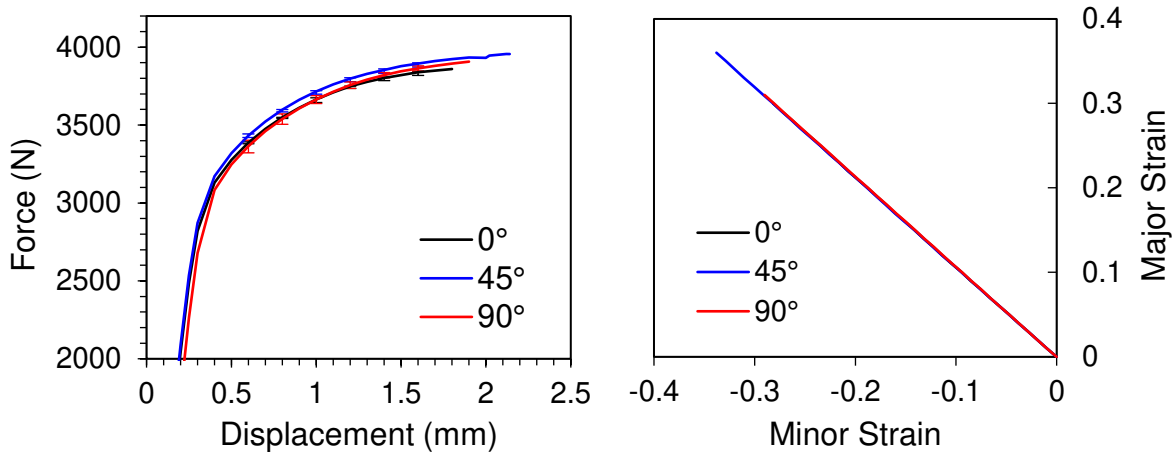


Figure 3-5 Shear test results (a) force-displacement curves (b) local strain paths from the shear zone center

Since the mini-shear sample design allows a relatively uniform shear strain distribution, the engineering shear stress-strain curve can be estimated by converting the force-displacement data. The shear stress τ is calculated as

$$\tau = \frac{F}{th} \quad (3-30)$$

where t is the specimen thickness, and h is the height of the shear zone. The engineering shear strain γ was evaluated from DIC analysis in the shear zone. Even though the conversion is not completely rigorous due to the involvement of uniaxial loading at the edge and slight shear zone rotation, it ensures a satisfactory level of accuracy for material model calibration. The engineering shear stress-strain curve can be further converted to the von-Mises equivalent stress and strain by Eq. (3-31) and (3-32).

$$\bar{\sigma} = \sqrt{3}\tau \quad (3-31)$$

$$\bar{\varepsilon} = \frac{2}{\sqrt{3}}\varepsilon_{12} = \frac{1}{\sqrt{3}}\gamma_{12} \quad (3-32)$$

3.2.4 Compression Tests

A set of small cuboid specimens were designed for uniaxial compression tests. The cuboid specimens were cut into 4 mm in length and 3 mm in width, with original sheet thickness of 2 mm. The length-to-width ratio is designed in such a way to guarantee the uniaxial compression stress state with no buckling (Jia & Bai, 2016b). The samples were loaded along the length direction. The top and bottom surfaces of the samples were lubricated by Teflon tapes to reduce friction in contact with compression platens. During the tests, the 0° and 90° cuboid samples were loaded until fracture with a noticeable load drop, but the 45° samples can sustain more load without fracture until the machine limit. However, due to the surface friction effect, the deformation under uniaxial compression is not uniform at large strain, therefore only the uniform deformation part data is presented in this paper. The engineering stress-strain curves for uniaxial compression is shown in Figure 3-6. The strength anisotropy is in the same trend as uniaxial tension, but the hardening curve along 45° in uniaxial compression is much lower than the curves along the other two material directions.

The through-thickness compression (or disk compression) tests were also conducted as supplementation for plasticity model calibration. The balanced-biaxial (or equi-biaxial) tension stress state can be obtained from the disk compression test, as an alternative to the hydraulic bulge test or the cruciform specimen test. The 10 mm diameter disk samples were loaded under

compression along the thickness direction. The sample surfaces were lubricated by Teflon tapes in contact with the compression platens. Since the sample is so small and placed in between the large compression platens, it is difficult to monitor sample deformation by DIC camera. Therefore, the local displacement on the sample was extracted from the spray painted papers attached to the rigid compression platens. Also, the disk sample was only loaded up to a small amount of displacement in each test, so that the force-displacement data can be converted to into stress-strain data under uniform deformation condition as follows according to Steglich, Tian, Bohlen, and Kuwabara (2014):

$$\sigma_b = \frac{4F}{\pi d_0^2} \left(1 - \frac{u}{t_0}\right), \quad \varepsilon_t = \ln \left(1 - \frac{u}{t_0}\right) \quad (3-33)$$

Where σ_b denotes the uniaxial compressive stress, ε_t denotes the uniaxial strain along the thickness direction, u is the vertical displacement from the rigid compression platens, F is the force measured from the load cell, t_0 is the thickness of the disk sample, and d_0 is the original diameter of the disk sample. The uniaxial stress-strain for through-thickness compression coincide with the von Mises equivalent stress-strain, i.e.

$$\bar{\sigma} = \sigma_b, \quad \bar{\varepsilon} = \varepsilon_t \quad (3-34)$$

Note that Eq.(3-33) and (3-34) only apply to the uniform deformation condition. From the present tests, it is difficult to justify if the deformation still remains uniform at large strain due to the friction effect, so for this reason, only the stress-strain data at initial yield and small plastic strain (up to 2%) is presented here as shown in Figure 3-6. The initial yield can be clearly identified from the slope transition on the curve.

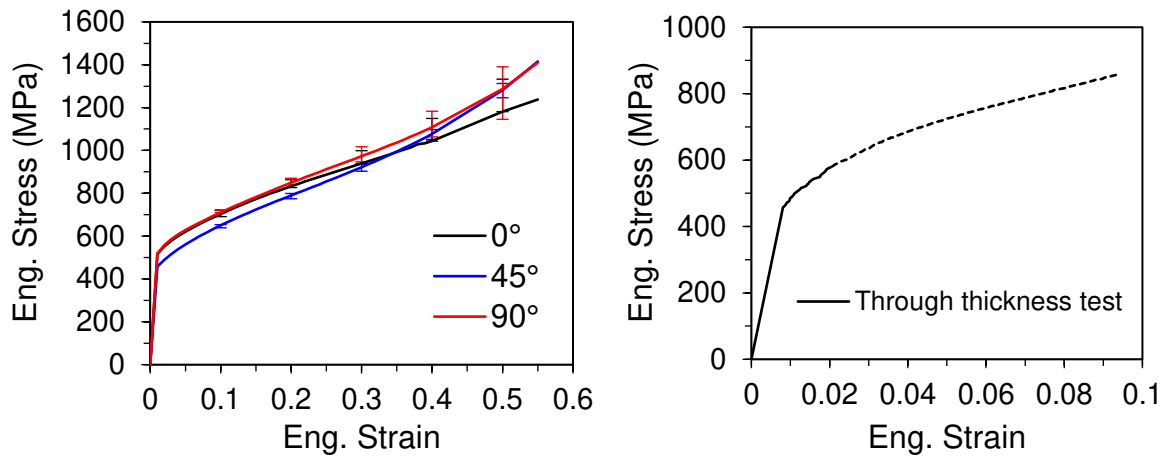


Figure 3-6. Experimental results of (a) uniaxial compression test (b) through-thickness compression test

3.2.5 Strain Analysis in DIC

Figure 3-7 summarizes the strain histories from DIC analysis for all tensile type tests. The strain histories were extracted from the location of the greatest equivalent plastic strain: (1) UT: at the localized neck (2) NT: at the center of the notch (3) SH: in the localized shear zone. The test results demonstrate remarkable repeatability so only one curve is plotted for each test. The values of angle ϕ is nearly constant except for the initial part, indicating that the deformation was under proportional loading condition. As mentioned above, the anisotropic plastic flow is only noticeable for uniaxial tension. The strain paths for notch tension and shear tests suggest negligible dependence on material directions. For compression tests, since the images can be only captured from the side view and no interrupted tests were repeated, the strain information is not available for DIC analysis.

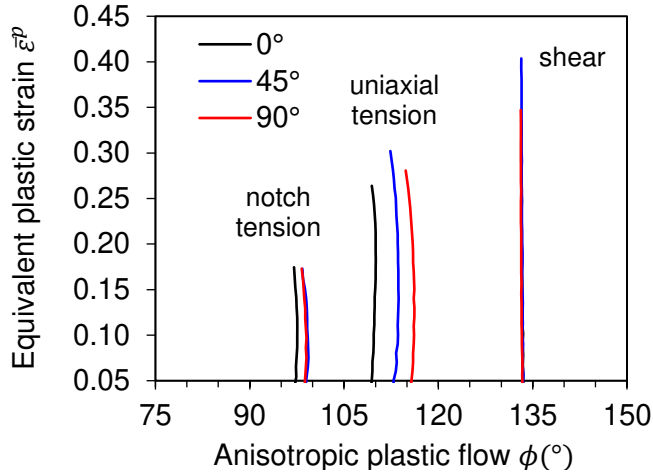


Figure 3-7. Strain paths to fracture in the space of $\bar{\epsilon}^p - \phi$ from uniaxial tension, notch tension and shear tests

The DIC technique is widely used in fracture strain analysis for industrial applications nowadays. In most existing ductile fracture models, the equivalent strain to fracture is defined as a function of stress parameters such as stress triaxiality, which cannot be obtained directly from experiments. The advantage of the all-strain based model is that the fracture locus can be directly calibrated from the DIC software without the complication from inverse analysis in FE simulations. This is especially efficient for fracture model calibration when the anisotropic effect is incorporated. In VIC-2D, the software supports an interface for implementing a user-defined variable by post-processing in the VicPy module. Figure 3-8 shows the contour plots of the user-defined variables: (1) the plastic flow parameter ϕ and (2) the anisotropic equivalent plastic strain $\bar{\epsilon}_f$ before fracture in uniaxial tension tests. One can see that the anisotropic effect is well distinguished by the angle offset from $\phi = 116^\circ$ as the isotropic base for uniaxial tension.

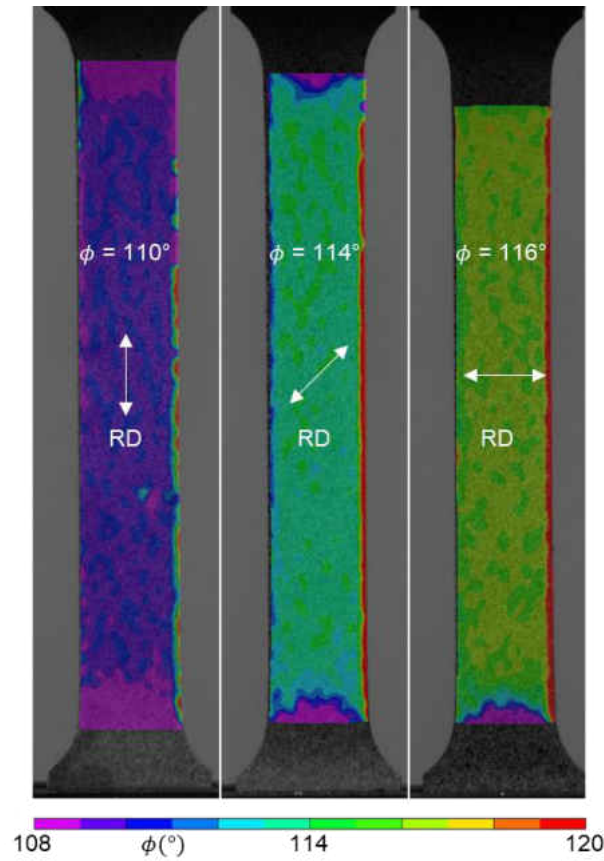


Figure 3-8. Contour plots of the plastic flow parameter ϕ in the DIC software VIC-2D

3.3 Calibration of Anisotropic Material Models

3.3.1 Equivalent Stress-strain Curve based on J2 Plasticity

The test data from the previous section were converted into equivalent plastic stress-strain curves based on J2 plasticity. Note that the conversion only applies to the test data from uniform deformation in UT, SH and UC. Figure 3-9 (a) and (b) compare the hardening curves of SH and UC with the hardening curves of UT, respectively. Figure 3-10 summarizes the hardening curves of different loading conditions the along rolling direction. First, it can be seen that the hardening curves along UT and SH show similar trends from initial yield to the necking strain in uniaxial

tension, but the equivalent stress of SH is lower than UT under the assumption of J2 plasticity. This indicates that the yield locus along shear should be adjusted from the von Mises ellipse. Further FE simulation results suggest that shear hardening becomes more compliant beyond necking strain in uniaxial tension. Second, from the comparison of hardening curves for UT and UC, the tension-compression asymmetric effect can be observed but not significant for 0° and 90°. The hardening curve along 45° in UC is much lower, implying that the shear stress component plays an important role in material anisotropy. Finally, the flow stress curves along rolling direction under different loading conditions are shown in Figure 3-10. σ_b is slightly larger than unity from the only available data for initial yield and not shown here. Similar result is also reported from a recent study on Al7075 in Abedini, Butcher, Rahman, and Worswick (2018).

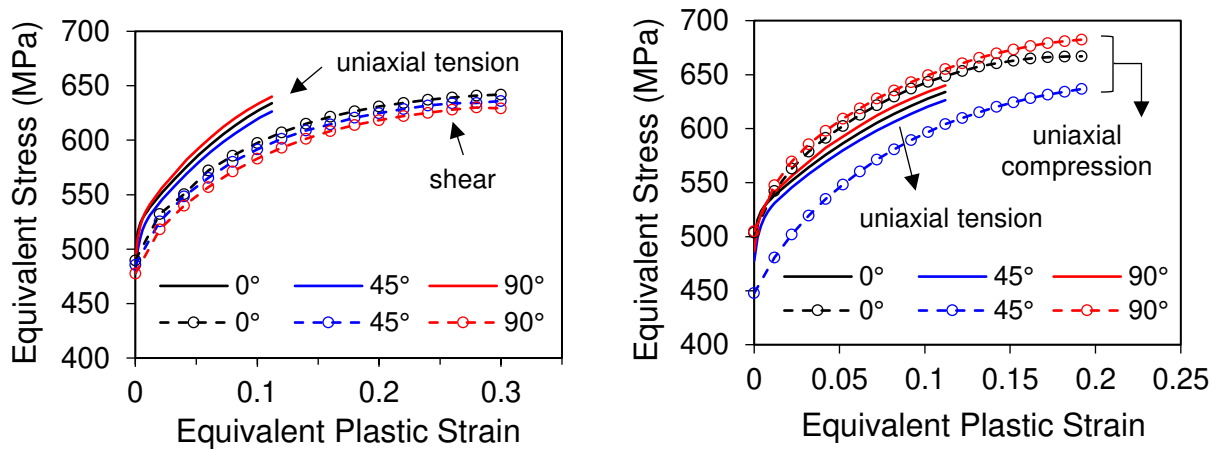


Figure 3-9. von Mises equivalent stress-equivalent plastic strain curves (a) uniaxial tension and shear (c) uniaxial tension and uniaxial compression

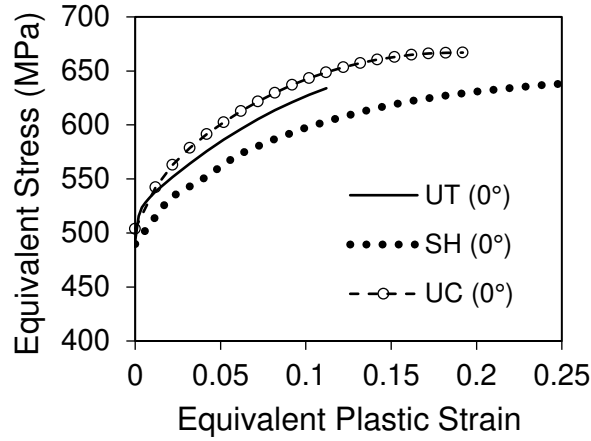


Figure 3-10. von Mises equivalent stress-plastic strain curves for all loading conditions along rolling direction

3.3.2 Calibration of Anisotropic Plasticity Model with Lode Angle Correction

The Yld2000-2d is calibrated from uniaxial tension and disk compression test results. Table 3-1 lists the normalized yield stresses and Lankford ratios from the uniaxial tension tests, and the balanced biaxial stress σ_b from the disk compression test. The optimization program was set up for solving a non-linear least square problem by minimizing the error function (Barlat et al., 2005) as follows

$$E = \sum_p w_p \left(\frac{\sigma_p^{pr}}{\sigma_p^{exp}} - 1 \right)^2 + \sum_q w_q \left(\frac{r_q^{pr}}{r_q^{exp}} - 1 \right)^2 \quad (3-35)$$

In Eq.(3-35), p and q represent the number of flow stresses or r-values available from experiments, and w_p and w_q are the weighting factors. The error function sums the difference squares of the model prediction over the experimental data. In this work, since the solution is unique based on uniaxial tension and equi-biaxial tension results, the flow stresses and r-values are equally weighted. The Yld2000-2d parameters are listed in Table 3-1 and the initial anisotropic yield locus is plotted in Figure 3-11.

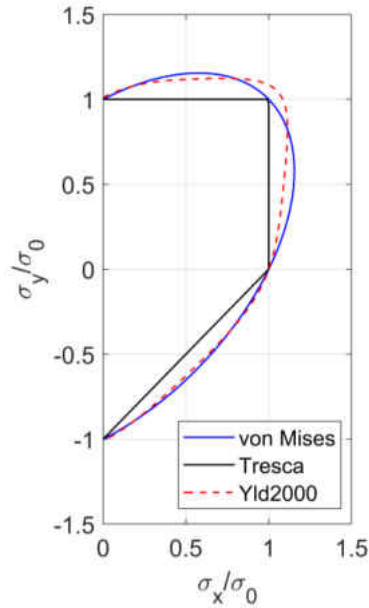


Figure 3-11. Yld2000-2d initial yield locus of Al7075 aluminum alloy sheet

Table 3-1. Yld2000-2d anisotropic yield function parameters for Al7075-T6

Exp. data	σ_0	σ_{45}	σ_{90}	σ_b	r_0	r_{45}	r_{90}	r_b	
	1.00	0.99	1.01	1.05	0.575	0.795	0.990	1.0	
Yld2000-2d	a_1	a_2	a_3	a_4	a_5	a_6	a_7	a_8	m
	0.9071	1.1027	0.8179	0.9956	1.0425	0.8496	1.0274	1.2548	8

The isotropic hardening curve is calibrated from uniaxial tension along the rolling direction using a linear combination of Swift-Voce hardening law in Eq.(3-11). As shown in Figure 3-12, both Swift and Voce hardening laws fit the uniaxial tension test data well before necking. After necking, the hardening curve was extrapolated by the combined Swift-Voce hardening function with a weighing factor α in Eq.(3-11). The weighting factor α was determined by iterations of FE simulations for uniaxial tension. This methodology ensures a smooth piecewise increasing post-hardening curve, which is efficient for model calibration and numerical simulations.

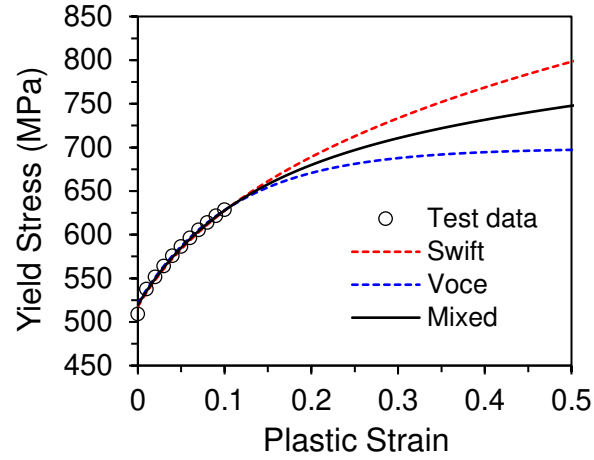


Figure 3-12. Swift-Voce hardening curve law for extrapolation after necking

The assumption of isotropic hardening may not be adequate for accurate description of plastic deformation even under proportional loading condition. The present test data and FE simulation results both suggest that it is necessary to correct the isotropic hardening curve with Lode dependence for $0 \leq \bar{\theta} \leq 1$, where $\bar{\theta}$ denotes the Lode angle parameter as defined by Eq.(3-5). $\bar{\theta} = 0$ refers to the loading conditions of shear and plane strain tension (or generalized shear), while $\bar{\theta} = 1$ refers to the positive axial symmetry loading condition (i.e. uniaxial tension) (Bai & Wierzbicki, 2008). The Lode dependence on flow stress can be adjusted by defining the Lode angle dependent term c_{θ}^s as an evolutionary function of equivalent plastic strain $\bar{\epsilon}_p$ in the following

$$c_{\theta}^s(\bar{\epsilon}_p) = c_L + \frac{c_L - c_U}{1 + e^{s_c(\bar{\epsilon}_p - \epsilon_c)}} \quad (3-36)$$

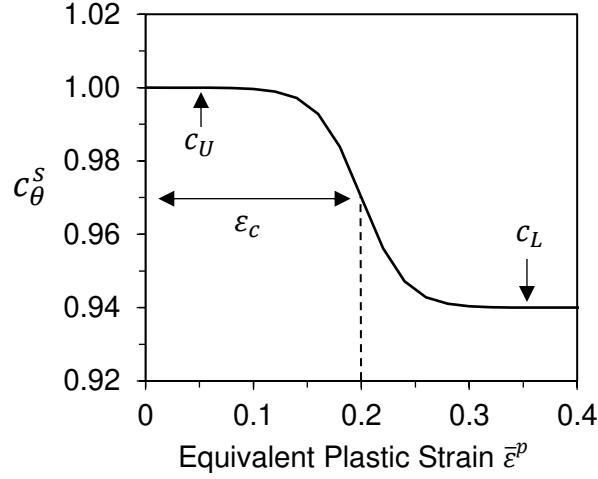


Figure 3-13. Lode dependence parameter c_{θ}^s as evolution of equivalent plastic strain $\bar{\epsilon}_p$

In Eq. (3-36), c_L and c_U defines the lower and upper bounds of c_{θ}^s ; s_c and ϵ_c are chosen to control the transition rate and position through the exponential term. Eq. (3-36) is depicted as shown in Figure 3-13. It demonstrates an S-shape curve from initial yield to fracture with a rapid transition in the middle. In addition to the hardening correction by Lode dependence for $0 \leq \bar{\theta} \leq 1$, the tension-compression asymmetry is also modified through the Lode angle asymmetric parameter c_{θ}^{ax}

$$c_{\theta}^{ax} = \begin{cases} c_{\theta}^t & \bar{\theta} \geq 0 \\ c_{\theta}^c & \bar{\theta} < 0 \end{cases} \quad (3-37)$$

In Eq. (3-37), c_{θ}^t is set to unity and $c_{\theta}^c = 1.02$ was determined from experimental results of uniaxial compression ($\bar{\theta} = -1$). The Yld2000-2d is assumed that, in the deviatoric stress plane, the yield surface is symmetric for uniaxial tension and uniaxial compression. This restriction can be removed in the present model by setting $c_{\theta}^c \neq c_{\theta}^t$. Figure 3-14 presents the hardening curves dependent on loading condition effect by Eq.(3-10). The yield locus evolution is correspondingly illustrated by 2D plot in Figure 3-15. With the Lode dependent parameters c_{θ}^s and c_{θ}^{ax} , the new

yield locus changes based on the Yld2000-2d yield locus according to Eq.(3-36) with evolution of plastic strain. The yield locus asymmetric behavior by Eq.(3-37) can be also observed in the plot.

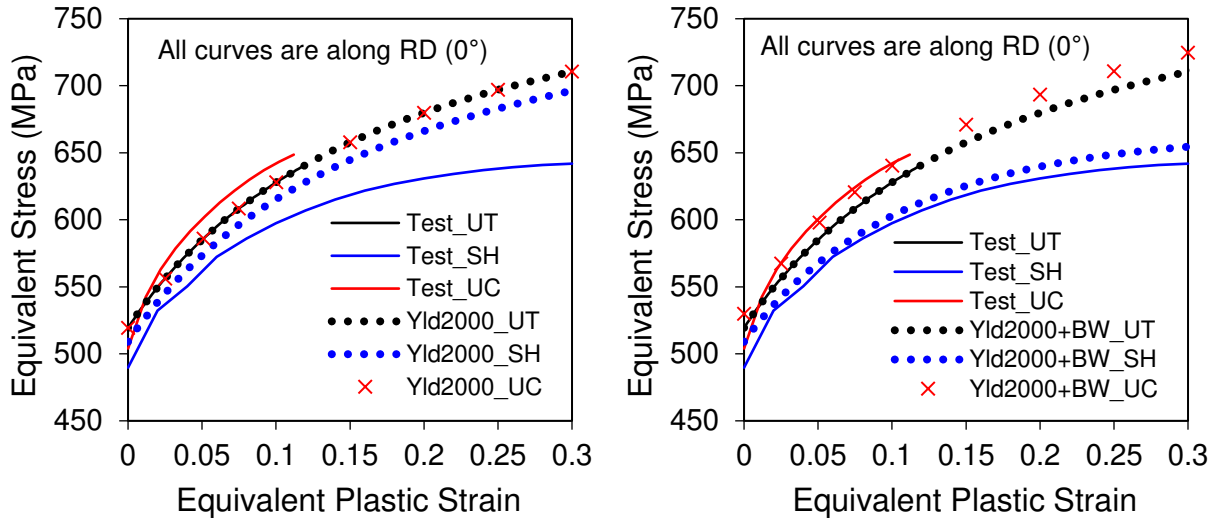


Figure 3-14. Evolution of hardening curve Yld2000-2d model with and without BW plasticity model correction

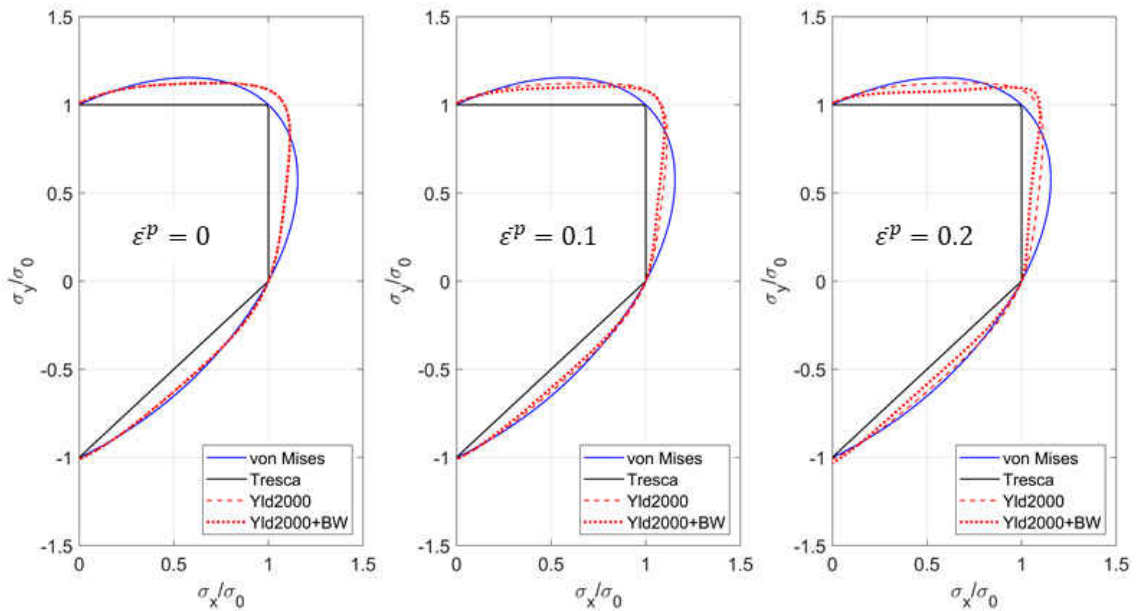


Figure 3-15. Evolution of Yld2000-2d yield locus with BW plasticity model correction

In a recent study on anisotropic plasticity of AA6013 sheet (Ha et al., 2018), the evolution of yield surface is corrected by a viable exponent of the Yld2004-18p anisotropic yield function. This method is conceptually similar to the present method but fundamentally different. The viable exponent in Ha et al. (2018) was calculated from an “equivalent stress-strain” curve obtained from notch tension tests on wide specimens. This is plausible because the stress-state is non-uniform on a flat notch sample unless thickness reduction is introduced, such as the flat groove specimen (Bai & Wierzbicki, 2008). The investigation of anisotropic plasticity in Ha et al. (2018) is still focused on initial anisotropy, with little consideration for hardening correction under plane strain tension condition ($\bar{\theta} = 0$). The present model framework not only considers initial anisotropy, but also accounts for generalized hardening for all loading conditions ($-1 \leq \bar{\theta} \leq 1$). It is also worth remarking here that, readers should not be confused about the Swift-Voce hardening law with the hardening correction by stress triaxiality and Lode angle. The Swift-Voce hardening law aims to extrapolate the isotropic hardening curve beyond material necking calibrated from uniaxial tension; while the latter corrects material hardening for other loading conditions using the base curve described by the Swift-Voce hardening law.

3.3.3 Calibration of Anisotropic Fracture Model

The all-strain based anisotropic fracture model eMMC-Srp was calibrated using different strain rate potential functions introduced in Section 3.1.4. The fracture locus $\tilde{\epsilon}_f(\phi)$ was first calibrated from the averaged fracture data points of each loading condition. Then the anisotropic fracture parameters were calibrated by minimizing the error function of Eq.(3-38)

$$E = \sum_{\phi} \left(\frac{\hat{\epsilon}_f^{pr}}{\tilde{\epsilon}_f^{\phi}} - 1 \right)^2 \quad (3-38)$$

Where $\tilde{\epsilon}_f^{\phi}$ refers to the fracture strain at each given ϕ value on the fracture locus $\tilde{\epsilon}_f(\phi)$, and $\hat{\epsilon}_f^{pr}$ denotes the predicted fracture strain transformed by the strain rate potential function at the corresponding ϕ value. Since the coupon tests were under proportional loading conditions, the ϕ value can be taken as the average through the linear strain path for each test. Note that $\hat{\epsilon}_f^{pr}$ is summed over the history of plastic deformation

$$\hat{\epsilon}_f^{pr} = \int \dot{\hat{\epsilon}}_p^{pr} dt \quad (3-39)$$

In Eq.(3-39), $\dot{\hat{\epsilon}}_p^{pr}$ is the effective plastic strain rate defined by the strain rate potential function (i.e. $\dot{\hat{\epsilon}}$ in Eq.(3-23) and (3-25)). The error function takes into account the strain history effect for calculating anisotropic equivalent plastic strain. For simplicity, the strain history effect can be removed under linear strain path. The material parameters of anisotropic fracture models are listed in Table 3-2.

Table 3-2. Anisotropic fracture model parameters for Al7075-T6

	c_1	c_2	c_{θ}^s	c_{θ}^c	A	n	
Isotropic MMC model	0.1105	409.6	0.9708	1.0008	846.4	0.152	
eMMC-Srp48	β_1	β_2	β_3	β_4			
anisotropic parameters	1.070	0.549	1.283	0.967			
eMMC-Srp93	c_{12}	c_{13}	c_{21}	c_{23}	c_{31}	c_{32}	c_{66}
anisotropic parameters	0.3123	1.6931	1.4258	0.7270	0.4455	0.3659	1.1301
eMMC-Srp2004	b'_{12}	b'_{13}	b'_{21}	b'_{23}	b'_{31}	b'_{32}	b'_{66}
anisotropic parameters	0.3590	1.8722	0.8696	0.4902	0.5552	0.4553	1.4368
	b''_{12}	b''_{13}	b''_{21}	b''_{23}	b''_{31}	b''_{32}	b''_{66}
	0.9707	1.1066	0.9678	-0.1213	0.2474	0.9736	0.5814

Figure 3-16 demonstrates the calibration results of anisotropic fracture model eMMC-Srp. Figure 3-16 shows the anisotropic fracture locus and the fracture strain data calculated from the strain rate potentials of Srp48, Srp93 and Srp2004, respectively. In each plot, the solid line represents the same fracture locus $\tilde{\epsilon}_f(\phi)$. The circular markers represent the equivalent plastic strain at fracture by assuming all anisotropic fracture parameters equal to one (i.e. isotropic), while the cross markers represent the anisotropic equivalent plastic strain calculated from the linear transformation matrix. The calibration results suggest that for the present data, the Srp48 model with 4 parameters predicts the same level of accuracy as the most complex Srp2004 model using 14 parameters. All models predict the noticeable anisotropic fracture behavior very well in uniaxial tension. If anisotropy plastic flow is strong for all loading conditions, the Srp2004 is expected to predict better correlation results.

In finite element simulations, a linear damage accumulation rule was applied

$$D = \int \frac{d\tilde{\epsilon}_p}{\tilde{\epsilon}_f(\phi)} \quad (3-40)$$

Where $\tilde{\epsilon}_f(\phi)$ is the all-strain based anisotropic fracture locus and $\tilde{\epsilon}_p$ is the anisotropic equivalent plastic strain.

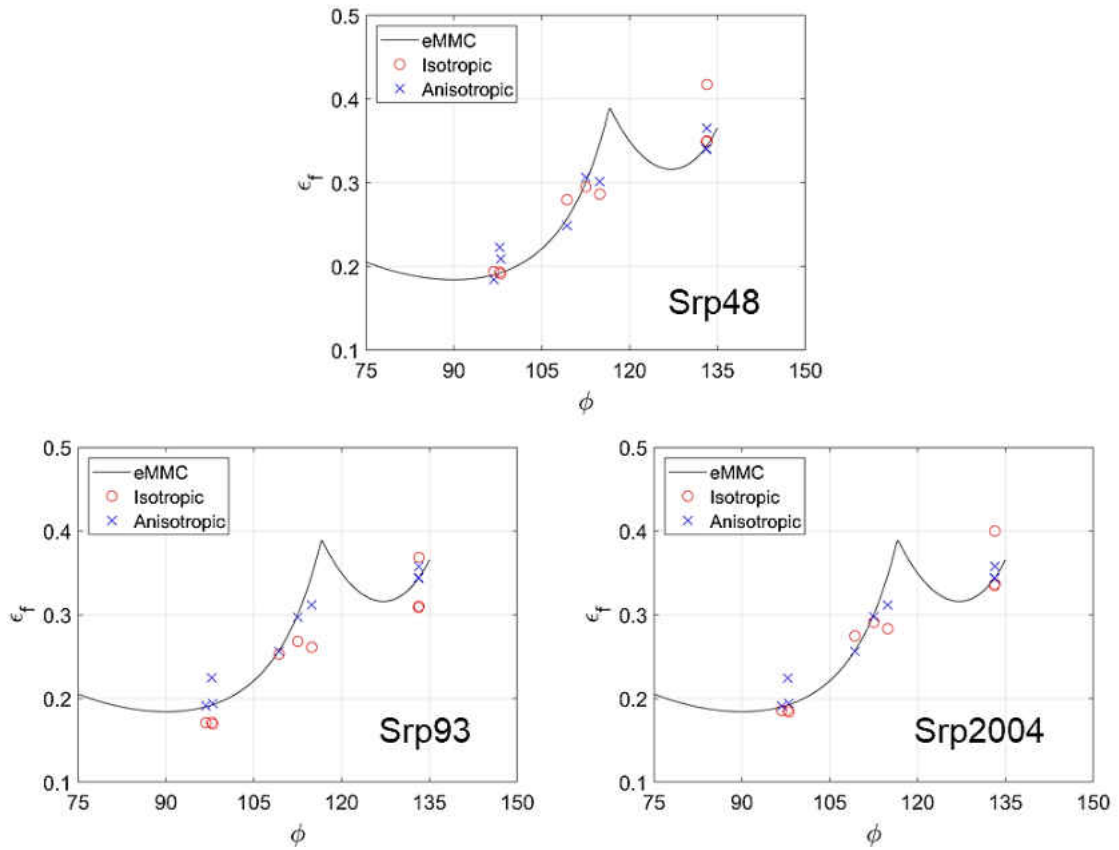


Figure 3-16. Anisotropic fracture model eMMC-Srp: Srp48, Srp93 and Srp2004. The solid line represents the eMMC fracture locus. The red markers denote the fitting results using isotropic coefficients in a strain rate potential function. The blue markers denote the fitting results using optimized anisotropic coefficients in a strain rate potential function.

3.4 Finite Element Analysis

The anisotropic plasticity and fracture models have been implemented by a user-defined material subroutine VUMAT in Abaqus/explicit (v2017). The finite element (FE) simulations were carried out using shell elements S4R (four-node shell elements with reduced integration points), with five Simpson integration points assigned through the shell thickness. The fracture initiation and crack propagation were simulated by deleting elements when the damage accumulation variable D reached a given critical value $D_c = 1$. The Srp48 anisotropic fracture model was used for simple demonstration of anisotropic fracture effect.

3.4.1 Uniaxial Tension

The FE simulation results of uniaxial tension tests are shown in Figure 3-17. The test results are denoted by solid lines and the simulation results are shown in dotted lines. The global displacement and local strain history outputs from the FE simulations were extracted at the same location as in the DIC analysis. The simulation results predicted almost identical results for both anisotropic yield stress and plastic flow as in the experiments. This can be essentially confirmed from the analytical calibration of the anisotropic yield function Yld2000-2d based on the experimental data before necking in uniaxial tension. After necking, the weighting factor in the combined Swift-Voce hardening law was adjusted iteratively to fit the post-necking part of the experimental data. Figure 3-18 shows the contour plot results of the anisotropic plastic flow parameter ϕ and the anisotropic equivalent plastic strain $\tilde{\epsilon}_f(\phi)$ from FE simulations. The FE simulation results are also in a good agreement with the DIC analysis results, so that the anisotropic fracture induced by anisotropic plastic flow is clearly demonstrated.

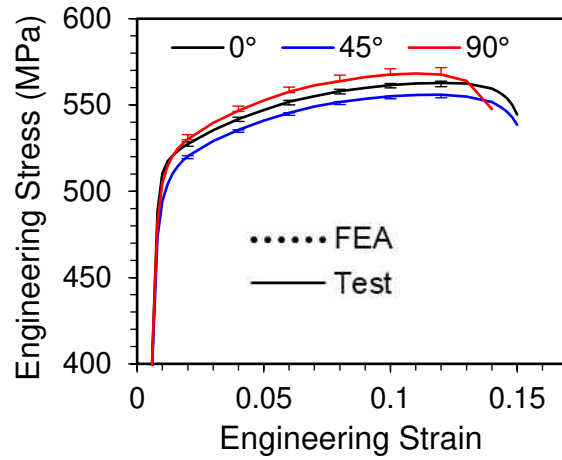


Figure 3-17. FE simulations of uniaxial tension: engineering stress-strain curve

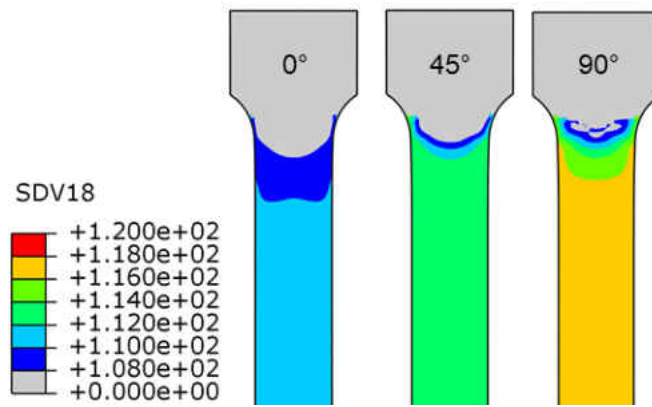


Figure 3-18. FE simulation results of uniaxial tension: anisotropic plastic flow measure angle ϕ (SDV18)

3.4.2 Notch Tension

Figure 3-19 shows the FE simulation results of notch tension tests using (a) only Yld2000-2d and (b) Yld2000-2d by flow stress correction in Eq.(3-10). In Figure 3-19(a), if only the anisotropic yield function Yld2000-2d is used, the force-displacement predictions from FE simulations agree well with the experimental results in the initial yield part. However, the discrepancy between FE simulations and experimental results became larger as the displacement increases. This indicates the limitation of Yld2000-2d and demonstrates the necessity to

incorporate the flow stress correction with plastic strain evolution. The present Yld2000-2d anisotropic yield model was calibrated from uniaxial tension and equi-biaxial tension stress states, as suggested in the original paper of Barlat et al. (2003). Hence, the calibrated model may lead to some discrepancies in predicting other stress states, such as plane strain tension and shear. More importantly, the Yld2000-2d is only calibrated for initial yield stress without considering anisotropic hardening at different loading conditions. For the present notch tension sample, the stress state at the notch center was initially in a general biaxial tension ($\bar{\theta} = 0.5$), and then switched to plane strain tension stress state ($\bar{\theta} = 0$) after strain localization. Meanwhile, the free edge was always in uniaxial tension stress state ($\bar{\theta} = 1$). At a given displacement, the global force is an integration of vertical force from the cross-section over the width direction:

$$F = 2 \int_0^a \sigma_{yy}(\bar{\theta}) t dx \quad (3-41)$$

As seen in Eq.(3-41), the total force F is a function of Lode angle parameter $\bar{\theta}$, or equivalently a function of stress triaxiality η under plane stress condition according to Eq.(3-15). It may not be straightforward to derive an analytical function of force-displacement for the notch tension test due to non-uniform deformation, but in order to lower the force prediction at large displacement, it is necessary to reduce the flow stress towards $\bar{\theta} = 0$ by $h(\eta, \theta)$ in Eq.(3-10). For the present material, only the Lode angle term in $h(\eta, \theta)$ was suggested for flow stress correction. The main reason is that the force over-prediction using Yld2000-2d does not only occur in notch tension test, but also in shear tests to be shown in the next section. In both cases, the Lode angle parameter $\bar{\theta} = 0$ at stress states of plane strain tension and shear. In FE simulations, by assigning the parameter C_{θ}^S as a function of plastic strain, the flow stress can be lowered for $\bar{\theta} = 0$. The

parameter C_{θ}^S was defined as a smooth S-curve bounded between 1.0 and 0.9. By changing the coefficients of the S-curve iteratively, the force-displacement curves agree well with the experimental results (the error become less than 0.8%), as shown in Figure 3-19(b). The plastic strain distributions at the fracture initiation are presented in Figure 3-20.

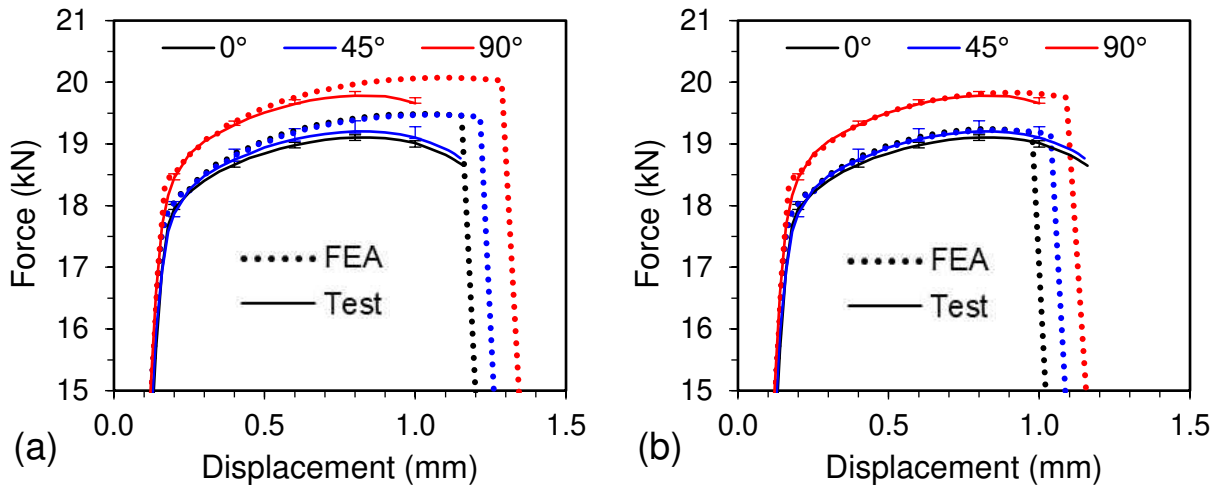


Figure 3-19. FE simulations of notch tension (a) using Yld2000 only (b) using Yld2000 and BW plasticity correction

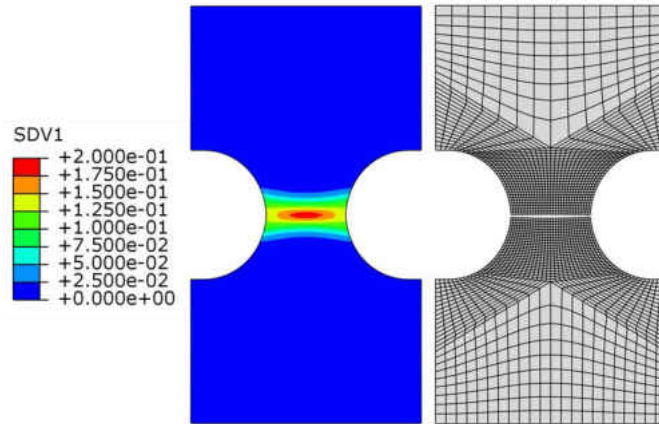


Figure 3-20. FE simulation results from notch tension tests along rolling direction (SDV1: equivalent plastic strain)

It is worth mentioning that an alternative method (e.g. in Abedini et al. (2018)) for Yld2000-2d calibration is to minimize the error function in Eq.(3-35) by assigning different weighting factors on any particular terms. For example, if large weighting factors are assigned for

shear stress and plastic flow, then the calibration result is more accurate for shear but comprised for other loading conditions. Therefore, the calibration result of an anisotropic yield function strongly depends on the user's choice if more unknowns are introduced than the number of coefficients (8 parameters in case of Yld2000-2d). In this work, the Yld2000-2d yield function was calibrated for initial anisotropy with a unique solution based on uniaxial tension and equibiaxial tension. The hardening model further corrects the deformation-induced anisotropy under proportional loading conditions. Similar methodology was used in previous work on Mg alloy sheets in Jia and Bai (2016a) with strong anisotropic, tension-compression asymmetry and complex hardening behavior.

3.4.3 Shear

The FE simulation results of force-displacement for shear tests are shown in Figure 3-21. In the FE model, a fine mesh size of 0.2 mm was used to discrete the localized shear zone of the shear specimen. The mesh size was determined from a mesh convergence study as shown in the discussion. Like the notch tension simulations, if only using Yld2000-2d, the FE simulations of the shear tests also over-predict the force response for about maximum 3% for all three material orientations. Since the Lode angle parameter is zero ($\bar{\theta} = 0$) for shear stress state, the force can be corrected using the same adjusted parameter $C_{\bar{\theta}}^s$ as in notch tension simulations. Figure 3-21 shows the FE simulation results after the flow stress correction by Eq.(3-10). In the present study, the choice of adjusting the Lode angle dependent coefficient $C_{\bar{\theta}}^s$ is sufficient for optimum simulation results in correlation with the experimental data. In general, the accuracy of the hardening model

can be further improved by the pressure correction term dependent on stress triaxiality η in $h(\eta, \theta)$ if more test data are available.

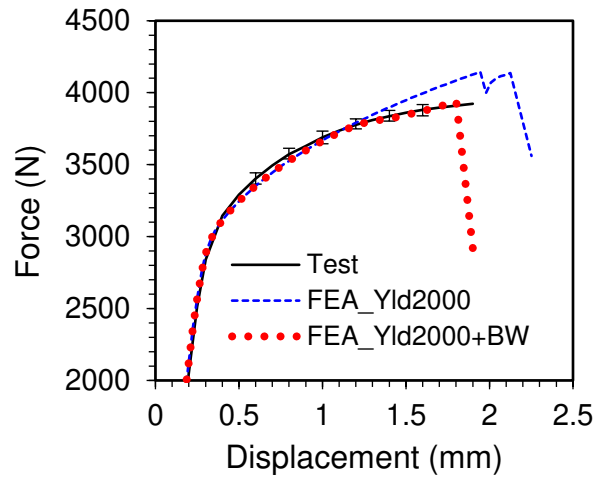


Figure 3-21. FE simulation results of shear test along RD using Yld2000 and BW plasticity model correction.

Figure 3-22 shows that the FE simulation results correctly predicted strain localization and fracture initiation within the shear zone as seen in the experiments. In this sample design, two potential fracture modes are competing: (1) crack in the shear zone and (2) crack at the notch edge. The loading condition is simple shear in the center; while at the notch edges, the stress state is either uniaxial tension or compression due to the free boundary condition. The fracture initiation location is determined by the rate of damage accumulation under the given fracture locus. Figure 3-22 demonstrates that by using the present anisotropic plasticity and fracture model, the damage accumulation at the center shear zone was faster than that at the notch edge, therefore the shear crack initiated first in the FE simulations.

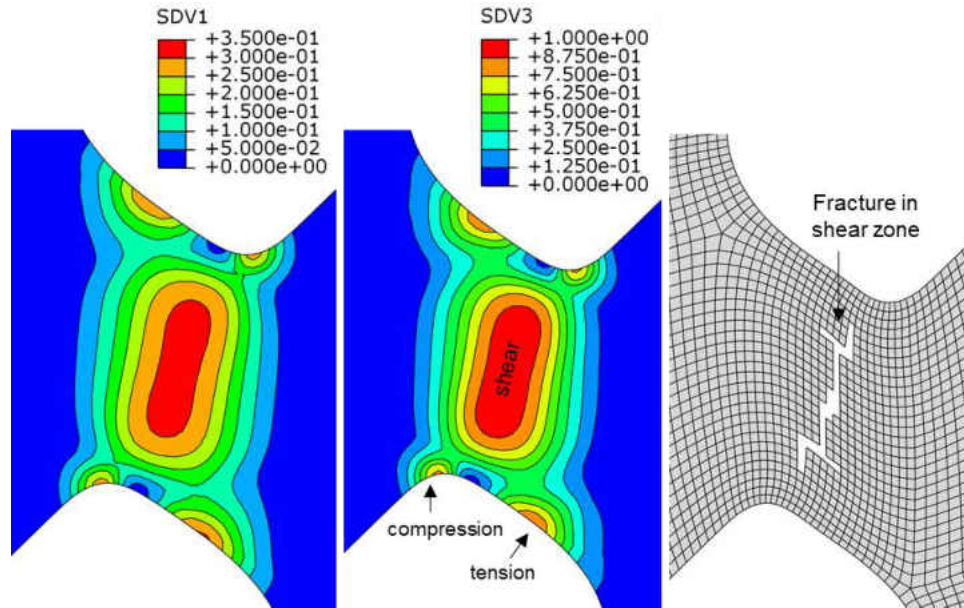


Figure 3-22. FE simulation results of shear test (a) contour plot of equivalent plastic strain (SDV1) (b) contour plot of damage parameter D (SDV3) (c) Fracture initiation in the shear zone

3.4.4 Strain Paths to Fracture

The strain paths to fracture are summarized in the all-strain based space ($\tilde{\epsilon}_p - \phi$) as shown in Figure 3-23. As introduced in previous sections, $\tilde{\epsilon}_p$ denotes the anisotropic fracture strain after linear transformation, and ϕ is the anisotropic plastic flow parameter. In Figure 3-23, the solid lines represent the test data and the circular markers represent the strain histories from FE simulations. For each FE simulation, the strain path was extracted from the critical element at fracture initiation. The strain paths are from tensile loading tests (UT, NT and SH) only. The strain histories from uniaxial compression simulations were omitted due to the limitation of shell elements. The 3D solid element will be more suitable to consider the strain histories of compression simulations. The FE simulation results demonstrate that with the current proposed

anisotropic plasticity and fracture models, the local strain paths to fracture are well correlated with the experimental results under proportional loading conditions.

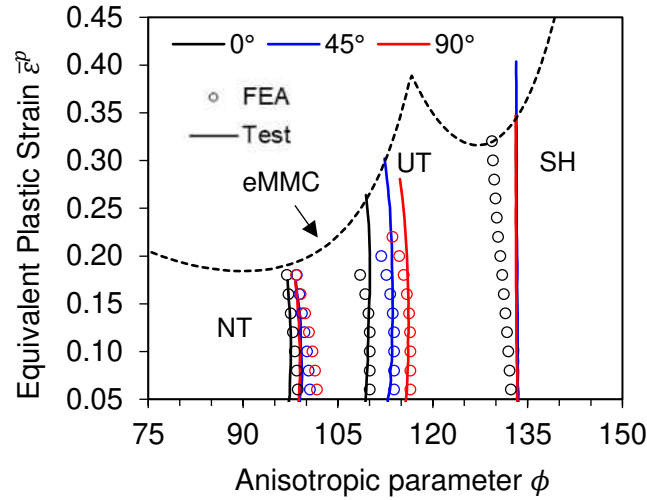


Figure 3-23. FEA results of strain paths to fracture for uniaxial tension, plane strain tension and shear tests

3.5 Discussions

In this work, shell elements are used for industrial applications due to the reasonable computational cost. Shell model solutions of large deformation problem are often as good as the solutions obtained with very fine solid element meshes unless necking occurs. The mesh size effect using shell element is a well-known issue in finite element modeling for ductile fracture. It is worth mentioning about the mesh size convergence issue in FE modeling by two sources: (1) the convergence issue introduced by spatial discretization in general finite element analysis and (2) the convergence issue related to the phenomenon of localized necking introduced by shell element. This can be best explained by our current work of using notch tension and shear tests. In notch tension tests, the FE simulation results are all the same before necking using different mesh sizes of 0.2, 0.5 and 1.0 mm. However, the force prediction diverges using shell element after localized

necking because plane stress assumption does not hold due to the hydrostatic pressure developed inside the neck. In shear test simulations, since the shear zone is very small due to the present sample design, the FE simulation results of mesh size 0.5 mm overestimated the test result for approximately 10%. The overestimation is not related with localized necking but simply due to the relatively large mesh used for spatial discretization of the localized shear zone. The maximal difference of the force-displacement response was less than 1% for element size 0.2 and 0.1 mm, suggesting that the FE solution was convergent.

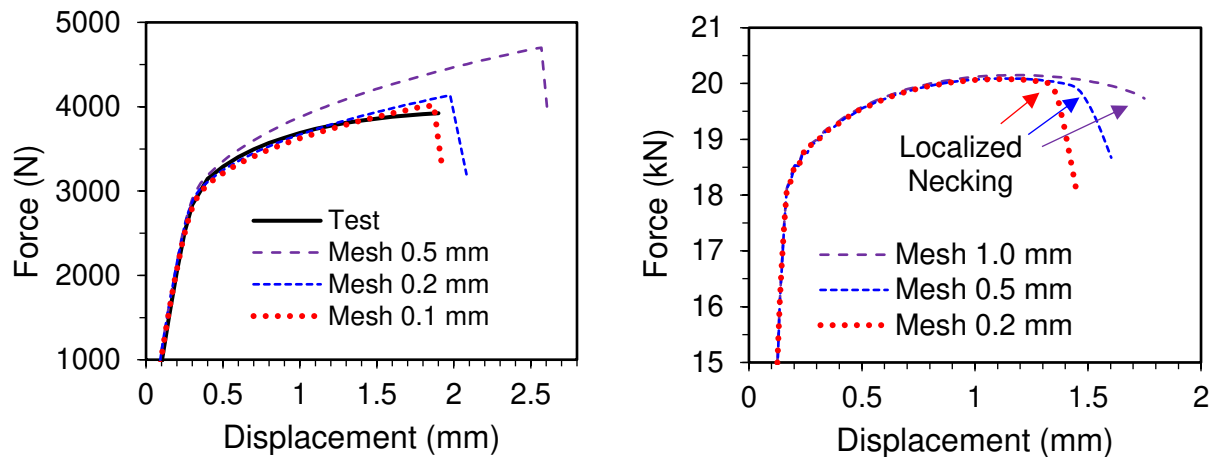


Figure 3-24. Mesh size effect in FE simulations of (a) shear test (b) uniaxial tension test.

The mesh size also affects the fracture strain. Mesh size may not be a sensitive issue for FE simulations at test coupon level because mesh sizes are very small (< 0.5 mm) compared to the mesh sizes used in practical applications (~ 5 to 10 mm) such as crashworthiness simulations. The problem of mesh size dependence on fracture strain has not been well understood, but it appears that mesh size regularization method provides a practical solution, which has been widely used and accepted in LS-DYNA. In addition, there also exists the size effect in DIC analysis of fracture strain. Experimental studies on different virtual strain gauge length (VSGL) suggest that the

fracture strain converges with respect to VSGL. Future work is necessary to address the effect of VSGL on fracture strain analysis in DIC and the mesh size dependence for fracture analysis in FE simulations.

CHAPTER 4 STRAIN RATE DEPENDENT FRACTURE MODELING OF ADVANCED HIGH STRENGTH STEELS

In this chapter, an extended rate-dependent MMC fracture model is proposed based on comprehensive quasi-static and high-speed fracture test data of four grades of advanced high strength steels (AHSS) sheets over a wide range of loading conditions. The new phenomenological fracture model aims to provide a bounded solution for modeling material fracture at high speed events within the range of low and intermediate strain rates for metal forming and crashworthiness applications. Finite element simulations are performed to correlate the test results under dynamic loading conditions.

4.1 Experimental Results and Analysis

This section presents the mechanical testing results of four grades of automotive AHSS sheets: QP980, MP980, DP1180 and PHS1300. AHSS grades contain significant alloying and two or more phases. AHSS are usually named in metallurgical designations providing the process information followed by the ultimate tensile strengths (UTS). Table 4-1 lists the four AHSS grades with tensile strength of 1000 MPa or above (also called “GigaPascal steels”) studied in this chapter. All the experimental results presented here are along the rolling direction of the AHSS sheet.

Table 4-1. AHSS sheets investigated in the present study

Steel Grade	Type of Steel	Tensile Strength (MPa)
QP980	Quenching and Partitioning steels	980
MP980	Multi-Phase steels	980
DP1180	Dual-Phase steels	1180
PHS1300	Press Hardened Steels	1300

4.1.1 Experiments at Quasi-static and High-speed Conditions

The AHSS sheets were tested by coupon specimens at both quasi-static and high-speed conditions. Figure 4-1 and Figure 4-2 show the schematic drawings of the coupon specimens of MP980, DP1180, PHS1300. The coupon specimen designs for QP980 are slightly different than the other three materials and are shown separately in Figure 4-3. In each test, 3-5 specimens were tested to ensure experimental reliability.

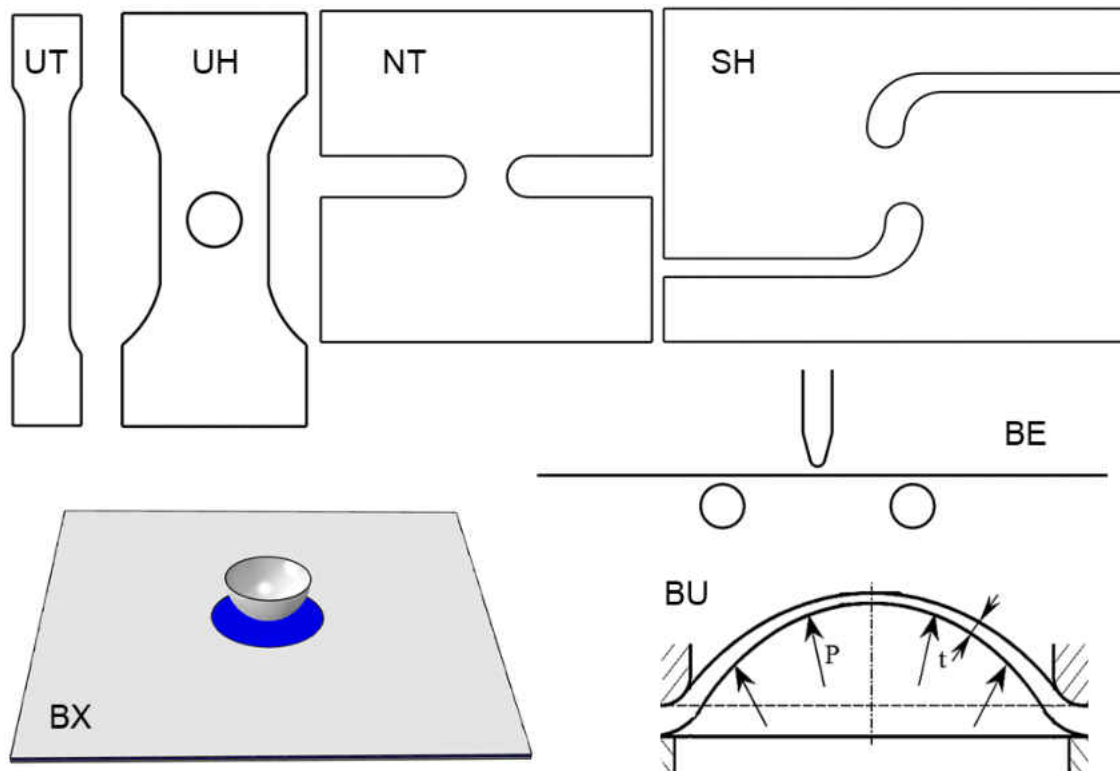


Figure 4-1. Schematic drawings of specimens tested under quasi-static conditions for MP980, DP1180 and PHS1300. (1) UT: uniaxial tension (2) UH: uniaxial tension with central hole (3) NT: notch tension (4) SH: shear (5) BX: biaxial punch (6) BE: plane strain bending (7) BU: hydraulic bulging.

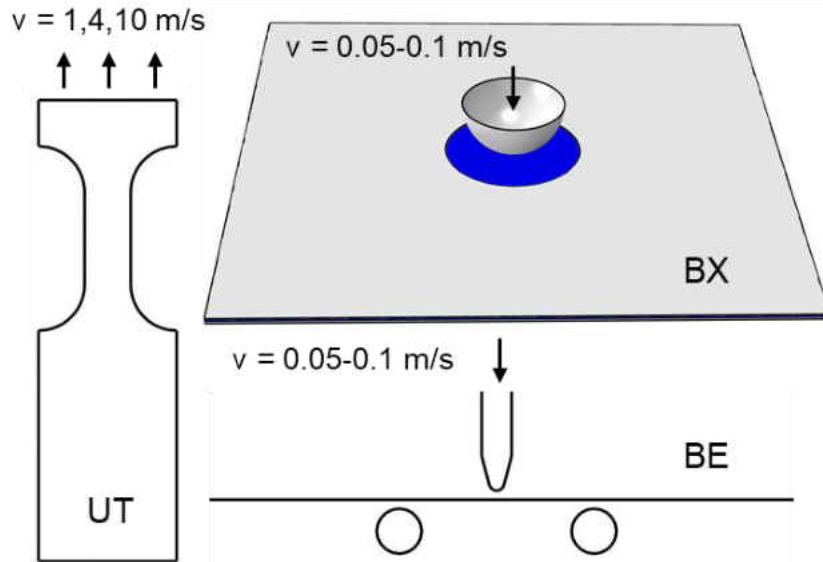


Figure 4-2. Schematic drawings of specimens tested under high-speed conditions for MP980, DP1180 and PHS1300. (1) UT: uniaxial tension (2) BE: plane strain bending (3) BX: biaxial punch.

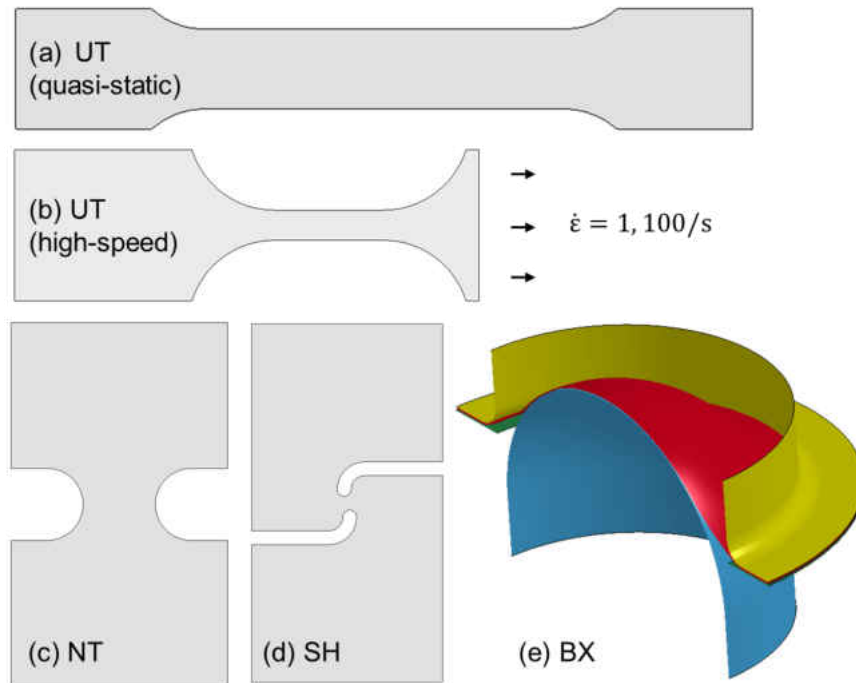


Figure 4-3. Schematic drawings of specimens tested under quasi-static and high-speed conditions for QP980. (a)(b) UT: uniaxial tension (c) NT: notch tension (d) SH: shear (e) BX: biaxial punch

The experiments of coupon samples at quasi-static conditions were conducted on universal testing machines. In the experiments, a stereo digital image correlation (DIC) system was used to in-situ measure the strain fields on the surface of the samples. The DIC system included a pair of CCD cameras operated at an adjustable low frame rate to allow sufficient resolution of strain states close to fracture. The testing machines and the DIC systems were triggered simultaneously at the beginning of each test, and the load signals measured in-situ by the load cells were continuously transferred into the DIC software to synchronize with the corresponding images during the tests.

The in-plane tests of coupon samples at high-speed conditions were conducted at different target effective strain rates on servo-hydraulic high-speed testing machines equipped with piezo load washers. The planar DIC systems equipped with a high-speed camera was used to capture the deformation and failure of the samples. The camera frame rate was set up to a high frequency with respect to the target strain rate to ensure the desired pixel resolution for fracture strain analysis. In order to record sufficient images for post-processing the strain close to fracture, the image acquisition was triggered by the rise of the force signals captured by the piezo load washer and thus the images can be synchronized with the force signals for DIC analysis.

Except for the in-plane tests, the AHSS sheets were also tested out-of-plane under bending, hydraulic bulge and punch tests. The hydraulic bulge tests were done at quasi-static loading condition only. The punch tests were carried out in a custom fixture equipped on the universal testing machine, or a Nakajima testing setup on a servo-hydraulic press. Due to the limitation of the universal testing machine and the servo-hydraulic press, the nominal effective strain rates were targeted at the order of magnitude of low strain rate $\dot{\epsilon} = 1 - 10/s$.

Table 4-2 summarizes the fracture tests of the four grades of AHSS sheets at quasi-static and high-speed conditions.

Table 4-2. Fracture test summary of AHSS sheets at quasi-static and high-speed conditions

Material	Fracture Tests	Test Condition	
		Quasi-static	High-speed
MP980 DP1180 PHS1300	(1) UT: uniaxial tension	$v = 0.1$ mm/s	$v = 1, 4, 10$ m/s
	(2) UH: uniaxial tension with central hole	$v = 0.05$ mm/s	×
	(3) NT: notch tension	$v = 0.01$ mm/s	×
	(4) SH: shear	$v = 0.005$ mm/s	×
	(5) BE: plane strain bending	$v = 0.1$ mm/s	$v = 50, 100$ mm/s
	(6) BU: hydraulic bulging	$P \approx 0.3$ MPa/s	×
	(7) BX: biaxial punch	$v = 0.1$ mm/s	$v = 50, 100$ mm/s
QP980	(1) UT: uniaxial tension	$v = 0.025$ mm/s	$v = 25, 2500$ mm/s
	(2) NT: notch tension	$v = 0.01$ mm/s	$v = 10, 1000$ mm/s
	(3) SH: shear	$v = 0.01$ mm/s	$v = 2.5, 250$ mm/s
	(4) BX: biaxial punch	$v = 0.25$ mm/s	$v = 25, 250$ mm/s

4.1.2 Experimental Results of Fracture Strain

The strain paths of all four loading conditions of QP980 at different strain rates are summarized in Figure 4-4. The quasi-static, slow and high speed dynamic test results are plotted by black, green and red lines respectively. For the same test, each repeat was represented by a specific line style. The test results show that when strain rate increases, the fracture strain drops significantly in uniaxial tension, but strain rate effect on fracture appears insensitive in other three loading conditions. Despite that the statistical differences in DIC analysis may be reduced in further analysis or cross-checked by physical measurement methods, the same conclusion is expected.

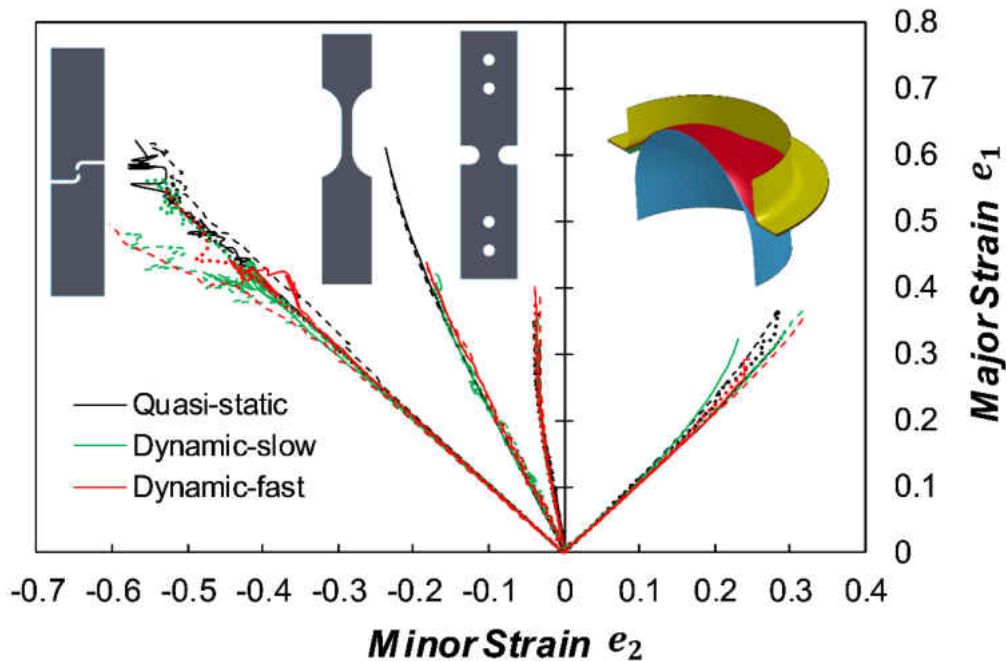


Figure 4-4. Strain paths for QP980 steel sheets at quasi-static, slow-speed and high-speed dynamic tests under different loading conditions (from left to right): (1) shear (2) uniaxial tension (3) notch tension (4) Nakazima punch test

Figure 4-5 to Figure 4-7 show the strain paths of quasi-static testing results of MP980, DP1180 and PHS1300. All test results are from the rolling direction of AHSS sheets. The strain path to fracture in each test was extracted from the critical location of the sample in the DIC analysis. The different test types are represented by different line colors. Five samples were tested for each test. The quasi-static tests cover a wide range of loading conditions from strain ratio $\alpha \approx -1$ (shear) to strain ratio $\alpha \approx +1$ (equi-biaxial tension). Except for the shear tests, the other six fracture tests can be divided into 3 groups: (1) Fracture under uniaxial tension loading condition characterized by uniaxial tension (UT) and uniaxial tension with central hole (UH) tests (2) Fracture under plane strain tension loading conditions characterized by the notch tension (NT) and plane strain bending (BE) tests (3) Fracture under biaxial tension characterized by hydraulic bulging (BU) and biaxial punch (BX) tests.

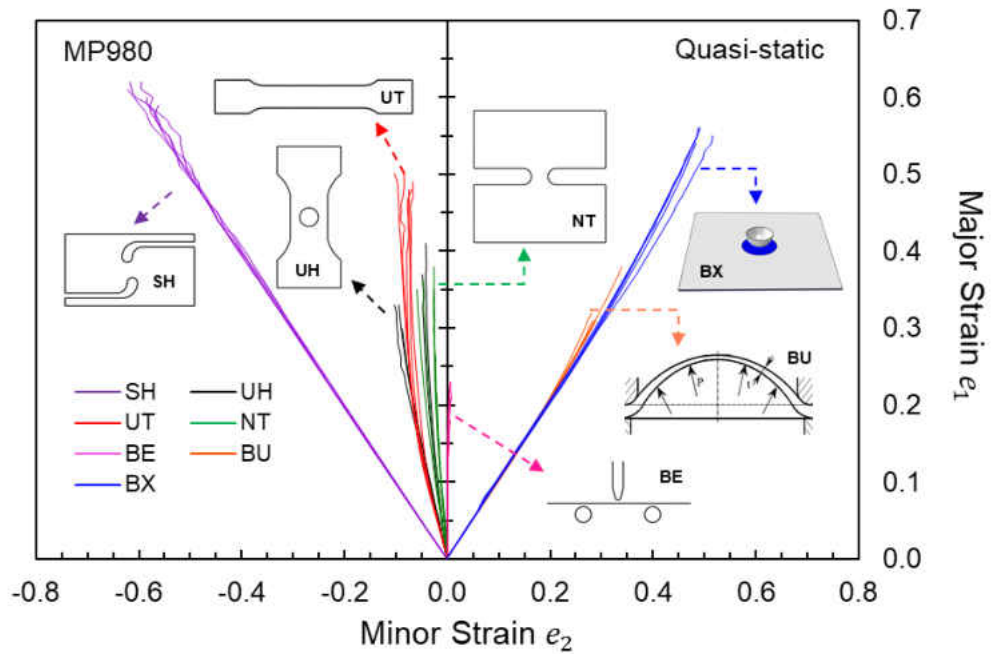


Figure 4-5. Strain paths to fracture for all 7 types of quasi-static tests of MP980: (1) SH: shear (2) UH: uniaxial tension with central hole (3) UT: uniaxial tension (4) NT: notch tension (5) BE: plane strain bending (6) BU: hydraulic bulging (7) BX: biaxial punch. The test results are along rolling direction of the samples.

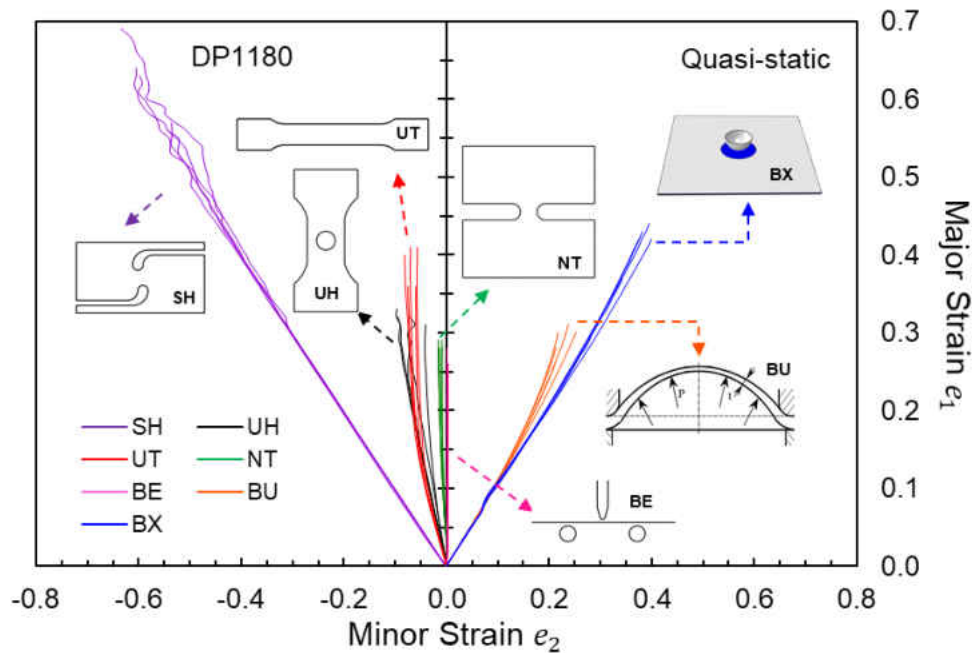


Figure 4-6. Strain paths to fracture for all 7 types of quasi-static tests of DP1180: (1) SH: shear (2) UH: uniaxial tension with central hole (3) UT: uniaxial tension (4) NT: notch tension (5) BE: plane strain bending (6) BU: hydraulic bulging (7) BX: biaxial punch. The test results are along rolling direction of the samples.

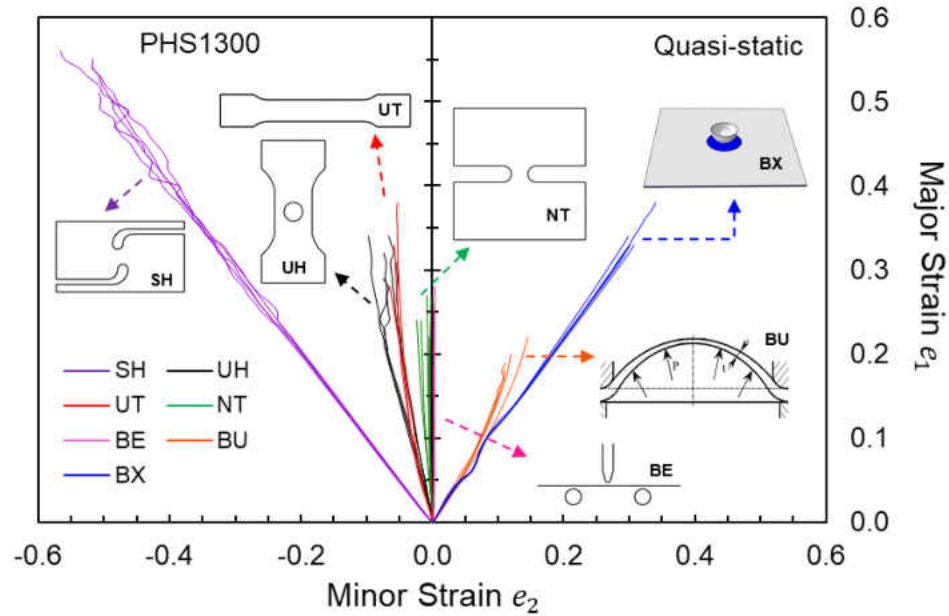


Figure 4-7. Strain paths to fracture for all 7 types of quasi-static tests of PHS1300: (1) SH: shear (2) UH: uniaxial tension with central hole (3) UT: uniaxial tension (4) NT: notch tension (5) BE: plane strain bending (6) BU: hydraulic bulging (7) BX: biaxial punch. The test results are along rolling direction of the samples.

For high-speed tests of MP980, DP1180 and PHS1300, the local fracture strain data were obtained from physical measurement of the fracture surfaces. Table 4-3 lists the analytical equations for fracture strain estimations from physical measurements.

Table 4-3. Local fracture strain estimation from physical measurements

Uniaxial tension	Plane strain bending	Punch test
$\bar{\epsilon}_f = \ln\left(\frac{w_0 t_0}{w_f t_f}\right)$	$\bar{\epsilon}_f = \frac{2}{\sqrt{3}} \ln\left(\frac{t_0}{t_f}\right)$	$\bar{\epsilon}_f = 2 \ln\left(\frac{R/t_0 + 1}{R/t_0 + 1/2}\right) + \ln\left(\frac{t_0}{t_f}\right)$

In Table 4-3, w_0 and w_f are the original and final widths of the uniaxial tension sample; t_0 and t_f are the original and failure thickness of the AHSS sheet at the fracture location; and R is the radius of the punch.

The fracture strain data of high-speed tests for MP980, DP1180 and PHS1300 are shown in Figure 4-8 to Figure 4-10. In each figure, the equivalent plastic strain data are shown in plot (a).

For high-speed bending and biaxial punch tests, since no strain paths are available from DIC analysis, the equivalent plastic strain data from physical measurement were converted to the principal strains by assuming the same strain ratio as in the quasi-static tests. For high-speed tension tests, the fracture strain data from DIC analysis and physical measurement are compared in plot (c) and (d). The stress triaxialities were calculated correspondingly under the assumption of linear strain path and associated flow rule. Note that the nominal strain rate ranges are different for the high-speed tests conducted on different testing machines: (1) low strain rate range ($\dot{\epsilon} = 1 - 10/s$) for high-speed bending and punch tests and (2) intermediate strain rate range ($\dot{\epsilon} = 50 - 500/s$) for high-speed tension tests. The nominal strain rates of high-speed bending and punch tests are the average strain rates obtained from the local fracture strain divided by the total time to fracture, while the nominal strain rates of high-speed tension tests are uniformly distributed over the gauge section of the sample.

The fracture data of high-speed tension tests obtained from physical measurement are consistent with DIC analysis results for MP980 and PHS1300. For DP1180, the fracture strain obtained from physical measurement are smaller than those from DIC analysis. In addition, for all three materials, the fracture strain values from high-speed bending tests appear underestimated by the analytical equation in Table 4-3. This may be attributed to the inhomogeneous strain distribution through the thickness direction during the plane strain bending tests.

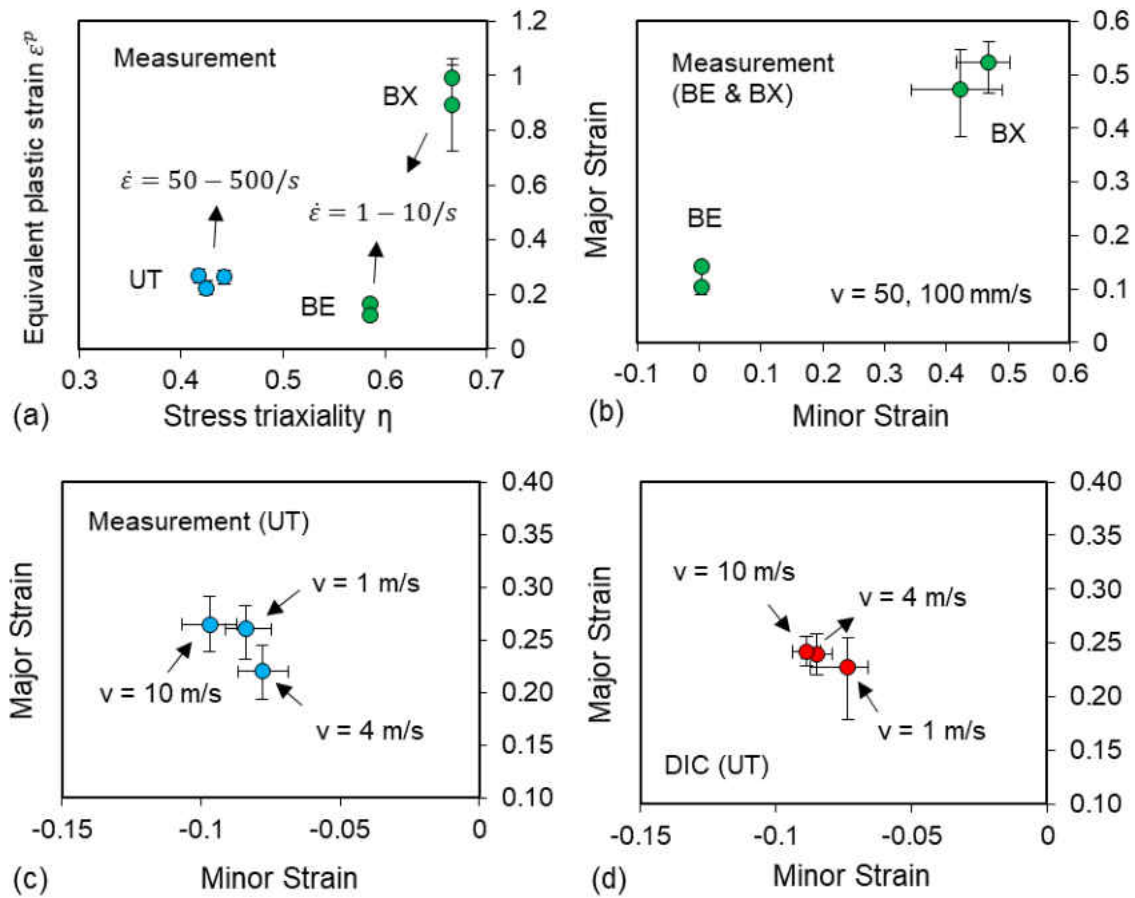


Figure 4-8. Fracture strain for high-speed uniaxial tests of MP980 (a) fracture strain from physical measurement (b) fracture strain from physical measurement of bending (BE) and punch (BX) tests (c) fracture strain from physical measurement of uniaxial tension (UT) tests (d) fracture strain from DIC analysis of uniaxial tension (UT) tests

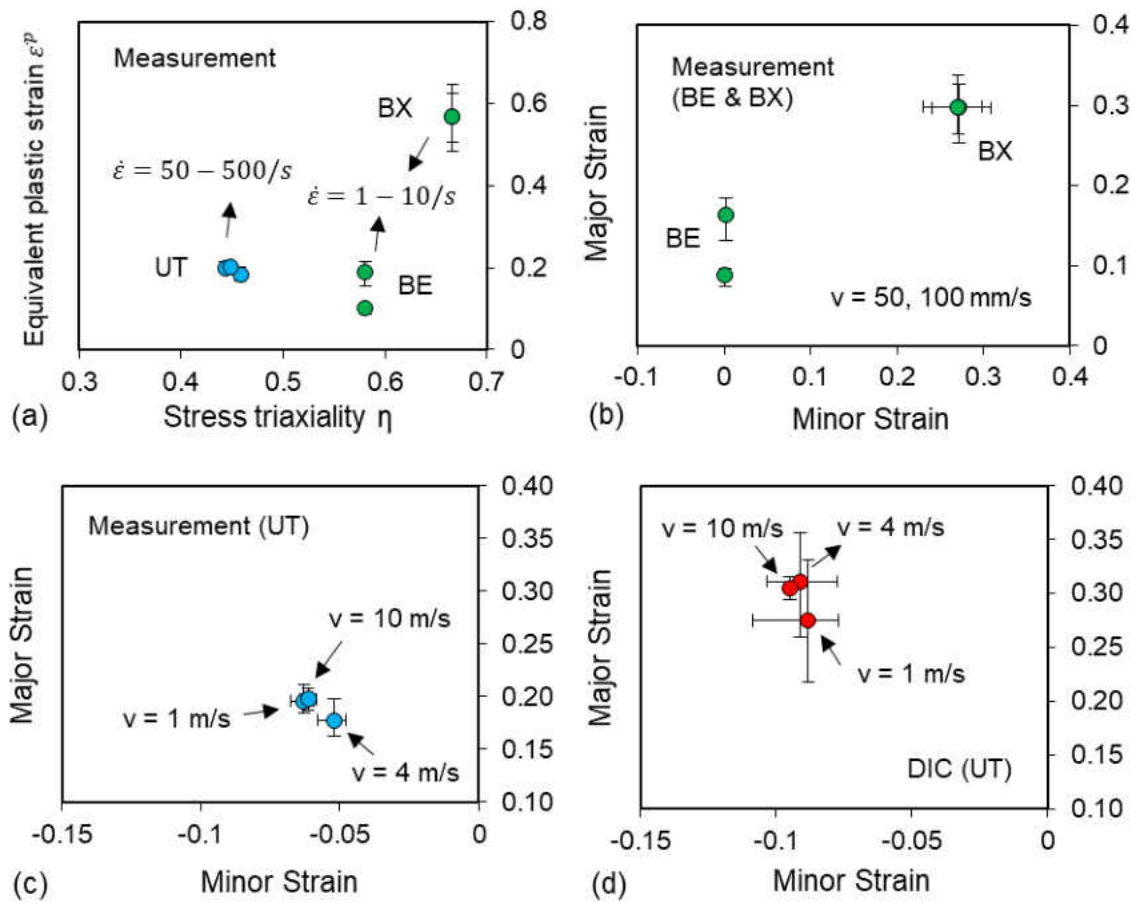


Figure 4-9. Fracture strain for high-speed uniaxial tests of DP1180 (a) fracture strain from physical measurement (b) fracture strain from physical measurement of bending (BE) and punch (BX) tests (c) fracture strain from physical measurement of uniaxial tension (UT) tests (d) fracture strain from DIC analysis of uniaxial tension (UT) tests

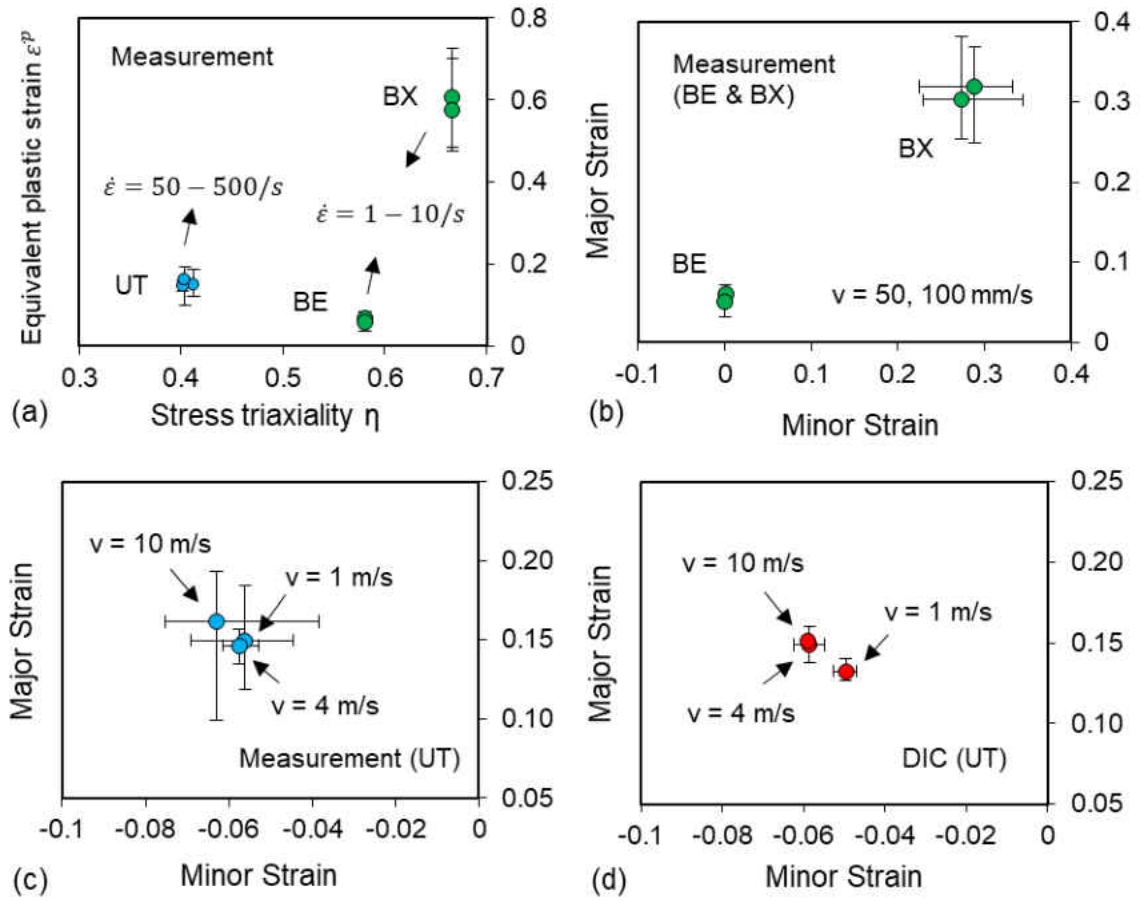


Figure 4-10. Fracture strain for high-speed uniaxial tests of PHS1300 (a) fracture strain from physical measurement (b) fracture strain from physical measurement of bending (BE) and punch (BX) tests (c) fracture strain from physical measurement of uniaxial tension (UT) tests (d) fracture strain from DIC analysis of uniaxial tension (UT) tests

4.2 Rate-dependent MMC Model and Fracture Strain Analysis

The material model presented in this section will serve as an efficient solution for the rate-dependent fracture problems in metal sheet stamping and full vehicle crashworthiness simulations.

The MMC fracture locus at quasi-static condition based on work of Bai and Wierzbicki (2010) reads

$$\bar{\varepsilon}_f(\eta, \bar{\theta}) = \left\{ \frac{A}{C_2} \left[C_\theta^s + \frac{\sqrt{3}}{2 - \sqrt{3}} (C_\theta^{ax} - C_\theta^s) \left(\sec \frac{\bar{\theta}\pi}{6} - 1 \right) \right] \left[\sqrt{\frac{1 + C_1^2}{3}} \cos \frac{\bar{\theta}\pi}{6} + C_1 \left(\eta + \frac{1}{3} \sin \frac{\bar{\theta}\pi}{6} \right) \right] \right\}^{\frac{1}{n}} \quad (4-1)$$

Under plane stress condition, Lode angle $\bar{\theta}$ and stress triaxiality η are uniquely linked by

$$\bar{\theta} = 1 - \frac{2}{\pi} \arccos \left[-\frac{27}{2} \eta \left(\eta^2 - \frac{1}{3} \right) \right] \quad (4-2)$$

The MMC fracture model is extended to a rate-dependent fracture model, by introducing a sigmoid function (or reversed ‘‘S-curve’’) $g(\dot{\varepsilon})$ as follows

$$g(\dot{\varepsilon}) = s_0 + \frac{s_d}{1 + e^{-s_c \dot{\varepsilon}}} \quad (4-3)$$

The fully-uncoupled rate-dependent MMC fracture model then becomes

$$\bar{\varepsilon}_f(\eta, \dot{\varepsilon}) = \bar{\varepsilon}_f(\eta) g(\dot{\varepsilon}) \quad (4-4)$$

The S-curve model $g(\dot{\varepsilon})$ is schematically shown in Figure 4-11. The S-curve $g(\dot{\varepsilon})$ smoothly decreases from an upper bound of $(s_0 + s_d)$ to a lower bound of $(s_0 + s_d/2)$. The rate-dependent fracture solution is now well-bounded from quasi-static to intermediate strain rate for a variety of modeling applications. The trend of the S-curve interprets such experimental phenomena over a wide range of strain rates that (1) at low strain rate range (0.1-10/s), material fracture strain decreases slowly with increasing strain rate; (2) at intermediate strain rate range (10-1000/s), the fracture strain drops significantly but gradually saturated toward the lower bound; (3) at high strain

rate range ($>10^3/s$), fracture strain ceases to decrease and maintain a constant value. The S-curve prediction is in a general consistency with the present fracture data of QP980 steel, particularly for high speed uniaxial tension and punch tests in two different strain rate ranges.

Another advantage of S-curve model is that, if compared to Johnson-Cook (J-C) damage model with strain rate dependent term only, the S-curve model is capable of predicting realistic material fracture in high speed deformation scenarios. As shown in Figure 4-11 (c), the strain rate dependent J-C fracture model predicts linear behavior in semi-log scale plot and the fracture limit is not bounded at high strain rate. This behavior may lead to unrealistic fracture prediction in finite element simulations. For example, in a forming or high velocity impact event, the local strain rate within an element does not remain constant during deformation and increases dramatically after the onset of necking. It is very likely to predict early fracture either if the model is unable to predict less ductility loss at low strain rate range, or if the model is not bounded at high strain rate range.

In Eq. (4-3) and (4-4), the strain rate term $g(\dot{\epsilon})$ is fully decoupled from $\bar{\epsilon}_f(\eta)$. In other words, the same magnitude of ductility loss applies to all stress states. Such an assumption is reasonable for a quick assessment for fracture model implementation from limited amount of test data, for instance, if only high speed tension is available. Nevertheless, in fact, the fracture data have demonstrated that for the present QP980 steel, strain rate does not cause ductility loss in other loading conditions than uniaxial tension. Therefore, a coupled rate-dependent MMC fracture model is tentatively proposed here to mathematically describe the experimental phenomenon, by assuming another piecewise sigmoid function $h(\bar{\theta})$ coupled with strain rate:

$$h(\bar{\theta}) = \begin{cases} 0, & \bar{\theta} \leq 0 \\ \frac{1}{1 + \left(\frac{\bar{\theta}}{1 - \bar{\theta}}\right)^{-\beta_h}}, & \bar{\theta} > 0 \end{cases} \quad (4-5)$$

The coupled strain rate dependent MMC fracture model then becomes a *double-S-curve* model as indicated in Eq. (4-6).

$$g(\dot{\epsilon}, \bar{\theta}) = s_0 + \frac{s_d}{1 + e^{-s_c h(\bar{\theta}) \dot{\epsilon}}} \quad (4-6)$$

The function $h(\bar{\theta})$ plot is shown in Figure 4-11(d). Here, $h(\bar{\theta})$ is chosen from zero to unity. The lower bound $h(\bar{\theta}) = 0$ indicates that for arbitrary strain rate, there is no ductility loss at this given stress state (e.g. $\bar{\theta} = 0$ for shear and $\bar{\theta} = -1$ for equi-biaxial tension). The upper bound $h(\bar{\theta}) = 1$ indicates that for the given stress state (e.g. $\bar{\theta} = 1$ for uniaxial tension), strain rate fully determines the ductility loss for the S-curve model by the original $g(\dot{\epsilon})$ in Eq.(4-3). Note that Eq.(4-2) can help to transfer $\bar{\theta}$ (in Eq.(4-6)) to η for plane stress conditions in implementation if needed.

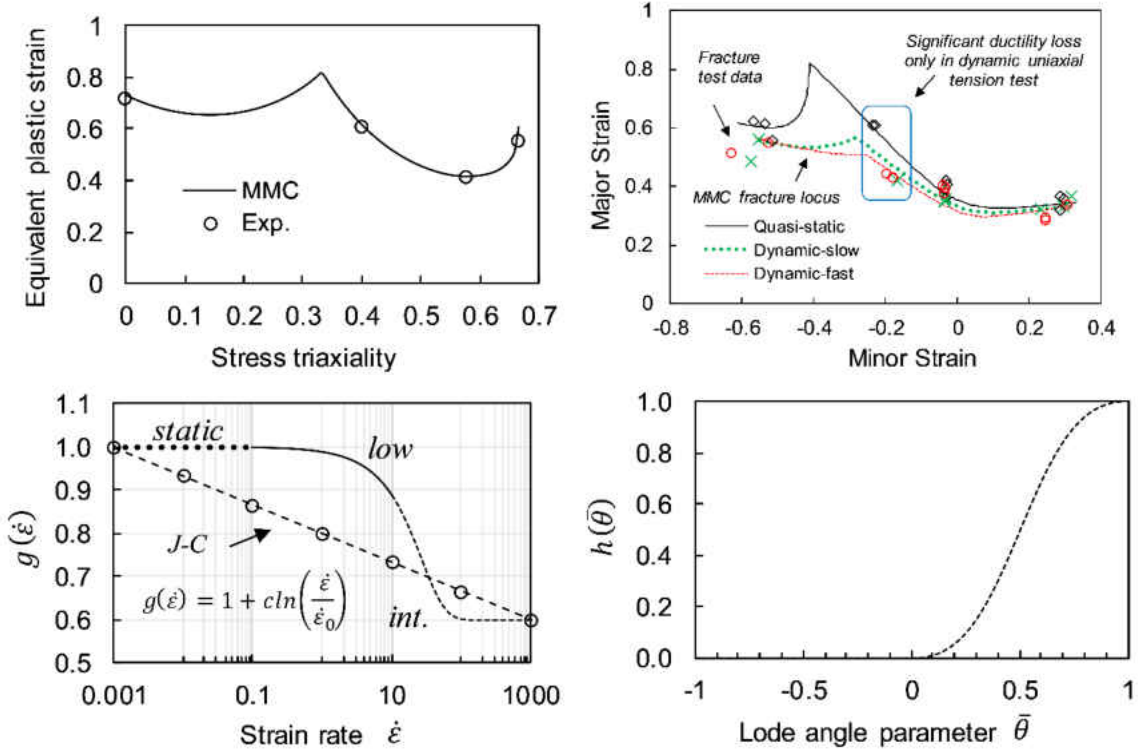


Figure 4-11. Fracture model plot for QP980: (a) MMC fracture locus at quasi-static condition (b) Fracture forming limit diagram (FFLD) at quasi-static and dynamic conditions in strain space (c) S-curve model $g(\dot{\epsilon})$ from quasi-static to intermediate strain rate and comparison with Johnson-Cook model (d) Lode angle coupling term $h(\bar{\theta})$ in Eq.(4-5).

The fully uncoupled and coupled rate-dependent MMC fracture model can be further viewed in 3D space in Figure 4-12. In case of the full uncoupled model, fracture strain drops equally for all stress states according to Eq.(4-3). On the contrary, the coupled model is bounded at shear ($\bar{\theta} = 0$) and equi-biaxial tension ($\bar{\theta} = -1$) for all strain rates investigated.

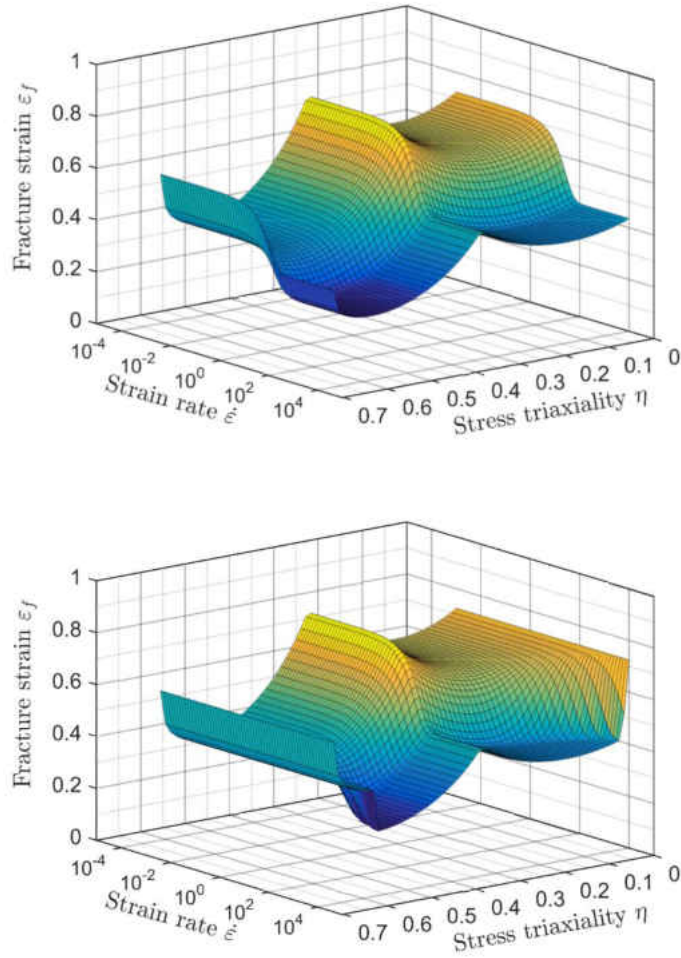


Figure 4-12. 3D fracture envelopes of QP980 under plane stress condition (a) Fully uncoupled rate-dependent MMC fracture model by Eq.(4-4). (b) Coupled rate-dependent MMC fracture model by replacing Eq.(4-4) with Eq.(4-6).

The rate-dependent MMC fracture models developed above were similarly applied for MP980, DP1180 and PHS1300. The high-speed test data for these three materials are not as comprehensive as QP980, hence only the fully decoupled S-curve model $g(\dot{\epsilon})$ in Eq.(4-3) was used to fit the available fracture test data. Figure 4-13 shows the S-curve model $g(\dot{\epsilon})$ fit with the test data of these three AHSS sheets in terms of equivalent plastic strain at fracture.

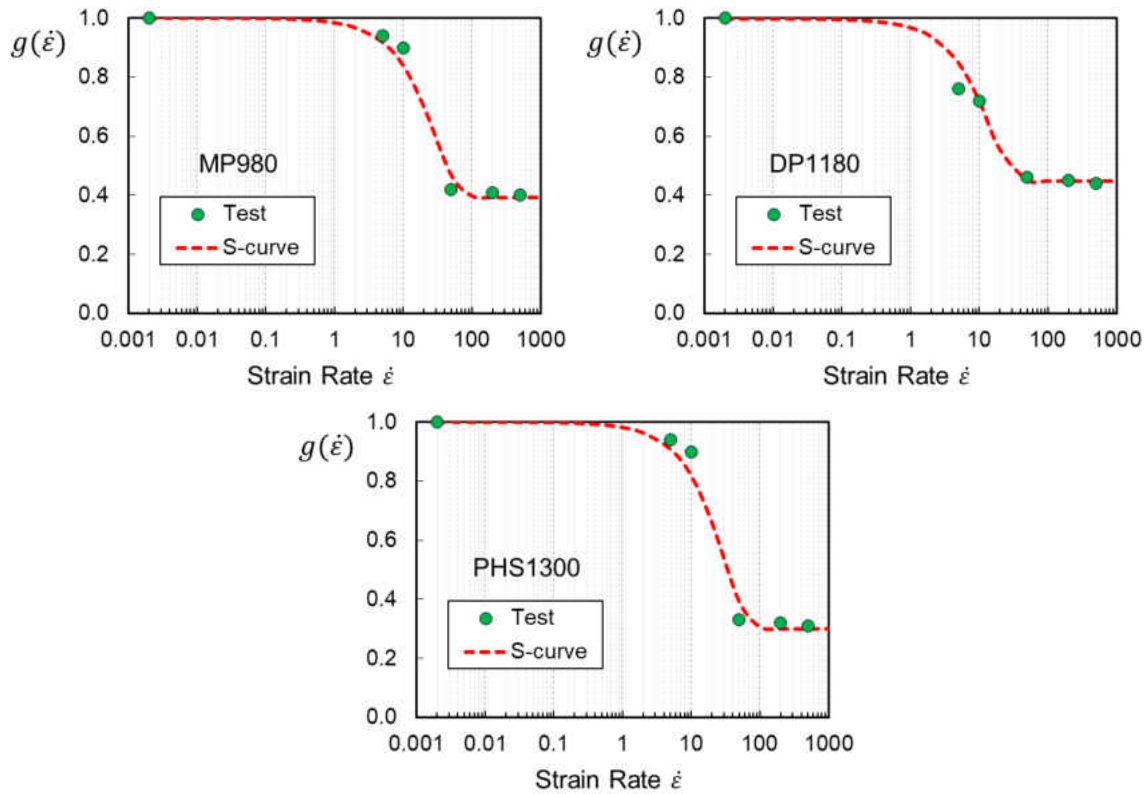


Figure 4-13. Full decoupled S-curve model $g(\dot{\epsilon})$ of MP980, DP1180 and PHS1300 from quasi-static to intermediate strain rate conditions

The full decoupled rate-dependent fracture forming limit diagrams (FFLD) and the corresponding MMC fracture loci for MP980, DP1180 and PHS1300 are shown from Figure 4-14 to Figure 4-19, respectively. Two representative rate-dependent fracture loci were plotted at two different strain rates: (1) Fracture locus within the low strain rate range ($\dot{\epsilon} = 1 - 10/s$) (2) Fracture locus within the intermediate strain rate range ($\dot{\epsilon} = 50 - 500/s$). The test data available for low strain rate range is the high-speed punch tests at punch speed of 50 and 100 mm/s. The test data available for the intermediate strain rate range is the high-speed tension tests at pulling speed of 1, 4, 10 m/s, which are faster than the quasi-static test speed by several order of magnitude. High-speed bending test results were not included in the figures due to the test data uncertainty.

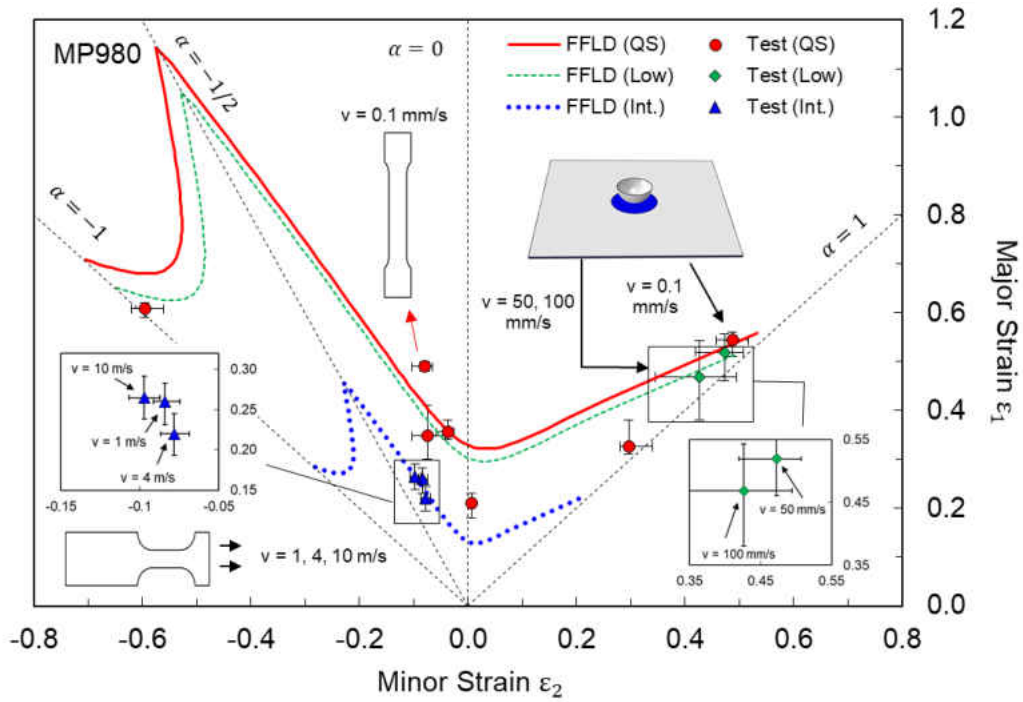


Figure 4-14. Fracture forming limit diagram (FFLD) of MP980 at (1) Quasi-static (QS) (2) Low strain rate and (3) Intermediate strain rate conditions. Strain ratio $\alpha = d\varepsilon_2/d\varepsilon_1$

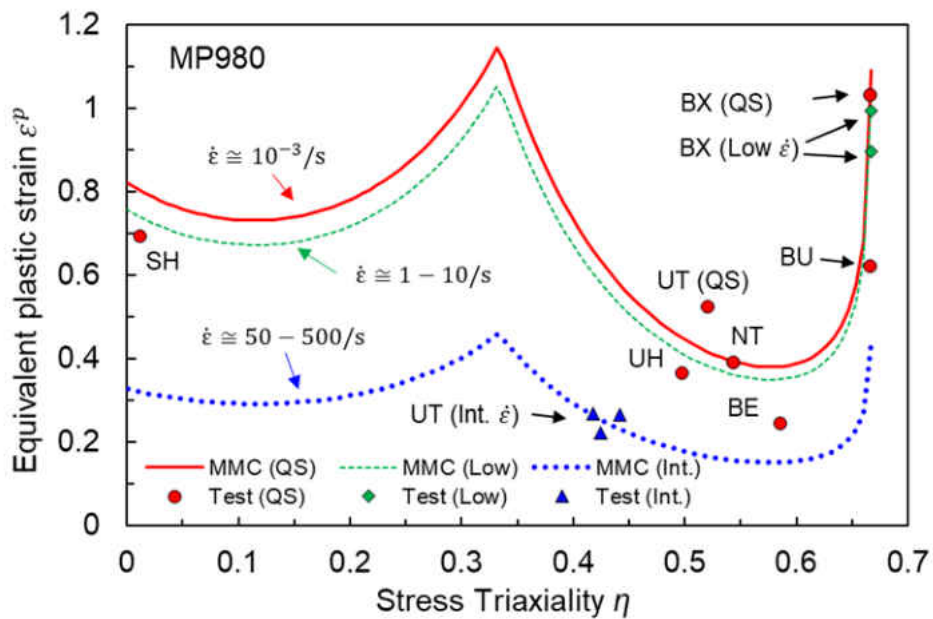


Figure 4-15. MMC fracture locus of MP980 at (1) Quasi-static (QS) (2) Low strain rate and (3) Intermediate strain rate conditions.

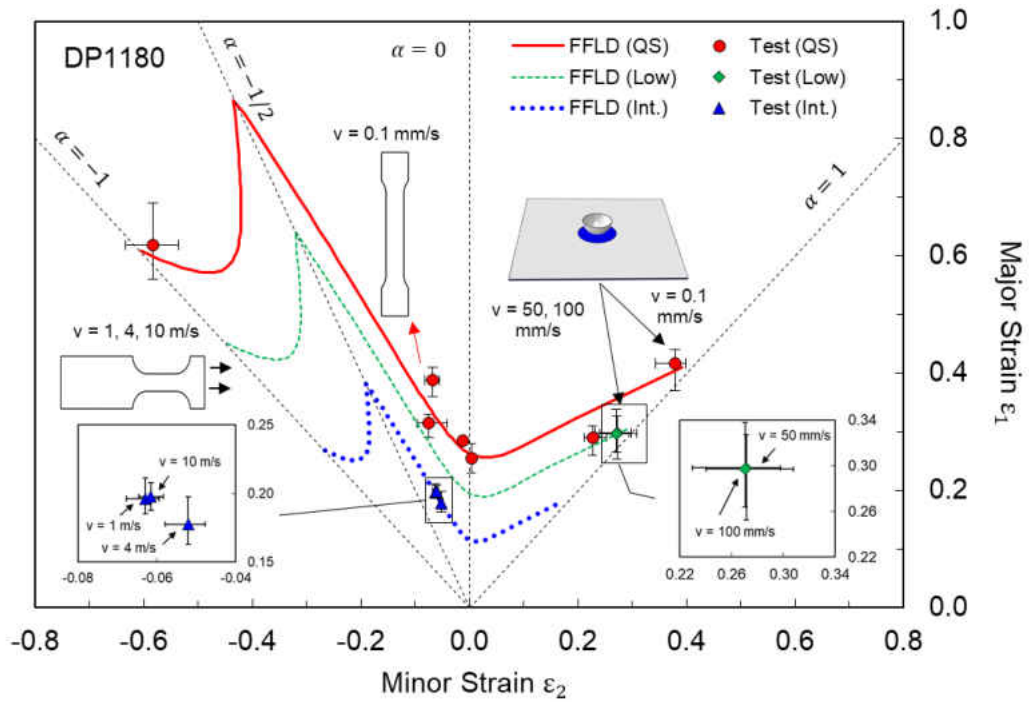


Figure 4-16. Fracture forming limit diagram (FFLD) of DP1180 at (1) Quasi-static (QS) (2) Low strain rate and (3) Intermediate strain rate conditions. Strain ratio $\alpha = d\varepsilon_2/d\varepsilon_1$

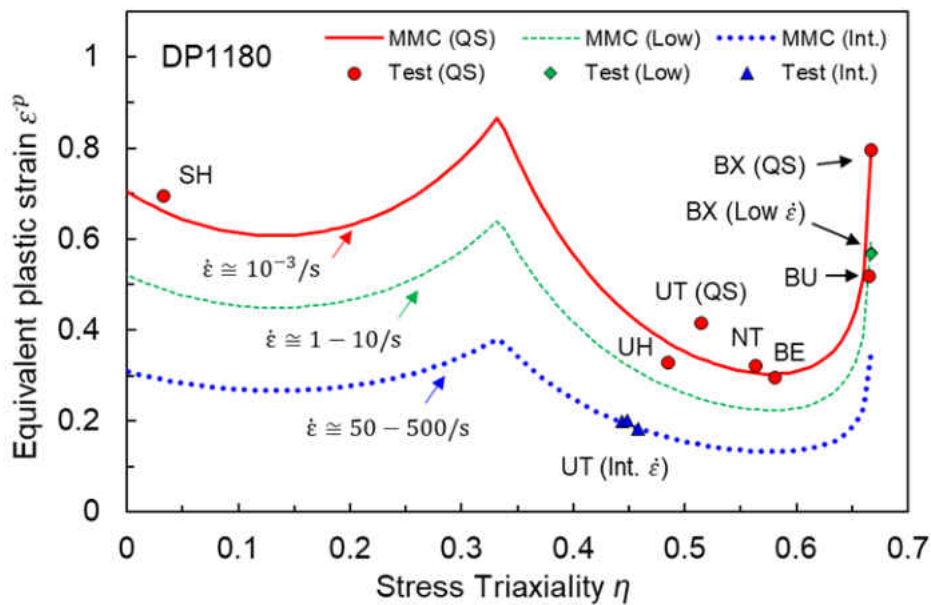


Figure 4-17. MMC fracture locus of DP1180 at (1) Quasi-static (QS) (2) Low strain rate and (3) Intermediate strain rate conditions.

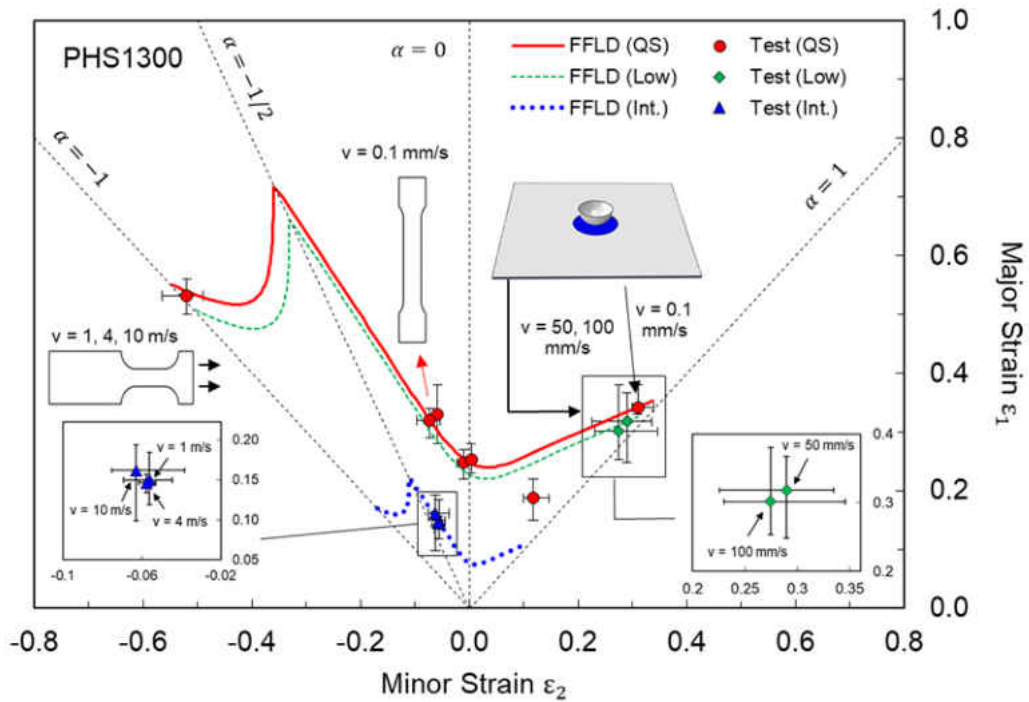


Figure 4-18. Fracture forming limit diagram (FFLD) of PHS1300 at (1) Quasi-static (QS) (2) Low strain rate and (3) Intermediate strain rate conditions. Strain ratio $\alpha = d\epsilon_2/d\epsilon_1$

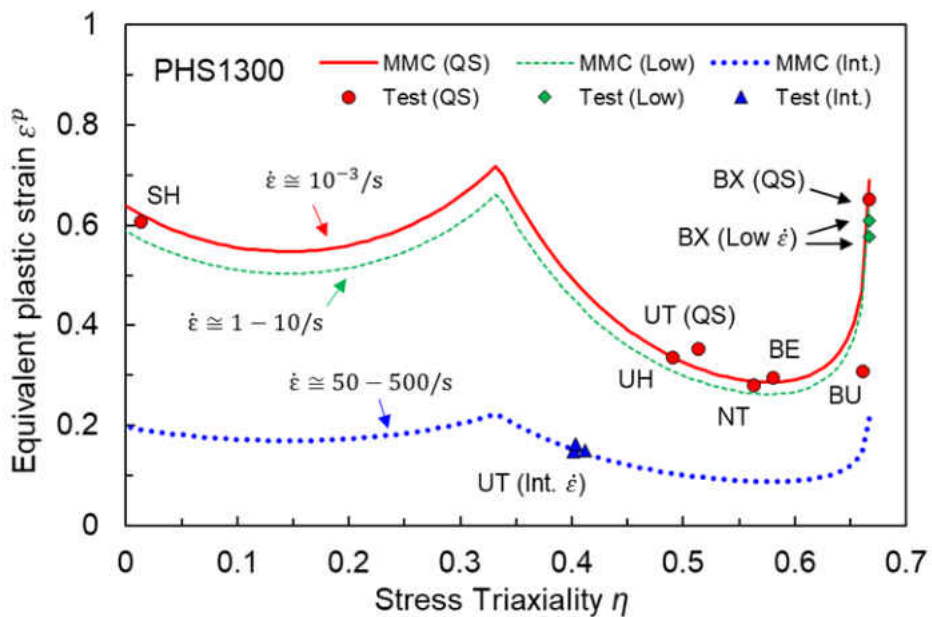


Figure 4-19. MMC fracture locus of PHS1300 at (1) Quasi-static (QS) (2) Low strain rate and (3) Intermediate strain rate conditions.

4.3 Finite Element Analysis of High-Speed Tests

This section presents the FE simulation results for high-speed tests of the AHSS sheets. The FE simulations were performed using the dynamic explicit solver in LS-DYNA. Test specimens were modeled using fully-integrated shell elements with five integration points assigned through the thickness direction. In order to model crack initiation, full size samples were modeled using the element erosion technique. Since the temperature dependent test data are not available, the thermal softening effect was not considered in FE simulations.

4.3.1 FE Simulation Results of QP980 sheets

This section presents the FE simulation results for high-speed uniaxial tension and punch tests of QP980. The strain rate effects of plastic hardening and fracture were modeled using keywords *MAT_024 and *MAT_ADD_DAMAGE_GISSMO. The mesh size was selected in accordance to the virtual strain gauge length (VSGL) from strain analysis in the DIC software.

In this work, only strain hardening effect was considered based on the available test data. The dynamic effects of strain rate hardening are modeled by Cowper-Symonds model:

$$\sigma = \sigma_0 \left[1 + \left(\frac{\dot{\epsilon}}{C} \right)^{1/P} \right] \quad (4-7)$$

The Cowper-Symonds model is a common and simple rate-dependent plasticity model for explicit dynamic simulations. σ_0 defines the hardening curve at quasi-static condition; and σ is the yield stress scaled with strain rate effect at dynamic condition. C and P are two material constants calibrated from uniaxial tension test results at different nominal strain rates.

The present QP980 sheet samples are in general isotropic. A linear combination of Swift-Voce hardening law is used here for determination of post-necking hardening before fracture. The model parameters were determined in a hybrid experimental-numerical approach.

$$\sigma_0(\bar{\varepsilon}_p) = \alpha[A(\varepsilon_0 + \bar{\varepsilon}_p)^n] + (1 - \alpha)[k_0 + Q(1 - e^{-\beta\bar{\varepsilon}_p})] \quad (4-8)$$

For modeling rate-dependent fracture, only the fully uncoupled strain rate dependent MMC fracture model were considered in FE simulations due to its simplicity. The material parameters of rate-dependent plasticity and fracture models are listed in Table 4-4.

Table 4-4. Plasticity and fracture parameters for QP980 steel

	<i>C</i>	<i>P</i>	<i>A</i>	<i>n</i>	ε_0	α	<i>k</i> ₀	<i>Q</i>	β
Plasticity parameters	6500	1.2	1750	0.215	0.008	0.6	654.6	559.5	14.98
	<i>A</i>	<i>n</i>	<i>c</i> ₁	<i>c</i> ₂	<i>c</i> _θ ^S	<i>c</i> _θ ^{AX}	<i>s</i> ₀	<i>s</i> _d	<i>s</i> _c
Fracture parameters	1750	0.215	0.13	955.4	1.008	1.038	1.4	-0.8	0.058

The FE simulation results are shown in Figure 4-20. The test results are denoted by lines and the FE simulation results are presented by scattered markers. In the uniaxial tension simulations, for quasi-static and slow speed conditions, the FE results show slight differences than the test results. However, at intermediate strain rate, the difference becomes noticeable: the FE result predicted longer elongation until fracture after the onset of necking. This difference is mainly because in the FE model, only strain rate hardening effect was considered, and the thermal softening effect was neglected. In real high speed tension tests, the strain rate is sufficiently high to generate adiabatic heating in the localized necking zone. The deformation-induced thermal softening effect will decrease the flow stress and promote earlier fracture (Wagoner & Chenot, 1996). Special attention is drawn to the readers that for high speed tension, despite that the uniform elongation is much longer than quasi-static and slow speed tension, the local fracture strain is still

lower as in FE model input. Fracture is a local phenomenon rather than an average response over a wide gauge area on the sample.

In the punch test simulations, as punch speed increases, the strain rate hardening effect is similarly observed as in uniaxial tension. For both experiments and simulations of the highest speed punch tests ($v = 250$ mm/s), the punch stroke at fracture is smaller than those at the slow speeds. The results are expected because when strain rate increases, the strain rate dependent MMC fracture model predicts lower fracture strain. However, the ductility loss in high-speed punch is only marginal. Unlike in high-speed tension tests, the nominal strain rates in high-speed punch tests are within low strain rate range.

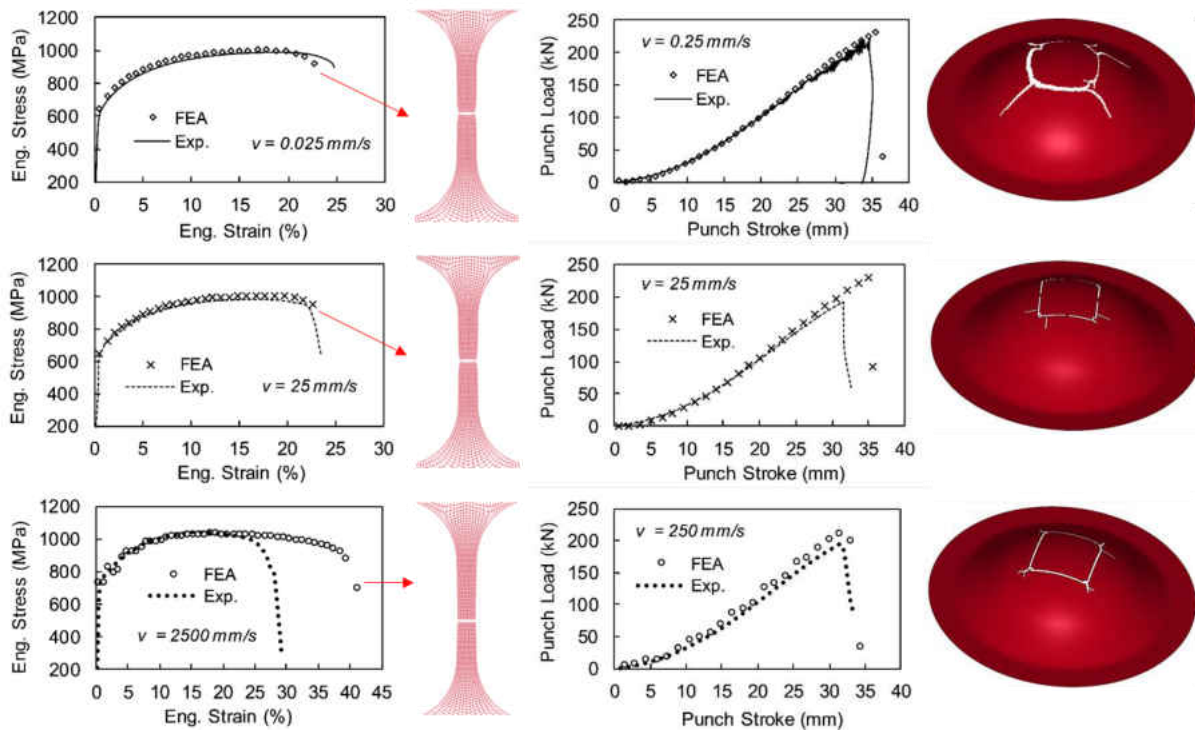


Figure 4-20. FEA results of (left) uniaxial tension and (right) punch tests of QP980 sheets at different speeds

The loading path histories were extracted from critical elements at fracture initiation in the FE simulations. Figure 4-21 shows the evolution of equivalent strain with respect to strain rate and stress triaxiality in a 3D space. For a given loading condition, the evaluation of triaxiality η is almost the same at different strain rates. For example, in uniaxial tension, triaxiality η started at 1/3 during uniform deformation, and then shifted to 0.4-0.5 after the onset of necking. In punch test modeling, triaxiality of the critical element remained close to 2/3 during punch stroke, which implies a proportional loading condition along equi-biaxial tension.

The effect of strain rate evolution during plastic deformation is more pronounced. Despite that constant velocities were applied as boundary conditions, the local strain rates of the critical elements increased dramatically even by one order of magnitude. For example, in high speed tension tests, the nominal strain rate is targeted at 100/s. But the actual local strain rate of the critical element changed approximately from 50/s to 500/s before fracture. Therefore, the FE results shed light on the importance of the proposed S-curve model. The bounded smooth S-shape curve model represents its capability of producing realistic simulation results for fracture model with element erosion.

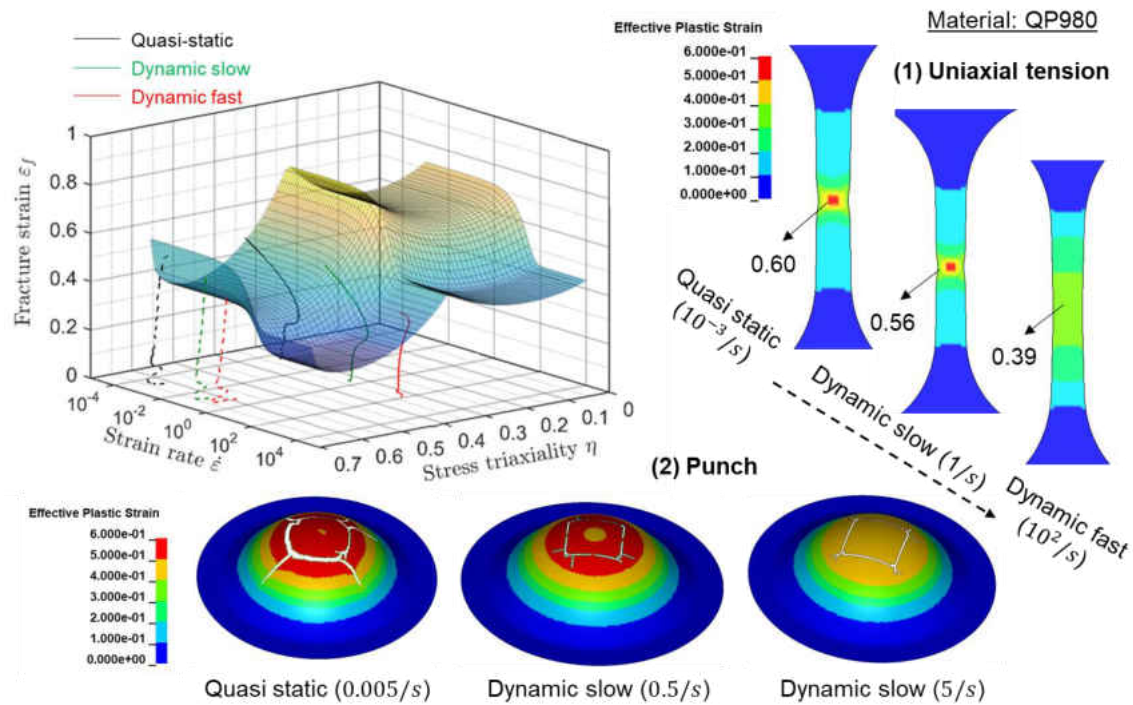


Figure 4-21. FEA results of rate-dependent loading paths to fracture of QP980 for uniaxial tension (solid lines) and punch (dashed lines) tests at 3 different speeds: quasi-static (black), slow speed (green) and high speed (red). Note that the strain rate range for the highest speed of uniaxial tension (intermediate $\dot{\epsilon}$) is different than punch test (low $\dot{\epsilon}$).

4.3.2 FE Simulation Results of MP980, DP1180 and PHS1300 sheets

Similar modeling approach was applied to the other AHSS sheets: MP980, DP1180 and PHS1300. The FE simulations were carried out for (1) uniaxial (2) plane strain bending and (3) punch tests by dynamic explicit analysis in LS-DYNA. Test specimens were modeled using fully-integrated shell elements (ELFORM = 16) with five integration points assigned through the thickness direction. The strain rate effects of plastic hardening and fracture were modeled using keywords *MAT_224. In *MAT_224, the rate-dependent hardening curve input are effective stress versus effective plastic strain at different strain rates as shown in Figure 4-22. Since the

temperature dependent test data are not available, the thermal softening effect was not considered in FE simulations.

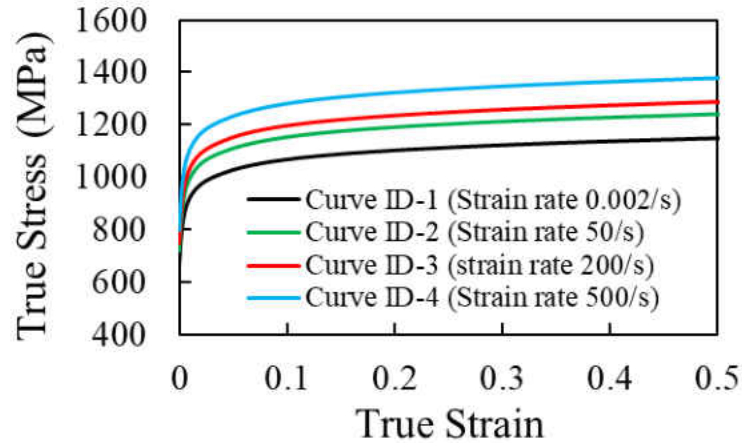


Figure 4-22. An example (MP980) of rate-dependent hardening curve input by *MAT_224 in LS-DYNA

The rate-dependent plasticity and fracture behavior were modeled using the Cowper-Symonds model in Eq.(4-7) and the fully uncoupled rate-dependent fracture model in Eq.(4-3). The material parameters of rate-dependent plasticity and fracture models of MP980, DP1180 and PHS1300 are summarized in Table 4-5. The plots of Figure 4-13 in Section 4.2 demonstrates the S-curve model $g(\dot{\epsilon})$ using the fracture parameters in Table 4-5.

Table 4-5. Plasticity and fracture parameters for MP980, DP1180 and PHS1300

Plasticity parameter	C	P	A	n	ϵ_0	α	k_0	Q	β
MP980	21362	2.30	1238	0.062	0.0001	0.7	893.2	166.9	32.47
DP1180	14976	2.05	1512	0.070	0.0001	0.5	1025.5	241.5	36.95
PHS1300	1565	0.45	1980	0.070	0.0001	0.0	1125.6	432.9	109.7
Fracture parameter	A	n	c_1	c_2	c_θ^s	c_θ^c	s_0	s_d	s_c
MP980	1238	0.062	0.049	655.8	0.9276	0.9996	1.608	-1.216	0.054
DP1180	1512	0.070	0.061	795.8	0.9324	1.0020	1.551	-1.103	0.111
PHS1300	1980	0.070	0.058	1025.4	0.9240	0.9996	1.701	-1.402	0.053

Figure 4-23 to Figure 4-25 show the FE simulation results of uniaxial tension tests for MP980, DP1180 and PHS1300. The test results are denoted by solid lines and the FE simulation results are shown as dashed lines. The FE simulation results predict the global force (or engineering stress) responses very well as compared to the test results. This is as expected because the rate-dependent Cowper-Symonds plasticity model was calibrated from the high-speed uniaxial tension results. The FE simulations predict late fracture for some cases (e.g. MP980-50/s). This is mainly because only strain rate hardening effect was considered in the model setup. In real high speed tension tests, adiabatic heating was generated in the localized necking zone and the thermal softening effect would decrease the flow stress and lead to earlier fracture after necking. In addition, despite that the global displacements to fracture are the greatest at the highest speed tests (i.e. nominal strain rate 500/s) for all 3 materials, the local fracture strain, on the other hand, is close to or smaller than the low strain speed test results (i.e. nominal strain rate 50/s).

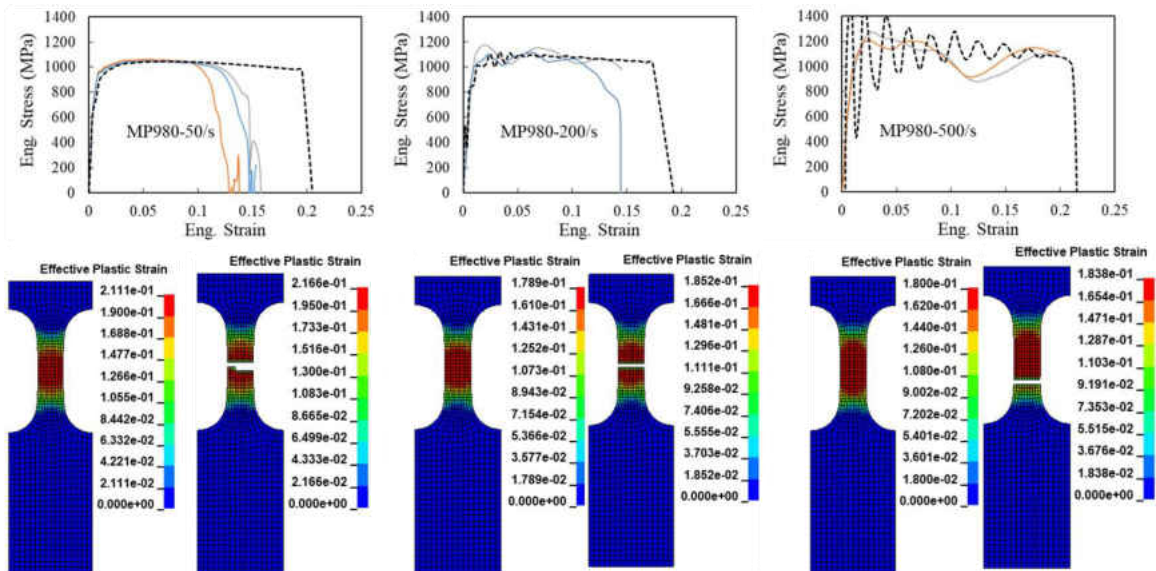


Figure 4-23. FEA results of high speed tests in uniaxial tension at different target nominal strain rates for MP980. The test results are shown in solid lines and the FEA results are shown in dashed lines.

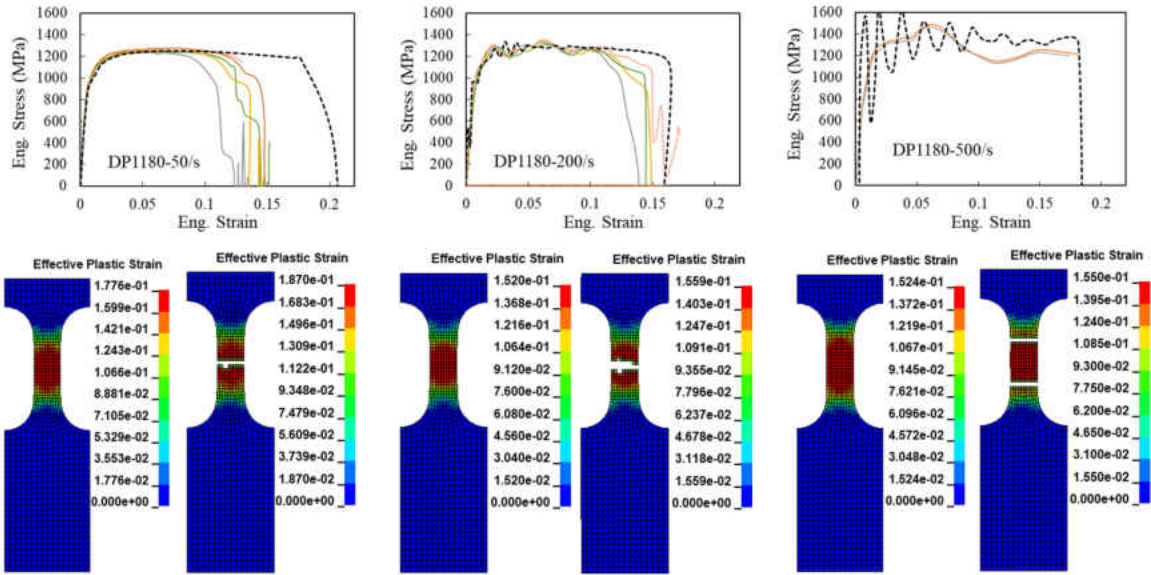


Figure 4-24. FEA results of high speed tests in uniaxial tension at different target nominal strain rates for DP1180. The test results are shown in solid lines and the FEA results are shown in dashed lines.

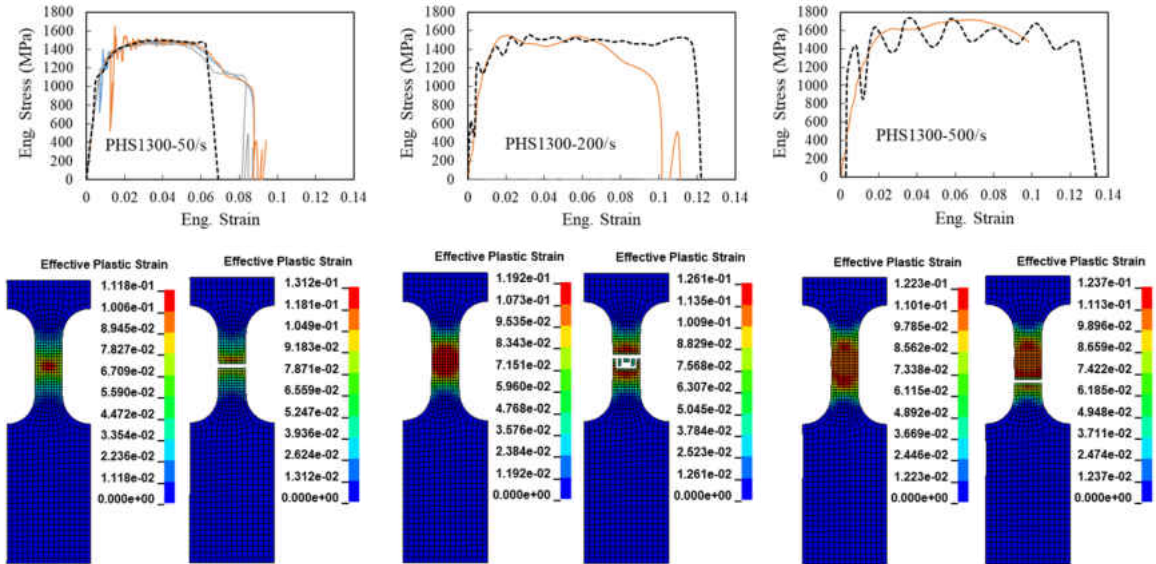


Figure 4-25. FEA results of high speed tests in uniaxial tension at different target nominal strain rates for PHS1300. The test results are shown in solid lines and the FEA results are shown in dashed lines.

The FE simulation results of high-speed bending tests are shown in Figure 4-26 to Figure 4-28. The displacements at fracture initiation from FE simulations are consistent with the experimental results for all three materials. In FE simulations, fracture was initiated when the

integration point on the tensile bending surface failed, but elements were deleted after all integration points through thickness failed. In experiments, fracture initiation was determined from the DIC images by observation of multiple cracks on the tensile side of the blank during the bending tests. From the simulation results, it can be seen that the force responses are underestimated for the high speed bending tests. The force difference between FE simulations and experimental results may be explained by two possible factors: (1) the simple rate-dependent Cowper-Symonds model did not consider strain rate hardening coupling with the stress state. The Cowper-Symonds model was calibrated from high speed uniaxial tension tests so the rate-dependent hardening curves along plane strain tension may not follow the same scaling factor as in uniaxial tension. (2) the assumption of isotropic hardening may also account for discrepancy between the FE simulation and test results.

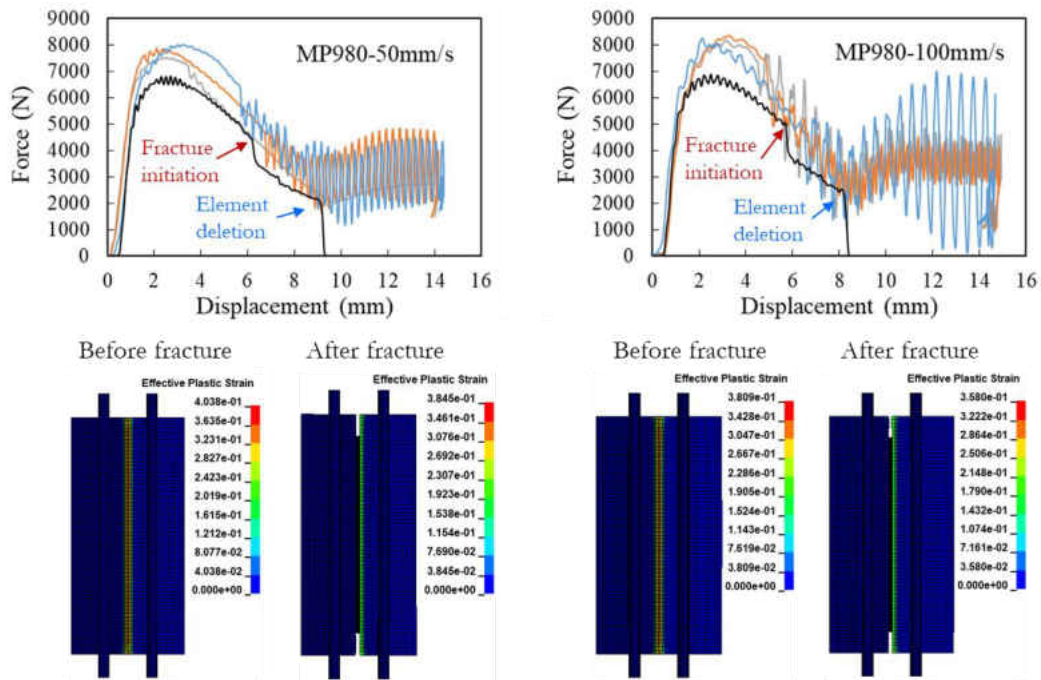


Figure 4-26. FEA results of high speed bending tests for MP980 at punch velocity of (a) 50 mm/s and (b) 100 mm/s. The test results are shown in color lines and the FEA results are shown in black lines.

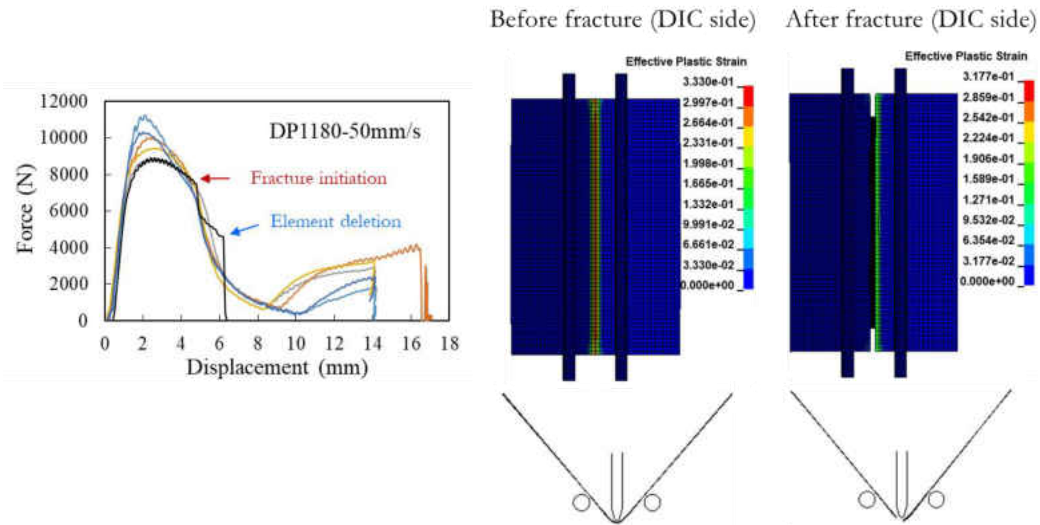


Figure 4-27. FEA results of high speed bending tests for DP1180 at punch velocity of 50 mm/s. The test results are shown in color lines and the FEA results are shown in black lines.

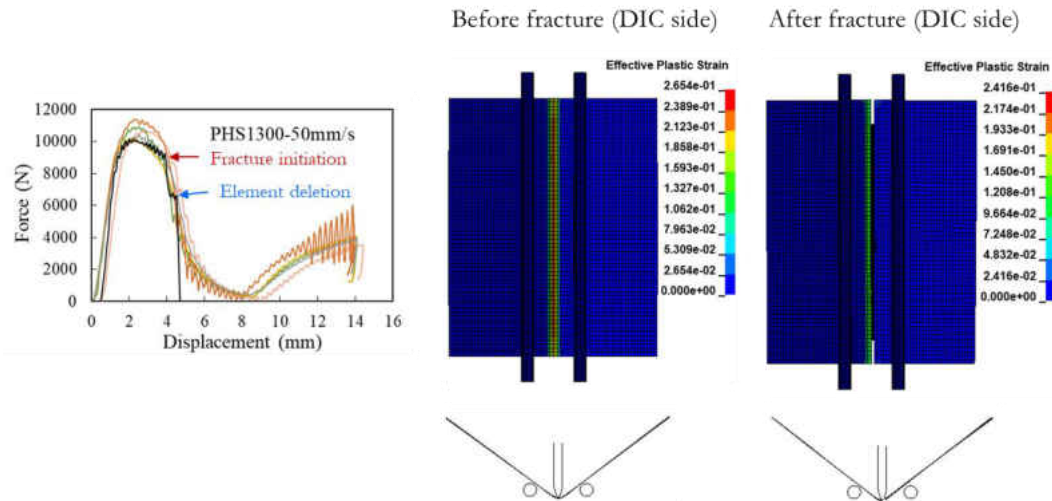


Figure 4-28. FEA results of high speed bending tests for PHS1300 at punch velocity of 50 mm/s. The test results are shown in color lines and the FEA results are shown in black lines.

The FE simulation results of high-speed punch tests are shown in Figure 4-29 to Figure 4-31. The FE simulation results agree well with experimental results of MP980. However, for DP1180 and PHS1300, the simulation results predicted greater punch loads and earlier fracture than experiments. The noticeable discrepancies obtained can be attributed to the similar factors as

discussed in high-speed bending simulations: (1) strain rate hardening not coupling with stress states and (2) the assumption of isotropic yield and isotropic hardening. For high-speed punch test simulations, the second factor may be more important in controlling the plastic flow between plane strain tension and equi-biaxial tension. In addition, thermal softening effect is another possible factor influencing the localized necking behavior of the AHSS sheets. In conclusion, the strain rate hardening and necking behavior under multi-axial stress states deserves further investigation on constitutive models with higher accuracy for FE simulations.

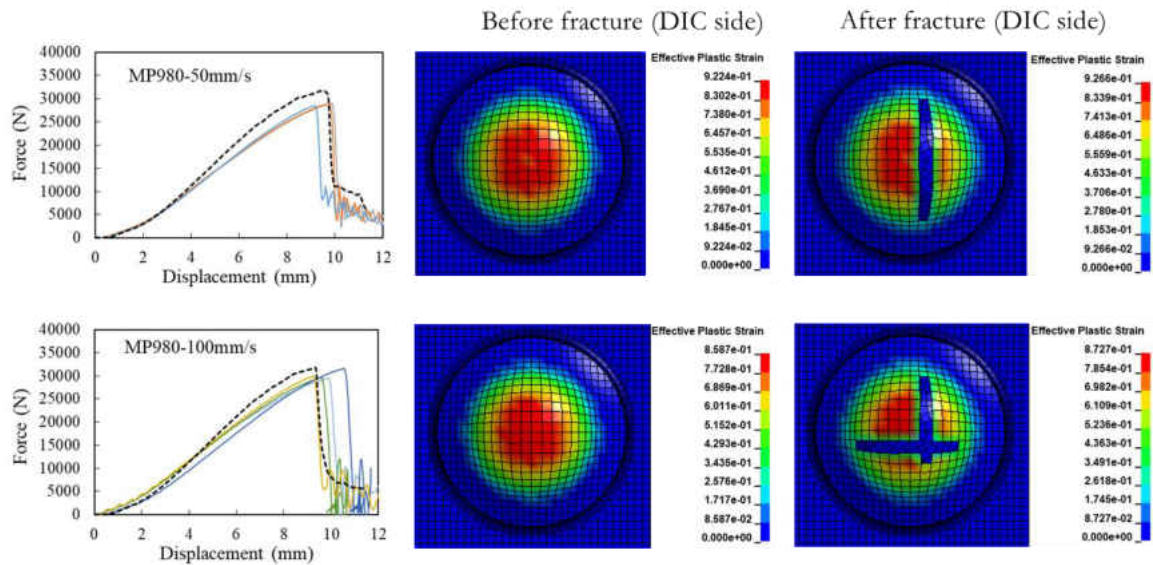


Figure 4-29. FEA results of high speed punch tests for MP980 at punch velocity of (a) 50 mm/s and (b) 100 mm/s. The test results are shown in solid lines and the FEA results are shown in dashed lines.

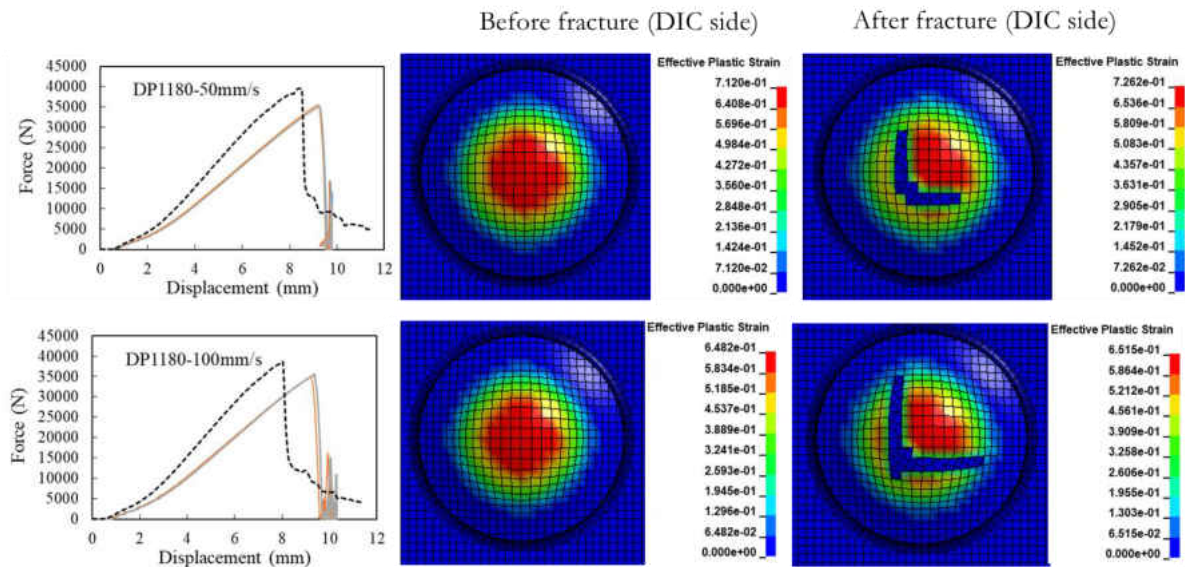


Figure 4-30. FEA results of high speed punch tests for DP1180 at punch velocity of (a) 50 mm/s and (b) 100 mm/s. The test results are shown in solid lines and the FEA results are shown in dashed lines.

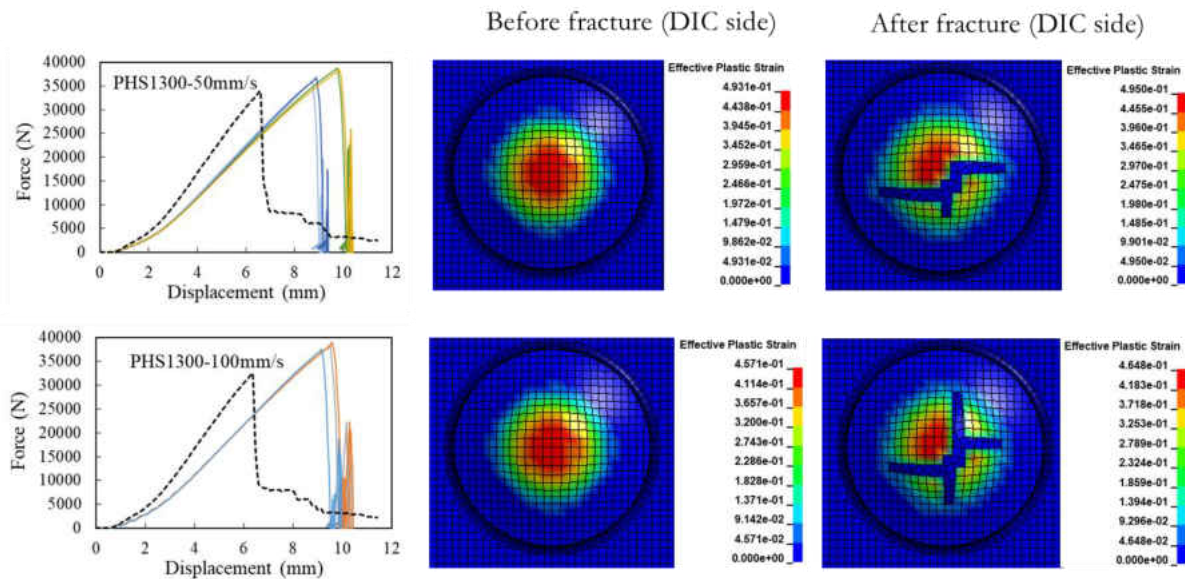


Figure 4-31. FEA results of high speed punch tests for PHS1300 at punch velocity of (a) 50 mm/s and (b) 100 mm/s. The test results are shown in solid lines and the FEA results are shown in dashed lines.

4.4 Discussions

In this work, only the strain rate effects were considered in modeling for simplicity. Temperature effects have been buried into the rate effects in the present plasticity and fracture models. However, it is well-known that at sufficient high strain rate, adiabatic heating induced from plastic deformation plays an important role on lowering material flow stress. The heat generated in localized neck of high strain has a detrimental effect on material formability and fracture (Sung et al., 2010). Research work on temperature coupling with strain rate effect is extensive but is primarily concerned with the one-dimensional constitutive model. It is difficult to evaluate the temperature effects comprehensively in the practical experiments, if strain hardening, strain rate hardening, thermal softening and multi-axial stress states are fully considered. Furthermore, coupling of thermal softening effect into hardening and fracture will impose extra challenges for model development and FE analysis. The study on temperature effect on plasticity and fracture AHSS is thereby reserved for the future work.

CHAPTER 5 ZONES OF MATERIAL SEPARATION IN CUTTING SIMULATIONS

5.1 Algebraic and Slip Line Field Analysis

Experiments show that most plastic deformation in plane strain orthogonal cutting of ductile solids is concentrated in a narrow band of shear (the so-called primary shear plane) inclined at an angle ϕ to the cut surface, the simplest representation for which is Piispanen's 'deck of cards' model (Atkins, 2009). In the Ernst-Merchant algebraic analysis of orthogonal cutting of ductile solids, cutting forces are determined from the plastic flow along the primary shear plane of by which the chip is formed, and from secondary plastic flow and friction along the rake face of the tool, see e.g. Shaw and Cookson (2005). Cook, Finnie, and Shaw (1954) showed that for the kinematics of the 'deck of cards' model to operate, a gap XY having the width of the shear plane has to form at the tool tip simultaneously with slip along the shear plane. The reason is because plastic flow occurs under constant volume, and without the gap, ZWV is an inadmissible increase in plastic volume under the plane strain conditions of orthogonal cutting.

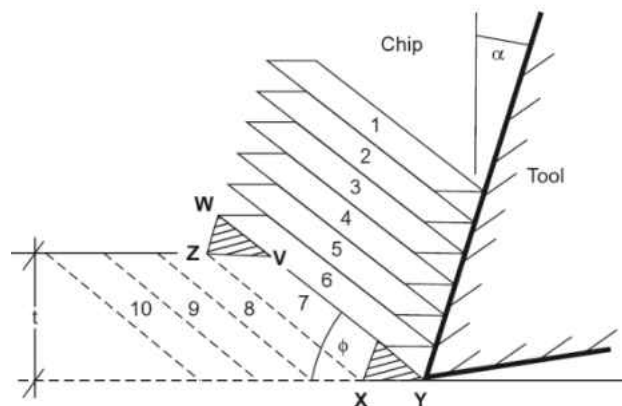


Figure 5-1. Piispanen's 'deck of cards' model. If slip occurs in plane strain in a finite width band along the primary shear plane, plastic volume cannot be conserved unless a gap occurs in the region of XY. Otherwise ZWV is an increase in plastic volume (Atkins, 2009) (adapted from (Cook et al., 1954)).

Shaw and Cookson (2005) understood that the formation of new surface XY required work and that this work ought to be incorporated in analyses of cutting forces. To estimate the magnitude of the work of separation they employed the surface free energy γ of the new surface, which for all materials has an order of magnitude value of a few J/m^2 . They concluded that the incremental work of formation of new surfaces in cutting (i.e. the incremental work of separation of material at the tool tip) was negligible in comparison with the component incremental works of plastic flow and friction during cutting. That became the received wisdom, so that developments of algebraic and slip line field analyses of machining in the second half of the 20th century concentrated on the effects of work-hardening in flow fields more complicated than the simple deck of cards model, strain rates and temperature on primary and secondary plastic flow and friction, to link theory and experiment. Even with such refinements, many observations in machining cannot be explained by traditional analyses (Atkins, 2009).

Atkins (2003) argued that the surface free energy γ was not the correct parameter by which to estimate the work of surface formation in cutting: γ is a short-range parameter concerning the unmatched chemical bonds exposed on free surfaces with the rest of the body unaffected, but surfaces in cutting are not formed that way. Instead, there are highly deformed boundary layers contiguous with all practically cut surfaces, and the associated work of formation per unit area within the boundary layers must be included in the total work of surface formation. The same question had arisen in the development of the subject of fracture mechanics where, because of this additional work of sub-surface deformation, Orowan and Irwin had to use 1000γ in place of γ in the Griffith formula to make sense of experimental results (Knott, 1973). Even in cleavage, where

sub-surface deformation is limited, γ is not used directly to predict forces from fracture mechanics formulae (Cottrell, 1964). The ‘1000 γ ’ property of materials is called the fracture toughness and is given the symbol R in this paper (G_c and J_c are also used). R represents the irreversible work done as the microstructure within the boundary layers is damaged up to failure, leading to separation at the tip of the cutting tool which, in turn, permits the tool to move forward. R may be viewed as some measure of workpiece ductility.

When R (in place of γ) is employed in modelling the mechanics of continuous chip formation, the controlling parameter is not just strength (equivalent to hardness) as in traditional analyses, but rather the toughness-to-strength ratio (R/k), where k is the shear yield strength. It seems reasonable that cutting mechanics should involve a measure of ductility as well as strength, since the cutting behavior of materials having the same R but different k , and vice-versa, can be quite different. It is known that the hardest material is not always the most difficult to cut (Kopalinsky & Oxley, 1987). In fact, cutting is not a problem just of plasticity, but is a branch of elastoplastic fracture mechanics. The formation of continuous or discontinuous chips, with steady or fluctuating cutting forces, simply reflects ‘cube-square’ energy scaling inherent in the mechanics of fracture. The type of chip formed depends upon the depth of cut relative to the length scale given by (R/k). When the non-dimensional number $Z = (R/kt)$ is large, ductile cutting ensues with continuous chips; when Z is small, brittle chipping takes place (Atkins, 2009). At intermediate values, serrated or discontinuous chips are formed.

The new analysis explains why ϕ is different for different materials – it depends on workpiece (R/k) – and why quasi-linear plots of cutting force vs depth of cut (uncut chip thickness)

do not pass through the origin but have a positive intercept on the force ordinate. Such plots are well-known in the literature, but the intercepts are often explained away in terms of so-called ploughing (blunt tools), wear on the flank (clearance) face of the tool, rubbing on the clearance face etc. While all those factors will play a part in increasing tool forces, experiments show that when efforts are made to eliminate all these effects, an intercept remains, the magnitude of which depends on the fracture toughness of the workpiece material. The slopes of the plots are determined by the yield stress of the workpiece (Atkins, 2009).

Favorable comparison of theory and experiment for a wide range of engineering and biological materials is summarized in Atkins (2009). Nevertheless, there is an assumption in Atkins' analysis that the individual component works of plasticity, friction and separation are uncoupled. This implies that the separation work is confined to very thin boundary layers and one aim of the present paper is to investigate the size and extent of these highly damaged zones in comparison with the rest of the plastic flow fields.

5.2 Review of Finite Element Modeling

As soon as plastic flow problems like forging had begun to be successfully simulated by FEM codes, the same programs were applied to the simulation of cutting. But a difficulty arose. It was found that the cutting tool would only travel an appreciable distance when a 'separation criterion' was employed at the tool tip to release nodes, yet no separation criterion was required when the same programs were used for plastic forming operations. It is clear that attempts to model cutting without inclusion of a separation criterion were simulating the different problem of an indentation by an inclined wedge (the tool) into the end of the workpiece, in which the material at

the cutting edge is stretched around the line of the wedge but is not separated. What was being simulated was a type of hardness test. In the FEM simulations reported in subsequent sections of this paper, the ‘indentation’ problem, rather than the ‘cutting’ problem, was replicated when the criterion for separation at the cutting edge was switched off.

In finding that the cutting tool would not move appreciably, FEM modelers had rediscovered what Cook et al. had said in (Cook et al., 1954), and what Astakhov said in (Astakhov, 1998) namely that the difference between cutting and other types of plastic flow problem is that in cutting there is physical separation of the piece being removed. In ordinary plastic flow all material elements retain the same neighbors before and after deformation irrespective of the severity of the deformation. In cutting, elements just above and just below the putative cut line that were neighbors before being separated, are far removed from one another after cutting: those below the cut line remain on the machined surface, those above go away on the underside of the chip. If controlled just by plasticity they would be still attached.

Separation criteria employed in FEM simulations of cutting have taken many forms (Huang & Black, 1996): some were entirely empirical and were more by way of ‘computational fixes’ to overcome the singularity at the tool tip; others represented physical microstructural events that might be taking place at the tool tip to permit separation of nodes, such as the attainment of a critical effective von Mises strain or critical plastic work per volume in elements along the direction of cut. A more recent review article about separation criteria can be found from Vaz, Owen, Kalhori, Lundblad, and Lindgren (2007). The separation criteria can be categorized based on (1) nodal distance (Lo, 2000; Mamalis, Horvath, Branis, & Manolakos, 2001; McClain, Batzer, & Maldonado, 2002; Obikawa & Usui, 1996; Sasahara, Obikawa, & Shirakashi, 1996; Shih, 1995,

1996; Shirakashi & Usui, 1974; Usui & Shirakashi, 1982; Zhang & Bagchi, 1994) (2) strain energy density (Ceretti, Fallböhmer, Wu, & Altan, 1996; Ceretti, Lucchi, & Altan, 1999; Hua & Shivpuri, 2004; Iwata, Osakada, & Terasaka, 1984; Lin & Lo, 2001; Lin & Pan, 1993; Lin & Lin, 1992), (3) critical stress (Hashemi, Tseng, & Chou, 1994; Li, Gao, & Sutherland, 2002; Marusich & Ortiz, 1995; McClain et al., 2002; Shet & Deng, 2003; Shi, Deng, & Shet, 2002), and (4) equivalent plastic strain to fracture (Barge, Hamdi, Rech, & Bergheau, 2005; Benson & Okazawa, 2004; Carroll & Strenkowski, 1988; Hashemi et al., 1994; Mabrouki & Rigal, 2006; Marusich & Ortiz, 1995; Ng, El-Wardany, Dumitrescu, & Elbestawi, 2002; Soo, Aspinwall, & Dewes, 2004; Yang & Liu, 2002). Irrespective of the actual separation criterion employed, no published FEM simulations seem to have evaluated the local work involved in separation of nodes to check whether it was negligible as averred by Shaw and co-workers. Again, the number of elements attaining the separation criterion has not been reported, nor their distribution ‘above’ and ‘below’ the cut surface to see how confined the damaged region is. What is significant, however, is that when a number of different separation criteria were applied to the same problem, the plastic flow fields for chip formation were very similar and almost independent of the detail of the different criteria.

In early 2D finite element analysis of machining using Lagrangian formulations, node-splitting method by a pre-defined parting line (Lei, Shin, & Incropera, 1999; Li et al., 2002; McClain et al., 2002; Obikawa & Usui, 1996; Shi et al., 2002; Shih, 1995; Shih & Yang, 1993) was extensively applied to model chip separation. Initially bonded nodes along the parting line are assumed to debond when either geometrical or physical indicator reaches a critical threshold value. It is argued in (Movahhedy, Gadala, & Altintas, 2000) that the parting line method creates an open

crack ahead of the tool tip, leaving an unrealistic material gap which is not observed in experimental studies of ductile materials. Similar to the concept of pre-defined parting line, several recent studies (Asad, Girardin, Mabrouki, & Rigal, 2008; Mabrouki, Girardin, Asad, & Rigal, 2008; Mabrouki & Rigal, 2006; Zhang, Mabrouki, Nelias, & Gong, 2011) attempt to use pre-defined sacrificial element layer along the tool tip travel path. By doing this, presumed fracture energy values were implemented as input data in the pre-defined sacrificial element layer and the chip. Despite that this approach gives more realistic results and physical insight into the fracture mechanism than previous studies of ductile materials, further investigations are necessary to incorporate robust plasticity and ductile fracture models which enable to capture the intrinsic features during deformation under multiaxial stress states and their associated fracture mechanisms. The chip separation and breakage, along with chip flow characteristics should be determined simultaneously without being restricted to a certain presumed fracture mode as in the assumption of pre-defined parting line or sacrificial layer method. Recent development on coupled/uncoupled ductile fracture model in orthogonal cutting modelling can be found from (Childs, 2013; Ducobu, Rivière-Lorphèvre, & Filippi, 2014; Ducobu, Rivière-Lorphèvre, & Filippi, 2015; Liu, Bai, & Xu, 2014).

Nevertheless, the necessity of having to employ a separation criterion in FEM simulations of cutting is an anathema to many workers, particularly if the criteria are linked to microstructural fracture events at the cutting edge as argued by Atkins (2003). There remains a strong belief, particularly among those in the field of metal cutting, that fracture parameters can play no role in the mechanics of cutting since ‘cracks are not seen at the tool tip in continuous-chip steady-state cutting of ductile metals’. This belief fails to distinguish between crack *existence* (where the crack

velocity coincides with the tool velocity when cutting ductile materials) and crack *stability* (where the crack velocity is faster than the tool velocity). Tool tip cracks *are* visible when cutting less-ductile materials that have smaller (R/k) as shown, for example in (Fleck, Kang, & Williams, 1996).

A great deal of effort has been spent trying to find ways of simulating cutting without using a separation criterion in FEM (i.e. (Dirikolu, Childs, & Maekawa, 2001)). The lack of consensus on an appropriate separation criterion was encountered in Lagrangian formulation. The Eulerian (Carroll & Strenkowski, 1988; Dirikolu et al., 2001; Iwata et al., 1984; Joshi, Dixit, & Jain, 1994; K. W. Kim, W. Y. Lee, & H.-c. Sin, 1999; K. W. Kim, W. Y. Lee, & H. C. Sin, 1999; Racz, Elmadagli, Altenhof, & Alpas, 2004; Strenkowski & Athavale, 1997; Tyan & Yang, 1992; Wu, Dillon Jr, & Lu, 1996) and arbitrary Lagrangian Eulerian (ALE) formulations (Benson & Okazawa, 2004; Movahhedy et al., 2000; Olovsson, Nilsson, & Simonsson, 1999; Pantalé, Bacaria, Dalverny, Rakotomalala, & Caperaa, 2004; Rakotomalala, Joyot, & Touratier, 1993) came to be alternative solutions to handle the numerical problems of large element distortion. However, what has *not* been done in the fluid-flow-type programs and continuous re-meshing modelling is to investigate whether somewhere in the flow field a criterion for fracture has been satisfied. The chip formation is a result of plastic flow of materials around the tool. The absence of fracture criterion benefit from a numerical point of view but its physical validity could be questioned. It is rather like solving an elasticity problem out to large strains without enquiring whether somewhere a yield criterion has been satisfied. Again, re-meshing simulations ought not to attain a steady state cutting force since the flow strains keep on increasing with tool travel. The only reason steady-state cutting forces are obtained is because the stress-strain constitutive relations employed saturate out at large strains to a constant value.

We shall show in this paper that re-meshing simulations do not represent the physics of what happens at the cutting edge even though they may predict sensible flow fields. We show that

- (i) FEM simulations using the JC damage relation as a criterion for separation at the tool tip, predict the sorts of quasi-linear relation between cutting force and depth of cut found experimentally for all ductile materials.
- (ii) At small depths of cut, the FEM predictions for cutting force depart from linearity and “curve down towards the origin”, but still do not pass through the origin and have a positive intercept as the depth of cut tends to zero.
- (iii) Those material elements that fracture according to the JC criterion are confined to thin layers of material between the underside of the chip and surface of the cut body.
- (iv) The JC damage criterion, expressed as a plastic work/volume (given by the area under the effective stress-effective strain curve out to the JC failure strain), together with the size of the damaged region, is related to the fracture toughness as determined from the force intercept.

5.3 Finite Element Model Setup

A thermo-mechanical 2D plane strain model was established in commercial finite element software Abaqus/Explicit v6.11. Figure 5-2 illustrates the configuration and boundary conditions in the model. Since the supposed value of feed rate (depth of cut) is much smaller than the designated radial cutting depth, it is reasonable to assume plane strain condition for the simulations in this study. The cutting tool was defined as a 2D analytical rigid body. The tool tip is sharp as assumed in the single shear plane algebraic model in Section 5.6. The workpiece in the experiments

was simplified as a single-part 2D rectangle with planar dimension of 12 mm × 1.2 mm. The mesh size of the workpiece is 20 μm with plane strain thickness specified at 4 mm. Quadrilateral coupled temperature-displacement continuum element CPE4RT was assigned as the element type in the workpiece during the dynamic analysis. For simplicity, a surface-to-surface contact pair was defined for the tool-workpiece interaction using finite sliding formulation during the analysis step. The friction coefficient μ and shear stress limit τ_{crit} was set to be 0.17 and 161 MPa respectively, the same as other experimental and numerical study of 2024-T351 aluminum alloy (Li et al., 2002; Liu et al., 2014; Mabrouki et al., 2008). 90% of dissipated energy caused by friction was assumed for heat conversion. As an initial condition, the temperature field was predefined uniformly throughout the workpiece at constant 25 °C.

In order to obtain a comprehensive group of simulation data for this study, 60 finite element simulations in total were carried out at 6 different rake angles (-20°, 0°, 10°, 20°, 30°, 40°) and 10 different depths of cut t_0 from 50 μm to 500 μm with a progression of 50 μm between t_0 values.

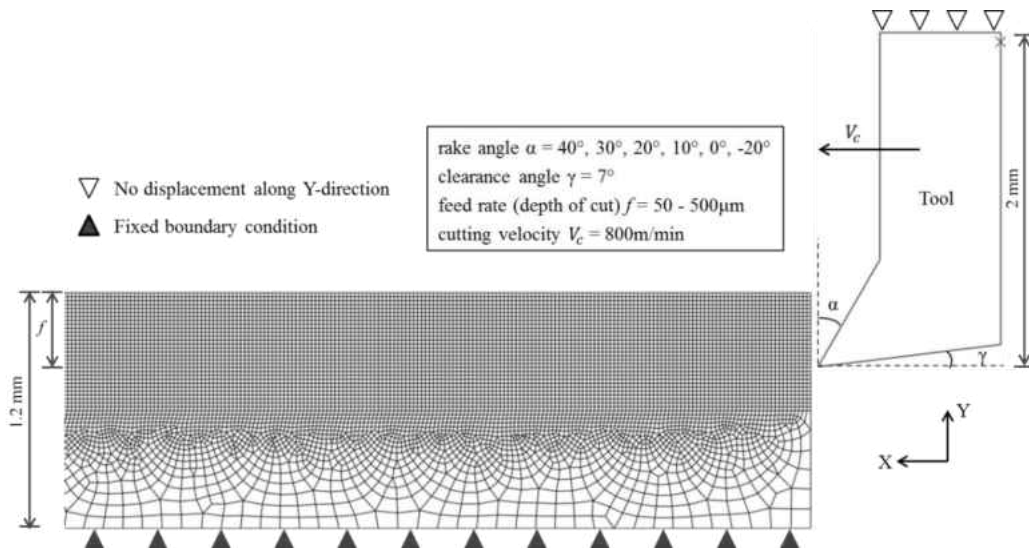


Figure 5-2. Configuration and boundary condition of the FEM model for orthogonal cutting simulations in this study

5.4 Johnson-Cook Plasticity and Damage Model

In this study, the Johnson-Cook (JC) plasticity and damage models (Johnson & Cook, 1983) are adopted as the material model for the purpose of investigating both chip flow and the formation of separation zones.

The JC plasticity model is often used in forming and crashworthiness simulations because it provides good descriptions of most metals undertaking large deformation at a wide range of strain rates and temperatures, and it is particularly suitable for high-strain rate deformation in adiabatic transient dynamic simulations. The equivalent stress in JC plasticity model uncouples the effect of strain hardening, temperature softening, and strain rate dependence, and it is given by

$$\bar{\sigma} = (A + B\bar{\epsilon}_{pl}^n) \left[1 + C \ln \left(\frac{\dot{\epsilon}}{\dot{\epsilon}_0} \right) \right] \left[1 - \left(\frac{T - T_{room}}{T_{melt} - T_{room}} \right)^m \right] \quad (5-1)$$

Here, A , B and n are material constants for strain hardening; C is the material constant for strain-rate hardening; m is the material constant for thermal softening; T represents the current temperature, whereas T_{melt} and T_{room} stand for the melting and reference ambient temperature, respectively.

Table 5-1. Johnson-Cook plasticity parameter values for AA2024-T351

A	B	N	C	m
352	440	0.42	0.0083	1

The JC plasticity parameters for AA2024-T351 are listed in Table 5-1 and the physical parameters of the workpiece are summarized in Table 5-2. The parameters in both tables are the same as Mabrouki et al. (2008).

Table 5-2. Physical properties of the workpiece material AA2024-T351

Physical parameter	Workpiece (A2024-T351)
Density, ρ (kg/m^3)	2700
Elastic modulus, E (GPa)	73
Poisson's ratio, ν	0.33
Specific heat, C_p (J/(kg°C))	$C_p = 0.557T + 877.6$
Thermal conductivity, λ (W/(m°C))	$\lambda = 0.247T + 114.4 \quad (25 \leq T \leq 300)$
	$\lambda = -0.125T + 226.0 \quad (300 \leq T \leq T_{melt})$
Thermal expansion, α_d ($\mu m/m/^\circ C$)	$\alpha_d = 8.9 \times 10^{-3}T + 22.2$
T_{melt} ($^\circ C$)	520
T_{room} ($^\circ C$)	25

The JC fracture criterion is a phenomenological model for predicting damage initiation due to nucleation, growth, and coalescence of voids. The equivalent plastic strain at fracture initiation is assumed to be of the form in Eq.(5-2). The effects of strain rate and temperature are incorporated in a similar manner as in the JC plasticity model.

$$\bar{\epsilon}_f^{pl} = (d_1 + d_2 e^{d_3 \eta}) \left[1 + d_4 \ln \left(\frac{\dot{\epsilon}}{\dot{\epsilon}_0} \right) \right] \left[1 + d_5 \left(\frac{T - T_{room}}{T_{melt} - T_{room}} \right) \right] \quad (5-2)$$

where η is the stress triaxiality, i.e. the ratio of mean stress to Mises equivalent stress; $d_{1\sim5}$ are empirical damage parameters. Recent researches have shown that ductile fracture is dependent on both stress triaxiality and Lode angle (Bai & Wierzbicki, 2008, 2010, 2015). However, the cutting simulation is assumed to be in plane strain, where the Lode angle parameter is fixed ($\bar{\theta} = 0$). Hence the use of the JC fracture criterion for the present study is in order.

Table 5-3. Material parameters in Johnson-Cook damage model

Damage Parameter	d_1	d_2	d_3	d_4	d_5
Present study	0.5	0.13	-1.5	0	0
Mabrouki et al. (2008)	0.13	0.13	-1.5	0.011	0
Liu et al. (2014)	0.13	0.13	-1.5	0.011	0

Table 5-3 lists two sets of the empirical damage parameters: the first row gives those used in the present study; the second row are those used in Liu et al. (2014) and Mabrouki et al. (2008). It should be noted that the damage parameter d_1 in the present paper is much higher than 0.13 in Liu et al. (2014) and Mabrouki et al. (2008), but d_5 is the same. The reason for using larger d_1 but the same d_5 is as follows. First, the present authors realize that only the first term in Eq. (2) was present in the original reference paper (Wierzbicki, Bao, Lee, & Bai, 2005), in which the damage parameters d_1 , d_2 and d_3 were found from Johnson and Holmquist's curve fitting with experimental data (Wierzbicki et al., 2005). However, it appears from Fig.14 in (Wierzbicki et al., 2005) that Johnson and Holmquist only provided a lower bound for the Johnson-Cook fracture locus for this material. Secondly, $d_5 = 0$ in Liu et al. (2014) and Mabrouki et al. (2008) because the experiments in Wierzbicki et al. (2005) were carried out at constant strain rate under room temperature. During the high-speed machining process, temperature in the cutting zone can rise significantly, resulting in a remarkable increase in ductility and fracture strain. Experimental studies on AA2024-T351 (Johnson & Cook, 1983; Leseur, 1999) show that the ductility enhances notably with increasing temperature. Given the fact that it is difficult to obtain d_4 and d_5 unless a tremendous number of tests under different loading conditions at high temperatures are performed, we average out the effects of strain rate and temperature (i.e. neglecting the last two terms in Eq.

(2)) by adding them into d_1 . In other words, even though the current damage parameters lack the support of experimental data, it simplifies the comprehensive uncoupled JC fracture model with reasonable approximation. Thirdly, our simulation will be compared with analytical solutions of cutting forces, where the effects of temperature and strain rate are neglected or averaged out. This simplification makes the comparative study easier.

In this study, the JC constitutive model was implemented by a user material subroutine VUMAT in Abaqus/Explicit. Elements are assumed to fail and are deleted when the damage indicator D exceeds unity.

$$D = \sum \frac{\Delta \bar{\epsilon}^{pl}}{\bar{\epsilon}_f^{pl}} \quad (5-3)$$

where $\Delta \bar{\epsilon}^{pl}$ is the incremental equivalent plastic strain updated during the analysis, and $\bar{\epsilon}_f^{pl}$ is the equivalent plastic strain at fracture for a particular loading condition (or ‘fracture locus’). The subroutine enables the FE program to update plastic strain energy density after each increment. The plastic work/volume and the size of the damaged region is believed to have an intrinsic relation with the specific work of new surface formation (fracture toughness). The flow chart in Figure 5-3 shows how the damage indicator and plastic strain energy density are updated in the codes.

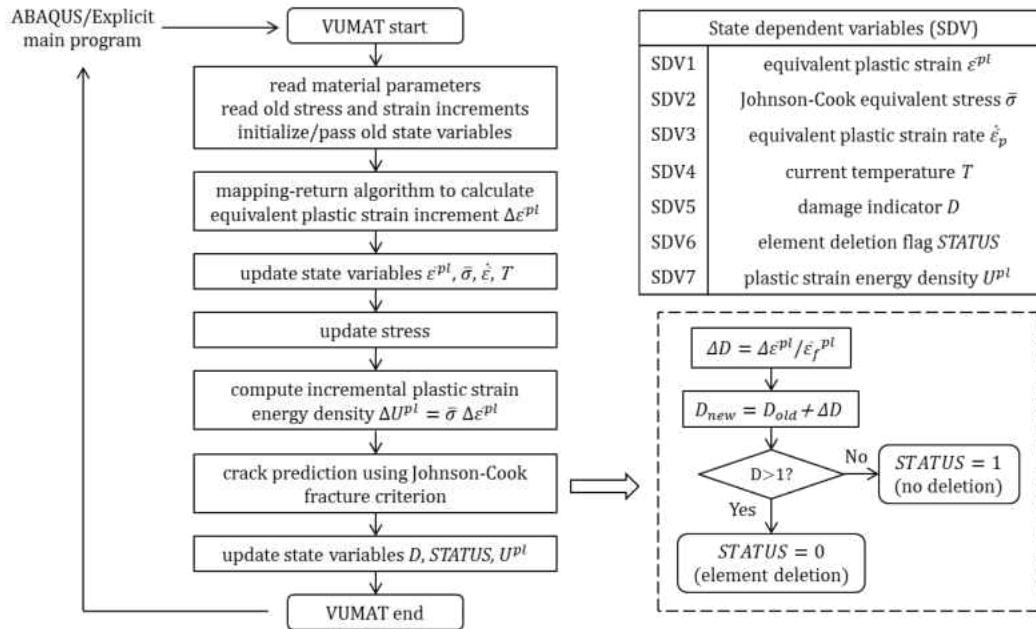


Figure 5-3. Flow chart of the user material subroutine VUMAT in Abaqus/Explicit

A final remark in this section relates to the stress triaxiality “cut-off” value implemented to the JC fracture locus. According to the analytical study by Bao and Wierzbicki (2005), ductile materials would never fail if the stress triaxiality is less than -1/3. Actually, a “cut-off” region exists for a general loading condition Bai and Wierzbicki (2010, 2015) if the Lode angle effect is considered. Since the current simulations are under plane strain condition, a “cut-off” value is used. Neglecting the “cut-off” value could lead to unreasonable results for chip formation and cutting forces.

5.5 Finite element simulation results

5.5.1 Forces

Figure 5-4 shows plots of the cutting force vs. tool travel distance for all depths of cut and rake angles investigated in this study. The data in the plot were extracted from predefined history outputs (horizontal reaction force and displacement) of the rigid tool in the simulations. The curves are terminated after 500 μs when representative chip formation and force curve were found. Two types of force curves can be observed from Figure 5-4 depending upon depth of cut t_0 and rake angle α : (1) smooth quasi-steady load at small t_0 and large α ; and (2) fluctuating load at large t_0 , with small or negative α . The corresponding chip morphologies are shown in Figure 5-5. Smooth cutting forces correspond to ribbon-like continuous chip formation, while fragmented discontinuous chips are accompanied by fluctuating loads, the amplitudes of which increase with depth of cut. During the formation of continuous chips, the JC fracture relation predicts separation by crack propagation along the same direction as the tool tip travels, at approximately the same speed as the tool velocity. The chip curls up and bends over at nearly constant radii so that the force required for pushing up the chip does not change much throughout the entire cutting process. When the rake angle decreases, more compression and shear deformation are induced. Shear type discontinuous chips become dominant in small and negative rake angles. The reasons for large load fluctuation are as follows. After the load increases to the first peak under elastoplastic loading, it drops rapidly because the crack runs ahead of the tool in the direction of cut and also along the primary shear zone towards the free surface of the workpiece. The chip is not completely detached before the tool tip again touches the uncut workpiece. Continued tool travel compacts the uncut

material, the load increases and the process start over again. It is found that the frequency of load peaks (or valleys) determines the number of discontinuous chips separated out of the workpiece, while the magnitude of the load wave decides their sizes.

5.5.2 Deformation Fields of Stress, Strain and Temperature

Figure 5-5 shows the FE simulation results of von Mises stress distribution at selected depths of cut for each rake angle. The figures are displayed at different cutting time instants in favor of a better presentation of the major features in the deformation field. The primary shear zones are clearly demonstrated: under a large amount of plastic deformation, stress is highly concentrated within a narrow region radiating from the tool tip towards the free surface at the chip root. On the other hand, the contour plots of the cut chips in green and blue indicate much lower stress values due to thermal softening effect and unloading after material separation. In all cases, deformation is negligible in the areas far from the tool-workpiece interaction zone.

The present simulation results in Figure 5-5 also captured the main characteristics of the chip morphology that have been discussed extensively in metal cutting books (Astakhov, 1998; Shaw & Cookson, 2005; Stephenson & Agapiou, 2016; Trent & Wright, 2000). For the condition of high cutting speed in this study, continuous chips were produced at large rake angles and small depths of cut (e.g. in Figure 5-5 (1a-3a) and (1b-3b)). In these cases, chips were separated from the workpiece along the constant depth of cut paths of the tool cutting edge. Discontinuous chips were generated when shear cracks propagate in the primary shear zone, particularly noticeable for the cases of negative rake angle (Figure 5-5 (6a-6c)). A few serrated chips (e.g. in Figure 5-5 (3c))

and (4b)) were formed when segmentations on continuous chips were initiated by the growing bending state and promoted by its interaction with the tool advancement.

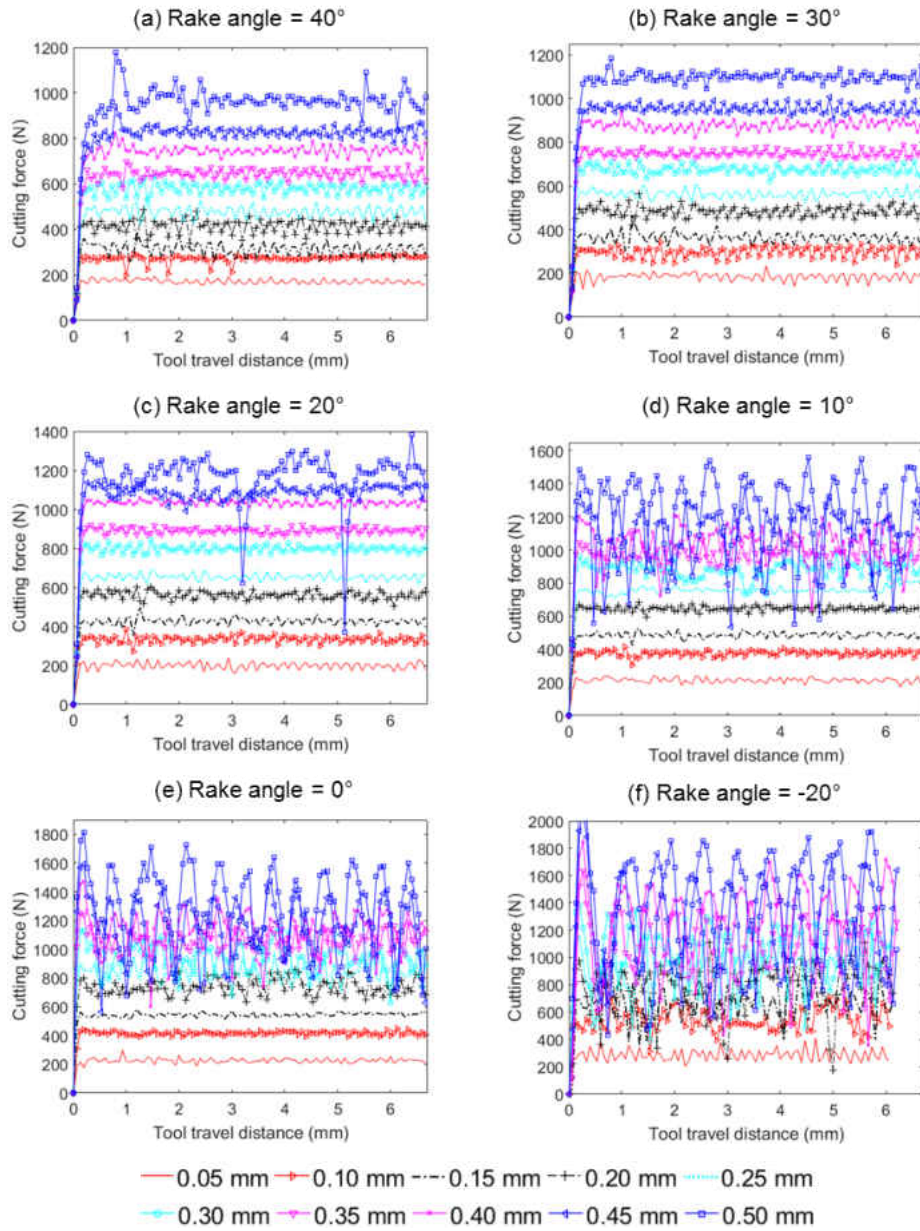


Figure 5-4. cutting force vs. tool travel distance at different depths of cut and rake angles

The equivalent plastic strain field is shown in Figure 5-6. SDV1 represents the equivalent plastic strain $\bar{\epsilon}_{pl}$ in the user-defined material subroutine in ABAQUS. For the convenience of a

consistent representation of simulation results, the value range of SDV1 in the legend box of the contour plot was specified from 0 (blue) to 1 (red) for all cases. The areas in grey color indicate that the field output value exceeds the maximum limit, i.e. $\bar{\epsilon}_{pl} > 1$. The equivalent plastic strain in the grey area was accumulated under massive compression at the initial moment when the tool tip touches the workpiece. After the chip curls-up, the underside of the chip is subjected to tension due to bending. This phenomenon is particularly evident for continuous chips (e.g. Figure 5-6 (1a-5a)): the smaller the rake angles, the more compression induced towards the free surface of the chips. For serrated or discontinuous chips (e.g. Figure 5-6 (4b) and (6b)), severe plastic deformation was accumulated in a highly localized shear band. The elements within the shear band at this moment were initially deformed under compression, followed by shear dominated deformation, and then split with the chip or workpiece after the fracture criterion was satisfied.

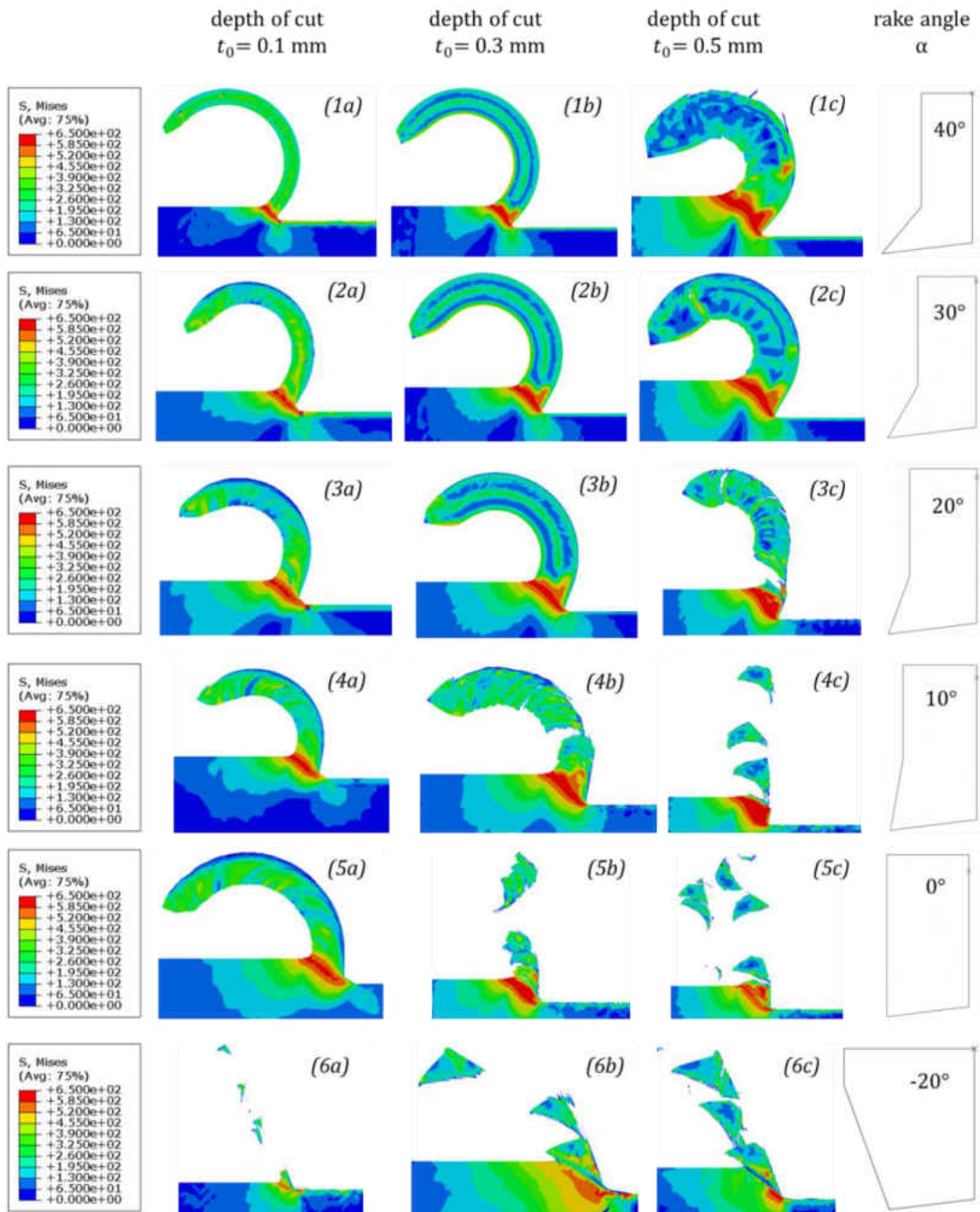


Figure 5-5. von Mises stress distribution of chip formations at different rake angles and selected depths of cut

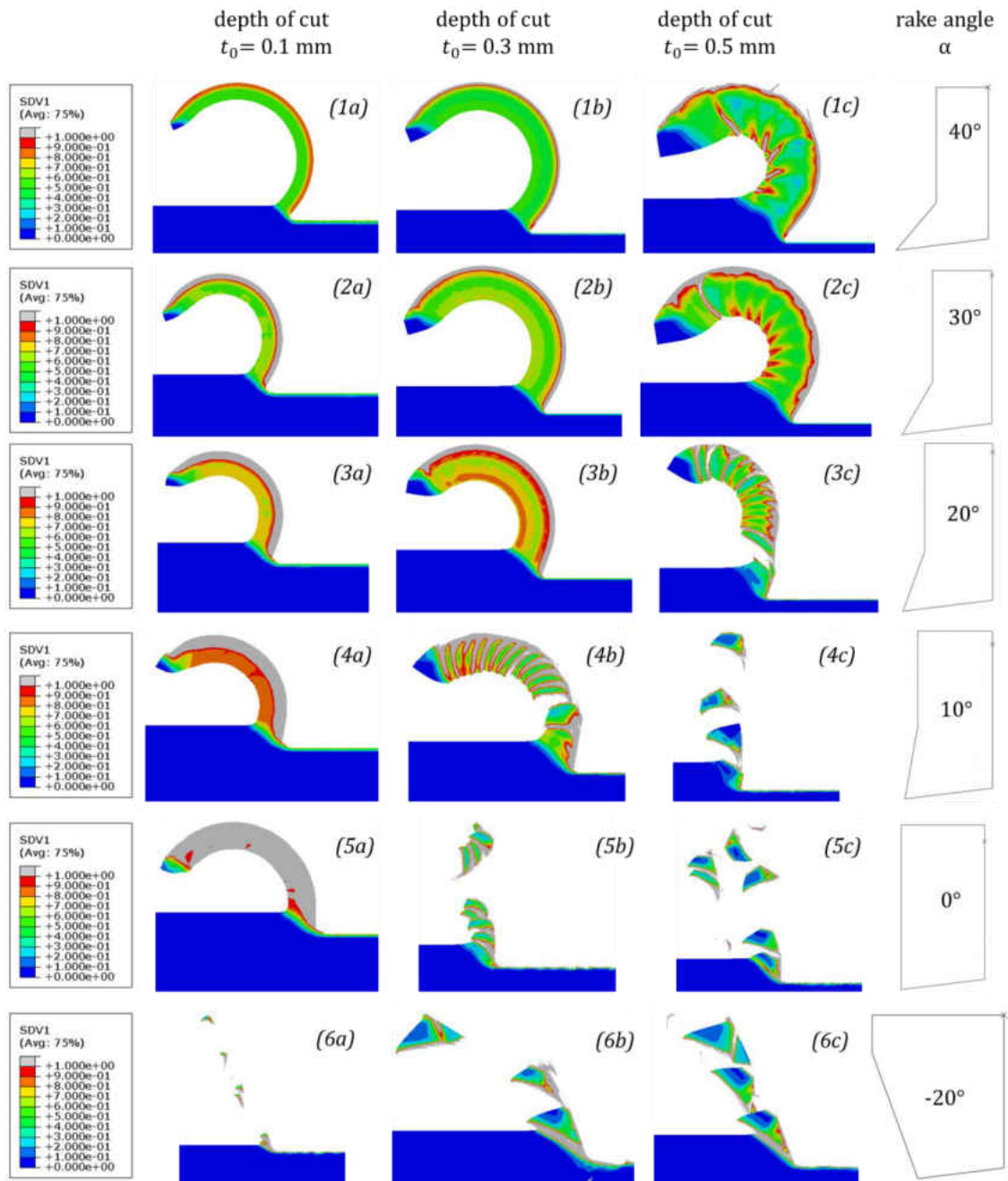


Figure 5-6. Equivalent plastic strain distribution of chip formations at different rake angles and selected depths of cut. Blue means 0 and red means 1.0

Figure 5-7 shows the temperature distribution (SDV4) in three representative chip types. In the subroutine, 90% of plastic energy was assumed to dissipate into heat generation in form of temperature rise. As the tool tip moves forward, the temperature increases from the root of the chip and evolves towards the chip-free side. As a result of large plastic deformation and friction, the temperature on the underside of the chip is higher than in the other areas in Figure 5-7(a) and (b). In Figure 5-7(c), significant temperature rise is concentrated within the primary shear zone. The equivalent stresses are consequently lower in the vicinity of these highly deformed areas due to thermal softening.

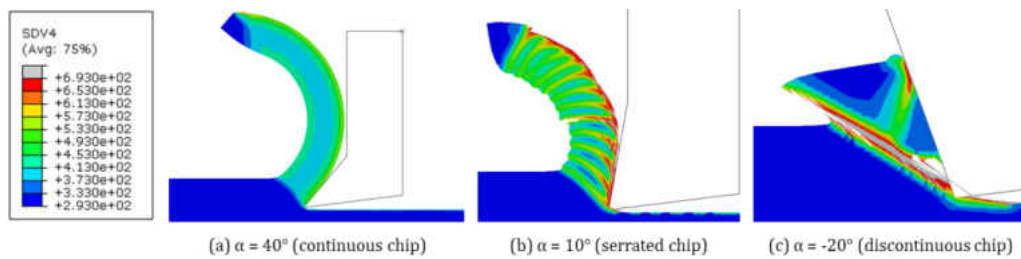


Figure 5-7. Temperature distribution in three representative chip types (unit: K)

5.5.3 Separation Zones

In the cutting simulations, separation zones refer to groups or layers of elements removed after the fracture criterion is satisfied. As mentioned in Section 5.4, in the user-defined material subroutine, elements are deleted when the damage indicator exceeds unity ($D > 1$). Figure 5-8 shows the distribution of the damage indicator D on the chip and the cut workpiece. Since D is defined on a strain basis, damage distribution on the chip and workpiece is analogous to the contour plot of equivalent plastic strain. However, it is worth mentioning that in the visualization module of Abaqus, the separation zone can be only visible in the contour plot on undeformed shape. Figure 5-9 exhibits some examples of damage distribution for different chip types in the contour plots of

undeformed shapes. The elements in red indicate their damage value is greater than unity so that they are deleted and invisible in the contour plots on deformed shapes.

In the contour plot of damage distribution on the undeformed shape Figure 5-9(a), the elements along the horizontal tool tip travel path were severely damaged and eventually deleted in the contour plot on deformed shape. This group of elements are defined as type(i) separation zone in this paper. In Figure 5-9(b)(c), the highly damaged shear bands during the formation of serrated and discontinuous chips, are referred as type(ii) separation zone. It is important to note that type(i) and type(ii) separation zones coexist for the cases of serrated and discontinuous chips. The focus of this paper is to discuss the damaged boundary layer associated with type(i) separation zone for the case of continuous chips. The formation of type(ii) separation zone by possible shear fracture along the primary shear plane, is an entirely different problem beyond the scope of this study.

The damage accumulation process can be illustrated by an arbitrary element on the underside of the continuous chip. Figure 5-10 shows how the equivalent plastic strain $\bar{\epsilon}^{pl}$ and damage indicator D evolves with loading history in this element. When the tool tip travels close to the element, plastic deformation starts accumulating at triaxiality η close to 0.5. The element is then subjected to compression with the tool advancement during which $\bar{\epsilon}^{pl}$ increases from 0.32 to 1.72. However, the increase in D is not that significant (from 0.22 to 0.45) within the compression regime. After the chip curls up and bends over, the loading condition in the element switches from compression to tension. According to Eq. (5-3), damage is accumulated at a rate of $1/\epsilon_f$, where ϵ_f is the fracture strain on the JC fracture locus for $\eta \geq -1/3$. Note that during this period, even though its $\bar{\epsilon}^{pl}$ value is much larger than the corresponding ϵ_f on JC fracture locus, the element is

however not deleted. This reveals an important point that damage accumulation depends upon the loading history, rather than an instant loading condition or instant equivalent plastic strain.

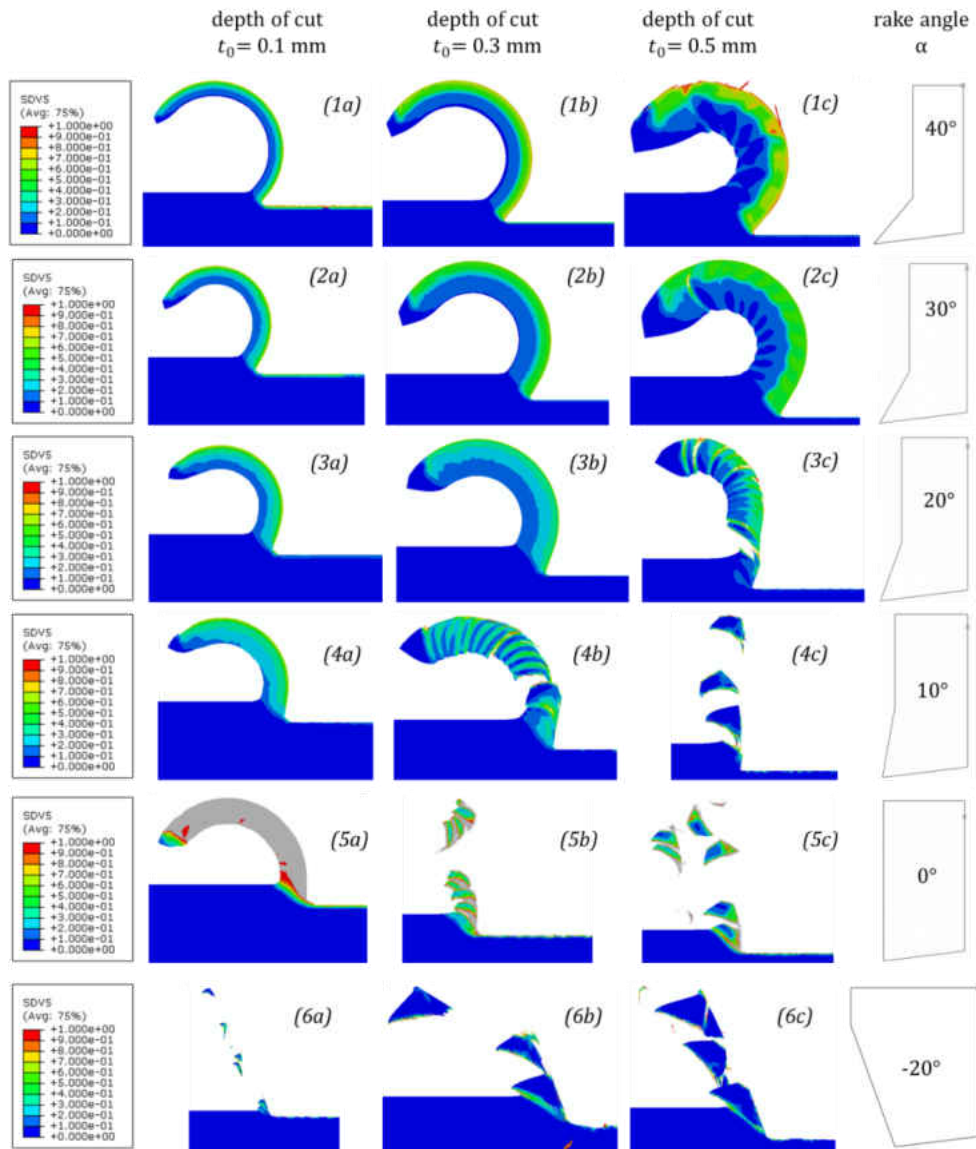


Figure 5-8. Damage distribution on the contour plot of deformed shape at different rake angles and selected depths of cut. Blue means 0 and red means 1.0.

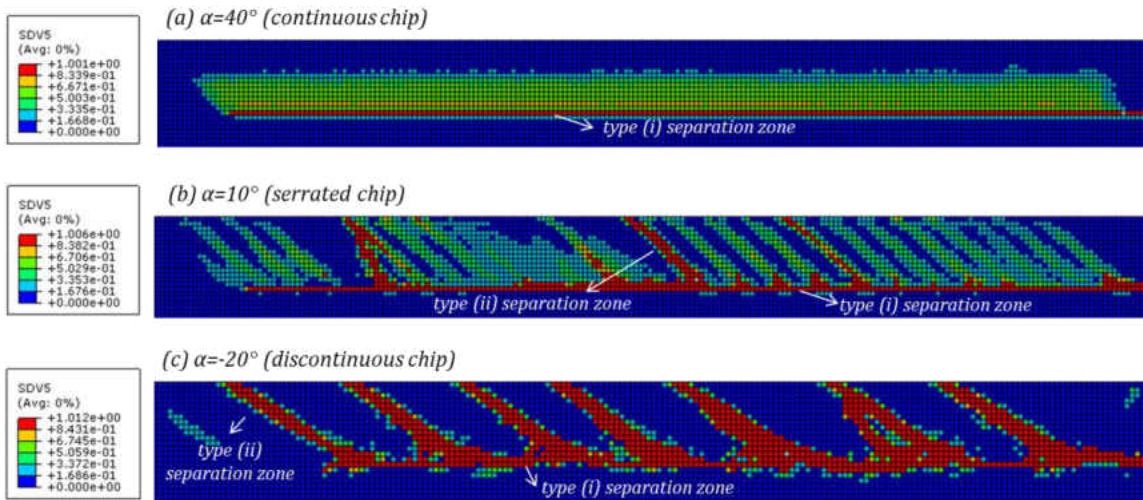


Figure 5-9. Damage distribution on the contour plot of undeformed shape ($t_0 = 0.3$ mm)

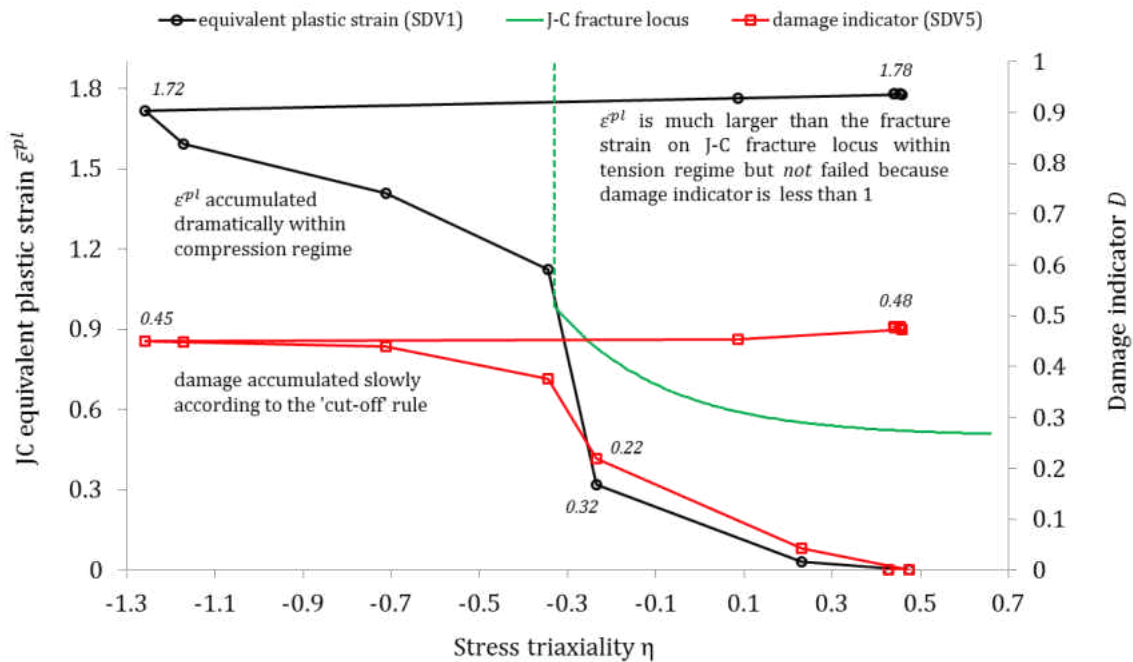


Figure 5-10. Evolutions of plastic strain, stress triaxiality and damage indicator for an element on the underside of the chip ($\alpha = 40^\circ$, $t_0 = 0.25$ mm)

5.5.4 Conversion of Incremental Tool tip Work into Fracture Toughness

For continuous chip formation, there exists an intrinsic relation between the incremental tool tip work/area (fracture toughness) and plastic work/volume in the highly-deformed region associated with type (i) separation zones (Atkins, 2003). The following proposes the methodology of calculating incremental plastic work/area done in the boundary layer from FEM simulation outputs in this study.

A representation of the highly deformed boundary layer is illustrated in a simulation contour plot in Figure 5-11. Figure 5-11(a) and (b) indicate the evolution of boundary layer between two cutting instants, during which new surface pairs were formed parallel to the tool travel path along the horizontal direction. The incremental volume of the boundary layer along the tool tip travel path is $dV = (dL)hw$, where dL is the incremental distance the tool tip travels, h is the height of the boundary layer, and w is the plane strain thickness specified in the simulation. Assume there are N elements in the boundary layer, then the volume per element $V_e = (dL)hw/N$. The incremental area of the new surface is $dA = (dL)w$. The incremental plastic strain energy density in each element is denoted as $(dU_{pl})_i$, $i=1\sim N$. Therefore, the total plastic strain energy in the boundary layer is

$$d\Gamma = (dU_{pl})_1V_e + (dU_{pl})_2V_e + \dots + (dU_{pl})_NV_e = (dU_{pl})_{total}V_e \quad (5-4)$$

where $(dU_{pl})_{total}$ is the sum of incremental plastic strain energy density of all N elements in the boundary layer. The specific work of new surface formation becomes

$$R = \frac{d\Gamma}{dA} = \frac{(dU_{pl})_{total}V_e}{(dL)w} = \frac{(dU_{pl})_{total}h}{N} = (dU_{pl})_{avg}h \quad (5-5)$$

where $(dU_{pl})_{avg}$ is the averaged incremental plastic strain energy density of the N elements in the boundary layer. The FEM simulation output results of $(dU_{pl})_{avg}$ are shown in Figure 5-12. Atkins (2003) employed a similar method to estimate the magnitude of surface work by converting the critical work/volume into critical work/area in the highly distorted boundary layer from other FEM simulation reports. The critical work/volume in Atkins (2003) was simply calculated by multiplying the work-hardened yield strength with the critical fracture strain. The averaged incremental plastic strain energy density $(dU_{pl})_{avg}$ for a JC hardening model in this study, is essentially equivalent to the critical work/volume in Atkins (2003). The equivalence of yield stresses between work hardening material in the present simulations and rigid-plastic material in the algebraic model is further discussed in Section 5.6.

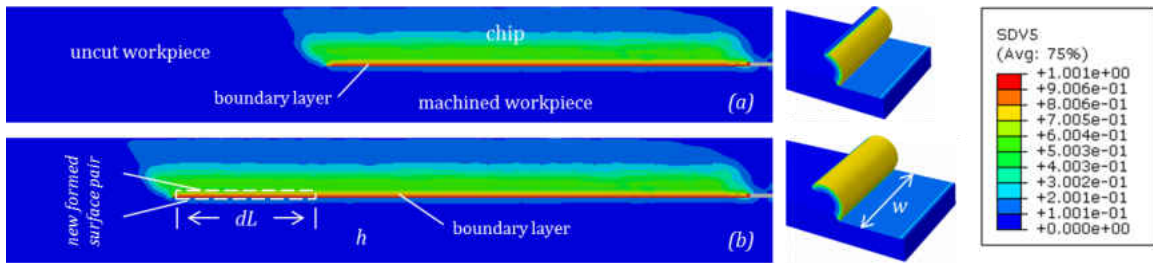


Figure 5-11. A representation of highly-deformed boundary layer on the contour plot of damage distribution at cutting instant of (a)150 μ s (b)200 μ s. Figures on the right shows an extruded 3D representation of the model.

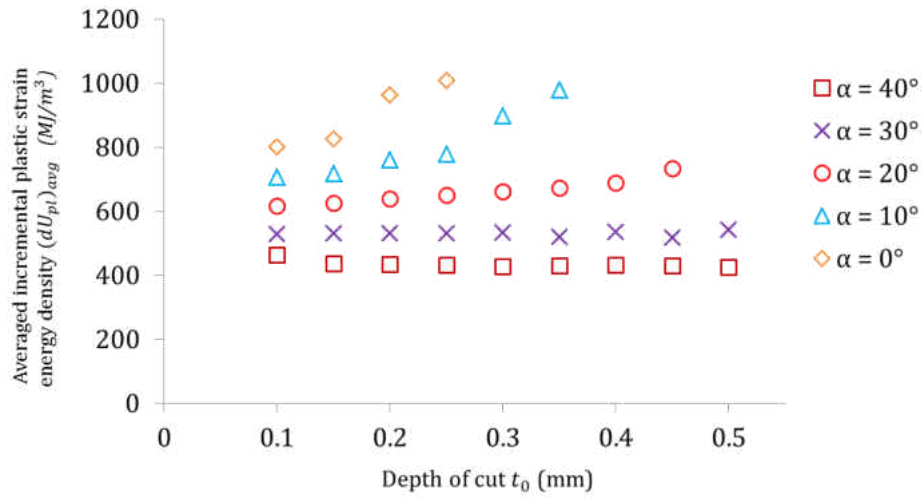


Figure 5-12. FEM simulation result of averaged incremental plastic strain energy density $(dU_{pl})_{avg}$ at each depth of cut and rake angle in cases of continuous chip formation

The procedures for calculating incremental tool tip work done from simulation outputs and converting it to specific work of new surface formation (fracture toughness) are described as follows:

- (1) In the visualization module, setup the plot contours on *undeformed* shape.
- (2) Select a region during steady state cutting regime and pick up corresponding elements in the boundary layer as shown in Figure 5-11.
- (3) Average the plastic strain energy density $(dU_{pl})_i$, $i=1\sim N$ of the elements in the boundary layer.
- (4) Apply Eq.(5-5) to calculate the fracture toughness R (Section 5.6).

5.6 Comparison with Algebraic Models

Atkins' single shear plane model (Atkins, 2003) states that during steady-state orthogonal cutting of ductile solids, the external work is balanced by internal work of plasticity, friction and new surface formation, as given by

$$F_c V = (\tau_y \gamma)(t_0 w V) + [F_c \sec(\beta - \alpha) \sin \beta] \frac{V \sin \phi}{\cos(\phi - \alpha)} + R w V \quad (5-6)$$

Here, V is the cutting velocity, w is the width of the workpiece, t_0 is the uncut chip thickness, τ_y is the rigid-plastic shear yield stress of the ductile material, γ is the shear strain along the primary shear plane, given by $\gamma = \cot \phi + \tan(\phi - \alpha) = \cos \alpha / \cos(\phi - \alpha) \sin \phi$, ϕ is the angle of the primary shear plane, β is the friction angle given by $\tan \beta = \mu$, where μ is the coefficient of friction, α is the rake angle, and R is the specific work of surface formation.

Eq.(5-6) can be simplified into

$$F_c = \left(\frac{\tau_y w \gamma}{Q} \right) t_0 + \frac{R w}{Q} \quad (5-7)$$

where Q is the friction correction parameter given by

$$Q = 1 - \frac{\sin \beta \sin \phi}{\cos(\beta - \alpha) \cos(\phi - \alpha)} \quad (5-8)$$

It is found experimentally that at sufficiently large t_0 , both γ and Q are constant. ‘Sufficiently large’ means a non-dimensional material-dependent parameter $Z = R/\tau_y t_0 < 0.1$ (Atkins, 2003). Under these conditions, F_c vs t_0 plots are predicted to be linear with slope given by $(\tau_y w \gamma / Q)$ and positive force intercept of $(R w / Q)$. At small t_0 , the plot droops downwards below the straight line for γ and Q being constant, but still intersects the force ordinate at a value close to $(R w)$. From the definitions of γ and Q , one can see that for given α and β , γ and Q are totally determined by the shear angle ϕ . If no separate experimental measurements are available for ϕ , it can be predicted analytically by the argument of minimum work (minimum force over the

same displacement), Williams, Patel, and Blackman (2010) derived a closed-form solution for ϕ as follows:

$$\cot \phi = \tan(\beta - \alpha) + \sqrt{1 + \tan^2(\beta - \alpha) + Z [\tan \alpha + \tan(\beta - \alpha)]} \quad (5-9)$$

It follows from Eq.(5-9) that ϕ not only depends on the toughness/strength ratio of the material, but also on the depth of cut. Once ϕ is known, the procedures in (Atkins, 2003, 2005) are followed to establish R and τ_y from the F_c vs. t_0 plot. The flow chart (Figure 5-13) concisely illustrates the iterative process of finding ϕ and simultaneously determining R and τ_y based on the detailed procedures described in (Atkins, 2003, 2005).

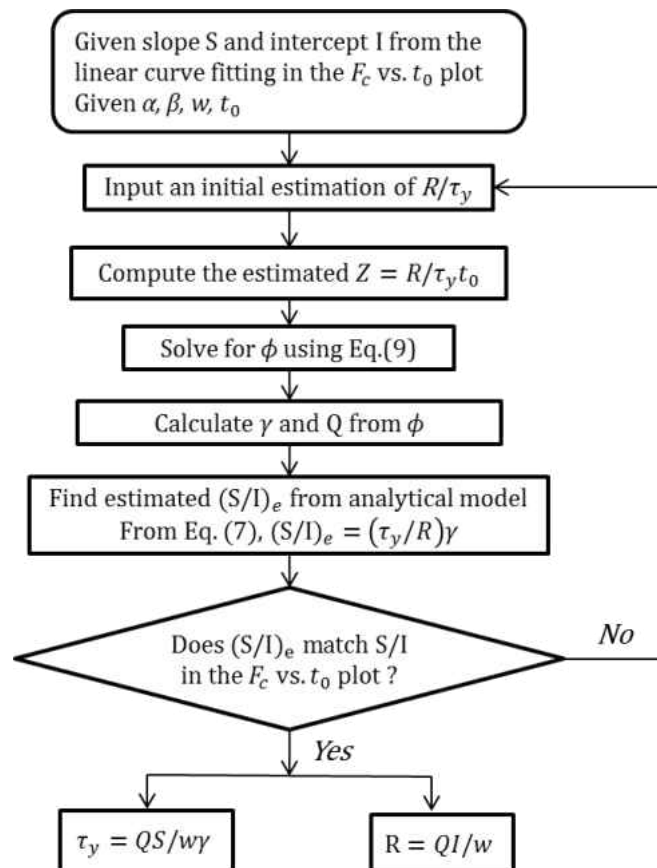


Figure 5-13. An iterative process of determination of shear angle ϕ , rigid-plastic yield stress τ_y , and specific work of surface formation R in the algebraic model from F_c vs. t_0 plot

It can be noticed from the flow chart that the algebraic solutions ($\phi, \gamma, Q, \tau_y, R$) are mostly determined by the slope S and intercept I values given in the linear curve fitting of the F_c vs. t_0 plot. Since Atkins' algebraic theory is only successful when continuous chips are formed and the load is steady, the F_c vs. t_0 plots given here were evaluated using the data points displaying linear relations within the regime of continuous chip formation. That is, first, the data points within the regime of discontinuous chip formation were ignored; second, the data points at the smallest depth of cut (0.05mm) were discarded since they were within the non-linear “drooping down” region. The remaining data points were fitted using least square method and the results are shown in Figure 5-14, including the regressed equations between F_c and t_0 .

Figure 5-15 (a-e) show a comparison, at different rake angles and depths of cut, between the shear angle ϕ measured from FEM simulations and predicted by the algebraic model. The dashed lines refer to the analytical solutions and the error bars indicate the estimated values from FEM simulations. For each simulation case, three ϕ angle values - minimum, medium and maximum possible values - were measured manually from the stress-concentrated area along the primary shear plane (Figure 5-15 (f)). The difference between the maximum and minimum values gives the magnitude of deviation of an error bar. From the closed-form solution of ϕ in Eq. (5-9), the analytical model predicts nearly constant ϕ over the range of depths of cut investigated, while decreasing rake angle α lowers the ϕ curves. The analytical solutions agree well with the measured values at small and zero rake angles (Figure 5-15 (c-e)), yet overestimate them at large rake angles (Figure 5-15 (a-b)). The overestimation may be related with the estimated R/τ_y value from the

linear fitting result in the F_c vs. t_0 plot, but overall, it can be concluded that the analytical solutions satisfy to give reasonable quantitative agreement with FEM simulation measurements.

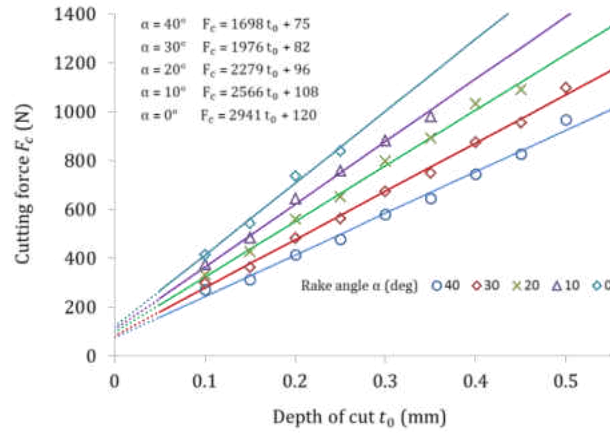


Figure 5-14. Cutting force F_c vs. depth of cut t_0 plot and linear curve fitting within the regime of continuous chip formation only

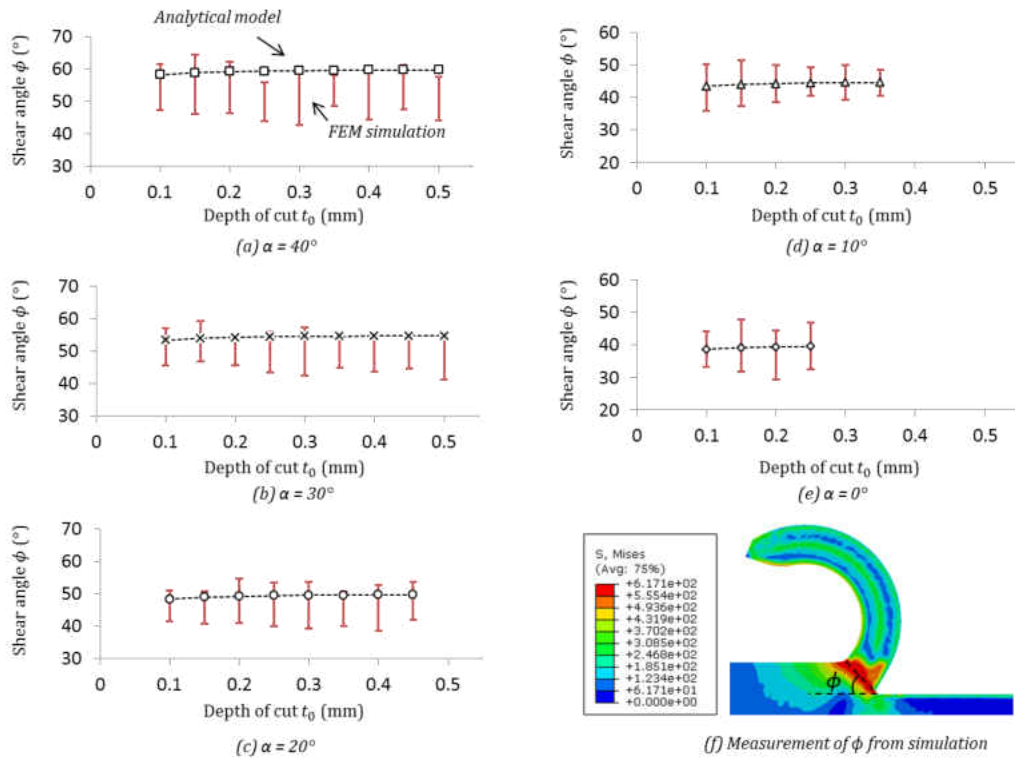


Figure 5-15. A comparison of shear angle ϕ between calculations from analytical model and measurements from FE simulations

Figure 5-16 shows the primary shear strain γ , friction correction parameter Q , and their ratio γ/Q calculated from the analytical model. It can be seen that at those depths of cut where ϕ is constant, γ , Q and γ/Q are also constant for given α . As $t_0 \rightarrow 0$, Q increases marginally towards to unity.

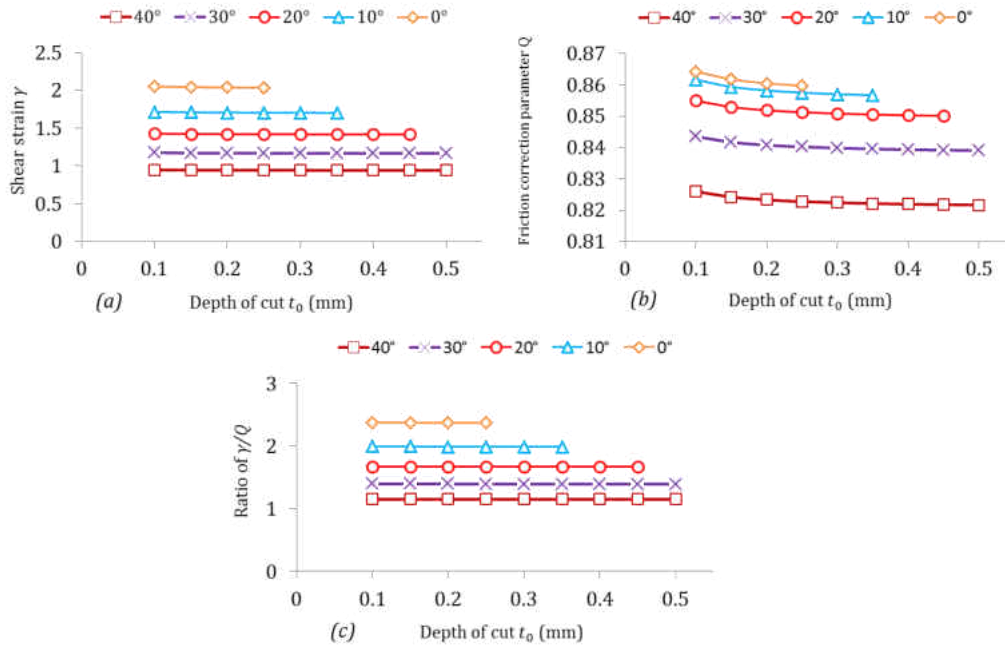


Figure 5-16. Analytical results of (a) shear strain γ (b) friction correction parameter Q (c) ratio γ/Q with respect to different depths of cut t_0 at each rake angle α

It follows from Eq. (5-7) that when continuous chips are formed, and in the range where γ/Q is constant, F_c plots linearly against t_0 with slope of $w\gamma\tau_y/Q$. The shear yield stress τ_y from the analytical model, therefore, equals to $QS/w\gamma$, where S is the slope in the linear F_c vs. t_0 plot. In FEM simulations, τ_y can be calculated indirectly from the primary shear zone. According to the von Mises yield criterion assumed in this study, $\tau_y = \sigma_y/\sqrt{3}$, where σ_y is the von Mises yield stress. Since τ_y is defined as rigid-plastic shear yield stress, but the JC hardening model was

employed in the simulations, σ_y is hence different from element to element. Therefore, σ_y along the primary shear zone was taken as an averaged value of JC equivalent yield stress from the highlighted elements shown in Figure 5-17 (a). It is important to note that during the steady-state cutting regime, the individual and averaged values of SDV2 in the elements within the primary shear zone are approximately the same at different instants.

Figure 5-17 (b) shows the comparison of shear yield stress τ_y between analytical and FEM simulation results with respect to rake angle α . Undoubtedly, τ_y also depends on depth of cut t_0 , however, both analytical and simulation results indicate that the effect of t_0 on τ_y is almost negligible. It can be seen from Figure 5-17 (b) that simulation results agree well with analytical predictions: τ_y is nearly constant (~ 350 MPa) for all rake angles calculated from simulation results; however, the analytical model predicts an increasing τ_y (310-370 MPa) as α increases. Strictly speaking, τ_y is a material constant and should be independent of depth of cut t_0 and rake angle α . The deviation of analytical solutions as compared to the nearly constant FEM simulation results could be caused by the shear angle ϕ which subsequently influences the Q/γ value.

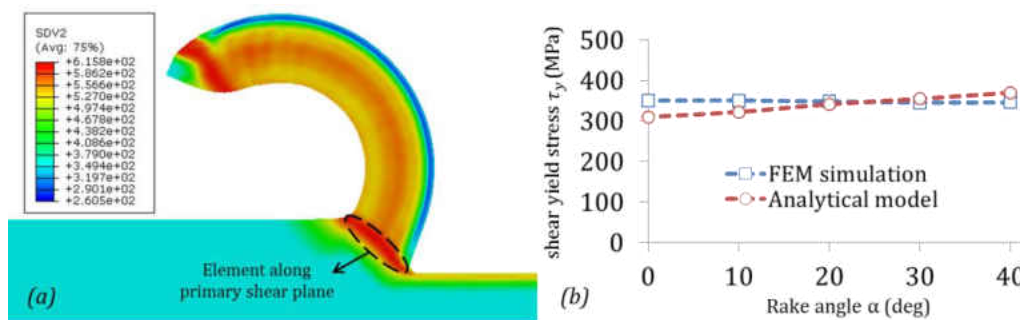


Figure 5-17. (a) Elements along primary shear plane were used for calculating the shear yield stress τ_y (b) Comparison of shear yield stress τ_y between FEM simulations and analytical model

The analytical solution for the work of new surface formation (or fracture toughness) R is related to the positive intercept I in the linear F_c vs. t_0 plot: $R = QI/w$. In FEM simulations, as derived in Section 5.5.4, R is linked with averaged plastic strain energy density $(dU_{pl})_{avg}$ and height of the boundary layer h . In Figure 5-12, $(dU_{pl})_{avg}$ is known at each t_0 and α . Now it remains to determine h . For continuous chip formation, separation of material occurs at the tool tip, to form highly deformed boundary layers contiguous with all practically cut surfaces. As shown in a contour plot from simulation (Figure 5-18), the boundary layer zone essentially consists of three sublayers: (1) the underside of the chip (2) the separation zone and (3) the top of the machined surface. From the fracture mechanics point of view, the energy required for material separation mainly comes from the plastic deformation energy around the advancing crack tip and newly created rough surfaces. When the tool tip travels through the separation zone, not only the plastic deformation energy in the deleted elements in sublayer (2), but also certain amount of plastic work in sublayers (1) and (3) contribute to the total work of surface formation. In other words, the plastic work in sublayer (2) gives a lower-bound value of R . The upper-bound value of R , however, depends on the height of sublayer (1) and (3). For the present simulations with mesh size of $20\ \mu\text{m}$, a reasonable attempt for the value range of h would be between $20\ \mu\text{m}$ (only sublayer (2)) and $60\ \mu\text{m}$ (sublayer (1) + (2) + (3)). Figure 5-19 shows the result for fracture toughness R given by both analytical and simulation calculations. Since Q is independent of depth of cut t_0 for given rake angle α (Figure 5-16 (b)), the analytical solution of R is correspondingly independent of t_0 . Hence Figure 5-19 is presented with respect to rake angle α only, in which each error bar indicates the range of R values at different t_0 converted from simulation outputs $(dU_{pl})_{avg}$. It is

further assumed here that the height of the boundary layer h is independent of t_0 and α . Three values of h were attempted: 20 μm , 60 μm and 35 μm . It can be seen from Figure 5-19 that 35 μm appears to be a reasonable size for the boundary layer.

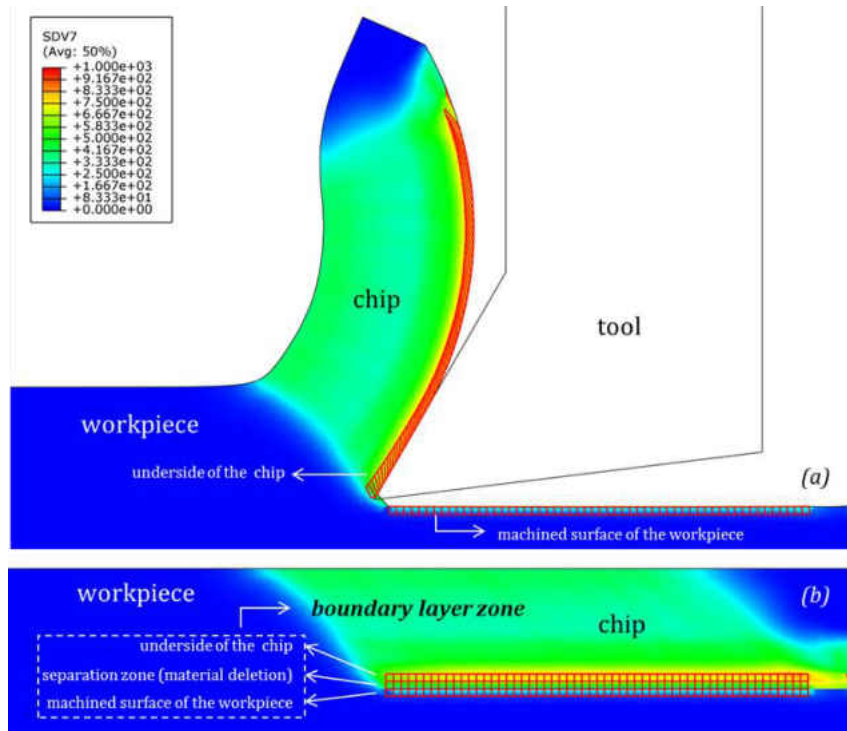


Figure 5-18. (a) Boundary layer zone on a contour plot of deformed shape (b) Boundary layer zone on a contour plot of undeformed shape. The boundary layer zone contains three sublayers on the contour plot of undeformed shape.

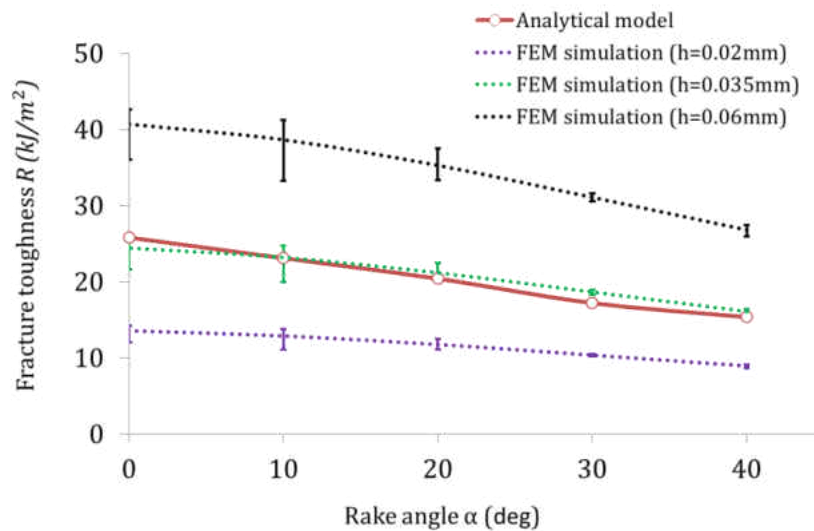


Figure 5-19. Comparison of specific work of new surface formation R (fracture toughness) between simulation results and analytical solutions using three h values. The magnitude of error bar at each rake angle indicates the range of R at different t_0 converted from $(dU_{pl})_{avg}$ in simulations.

Both analytical and simulation results predict greater fracture toughness value R at smaller rake angle α . The reasons are as follows. First, the underside of the chip accumulated more equivalent plastic strain from greater compressive deformation at smaller α . Second, in the case of continuous chip formation during orthogonal cutting process, mixed tensile and shear fracture mode coexist. The JC equivalent fracture strain is a monotonic decreasing function of stress triaxiality. When the rake angle decreases, shear fracture becomes more dominant; elements will be deleted at larger fracture strain. Wyeth and Atkins (2009) postulated a simple rule of estimating the mixed mode fracture toughness from R_I (tensile) and R_{II} (shear) at different rake angles, however, what governs the mixity still needs further investigation.

5.7 Discussions and Summary

The effectiveness of the present FEM modelling methodology can be cross-checked from a separate case study (Mabrouki et al., 2008) where the rake angle $\alpha = 17.5^\circ$ and cutting velocity $V_c = 800$ m/min. Figure 5-20 compares the chip morphology and cutting force with the experimental and numerical results in Mabrouki et al. (2008). The saw-tooth chip morphology in Figure 5-20 (a) is similarly predicted as Figure 5-20 (b) and (c). The present simulation result shows less saw tooth thickness on the chip segment. This is because self-contact of the workpiece in (Mabrouki et al., 2008) provokes more bending on the chip and consequently induces chip fragmentation. Other phenomena in the experiments, such as thermal softening, pre-existing micro-cracks and machine tool vibrations could also participate in the formation of saw-tooth chip shape (Mabrouki et al., 2008). However, the present model successfully predicted the experimental cutting force within a reasonable error range (7%). The validity of the present FEM model encourages the “simulation experiments” on the study of separation zones.

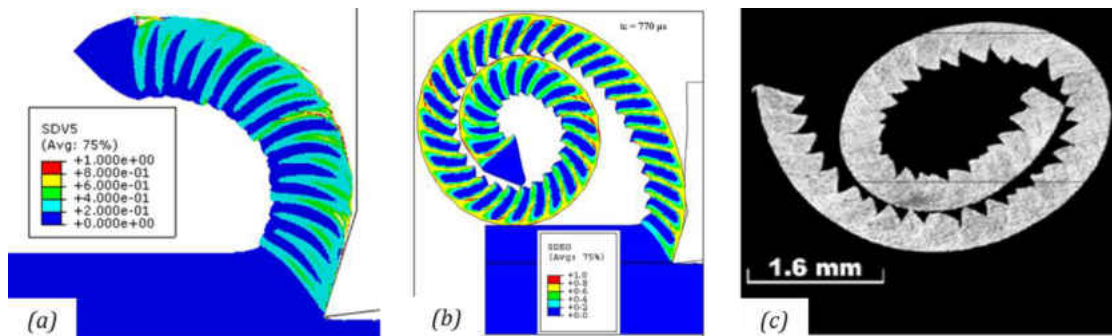


Figure 5-20. (a) Damage evolution and chip morphology in the present study ($\alpha = 17.5^\circ$, $V_c = 800$ m/min) (b) FEM simulation result of damage evolution in Mabrouki et al. (2008) (c) chip morphology in real experiment ($t_0 = 0.4$ mm, $V_c = 800$ m/min) in Mabrouki et al. (2008)

In both algebraic modelling and FEM simulations, a constant friction coefficient 0.17 was used for simplicity. In actual cutting experiments, the effective friction coefficient μ is usually

determined by resolution of the force F_T perpendicular to the cut surface and the cutting force F_C parallel to the surface (Atkins, 2009). The horizontal and vertical force outputs from the present FEM simulations, which can be considered as “experimental forces”, predict that the friction angle β varies with rake angle and depth of cut (Figure 5-21). This is not unexpected, since μ is known to alter with increase of t_0 owing to a change in the relative lengths of ‘sticking’ and ‘sliding’ regions along the rake face of the tool (Atkins, 2015). More elaborate friction models expressed in terms of normal and frictional stress have been introduced and modified by other researchers (Childs, Maekawa, Obikawa, & Yamane, 2000; Dirikolu et al., 2001; Obikawa & Usui, 1996; Ohbuchi & Obikawa, 2005; Sasahara et al., 1996; Shirakashi & Usui, 1974; Usui & Shirakashi, 1982). By comparing with experimental results, it is concluded in (Özel, 2006) that the predictions are more accurate when using variable friction models at the tool-chip contact in the FE simulations.

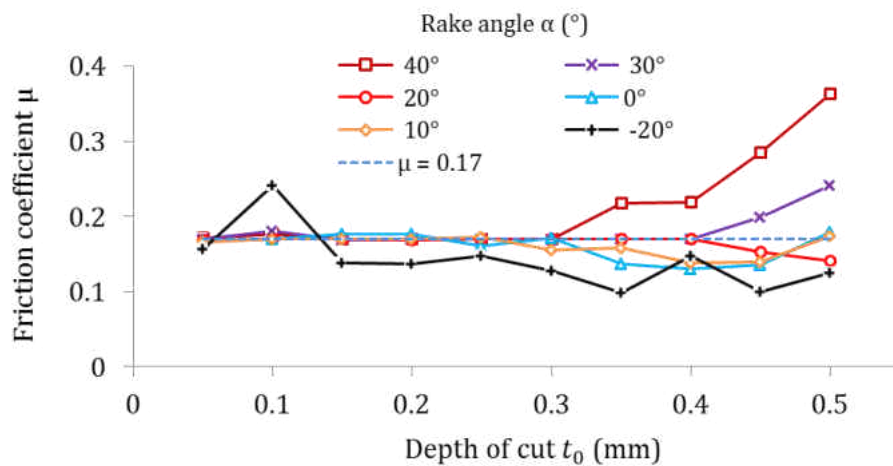


Figure 5-21. Friction coefficient μ calculated from Atkins algebraic model for all α and t_0

We may conclude from Section 5.6 that the simple single shear plane algebraic model has very good capability of predicting continuous chip formation, quasi-steady forces, and giving

satisfactory agreement with ϕ , τ_y and R values calculated from FE simulations. Another interesting question to ask is how plasticity, friction and fracture contribute to the total work. Figure 5-22 gives the proportions of total work due to plasticity, friction and fracture at rake angle 30° based on the analytical model. It is obvious from Figure 5-22 that large depth of cut involves a smaller proportion of fracture work because R is nearly constant but cutting force increases. The proportion of friction, however, is almost constant for all depths of cut due to the friction correction parameter Q. Consequently, total work attributed to plasticity increases with depth of cut for a given rake angle. The proportion of fracture work can be significant from 7.5% to 24.5% in continuous chip machining. Examination of other rake angle cases suggests that the proportion of plasticity, friction and fracture work tends to be similar to the present case.

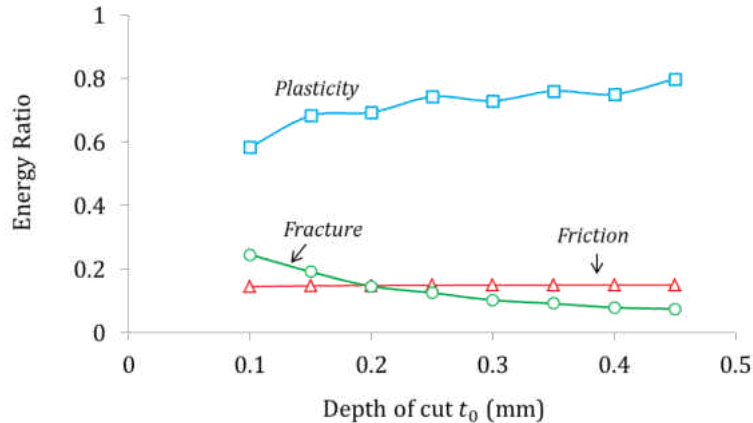


Figure 5-22. Proportions of plasticity, friction and fracture work at rake angle $\alpha = 30^\circ$

In this paper, the FE simulations of orthogonal cutting using the Johnson-Cook fracture criterion demonstrate that the present method gives great promise for evaluating material separation (damaged regions), the local work involved in separation of nodes and its relationship with algebraic models. The conclusions are summarized as follows:

- (1) FE simulations using the JC damage relation as a criterion for separation at the tool tip, predicted quasi-linear relation between cutting force F_c vs. depth of cut t_0 at large positive rake angles α over the range of t_0 investigated. Linear behaviour was also observed at small α but limited to certain range of t_0 . At negative α , F_c is possibly linear with t_0 but further investigations are required.
- (2) At the smallest depth of cut, the FEM predictions for cutting force depart from linearity and “curve down towards the origin”, but still do not pass through the origin and have a positive intercept as t_0 tends to zero.
- (3) The JC damage criterion, expressed as a plastic work/volume (plastic strain energy density), together with the size of the highly deformed boundary layer, is related to the fracture toughness as determined from the force intercept. The slope in the linear F_c vs. t_0 plot relates to the shear yield stress.
- (4) The boundary layer contains three sublayers contiguous with all practically-cut surfaces: the underside of the chip, the separation zone and the machined surface of the workpiece. The associated plastic work within the boundary layers must be included in the total work of surface formation.
- (5) The size of the damaged boundary layer is some 35 μm and appears to be independent of t_0 and α over the range investigated within the regime of continuous chip formation.
- (6) The material length scale is given by $R/k \approx (20 \times 10^3)/(350 \times 10^6) \approx 6 \times 10^{-5}$. The boundary layer therefore is some $0.6(R/k)$.
- (7) For continuous chip formation, Atkins’ single shear plane algebraic model gives satisfactory quantitative agreement with the shear angle ϕ , fracture toughness R and shear

yield stress τ_y as compared to FE simulation results. The results successfully validate that in cutting with continuous chips, works of plasticity, friction and separation are essentially uncoupled.

CHAPTER 6 APPLICATIONS OF DUCTILE FRACTURE MODELING IN METAL FORMING PROCESSES

In this chapter, the ductile fracture modeling method is applied to predict fracture initiation of advanced high strength steels (AHSS) sheets in (1) square punch tests (2) Nakazima tests and (3) three point bending tests of hat-sections. These tests are common engineering practices for metal sheet industrial applications in investigation of part loading history effect, determination of material formability and fracture, and validation of material model for structural components. Specifically, for ductile fracture modeling, they are good candidates for validating the fracture model calibrated from coupon test from a given grade of metal sheet. The experimental results are compared with finite element simulation results using calibrated plasticity and fracture parameters.

Advanced high strength steels (AHSS) have been developed in automotive industry over the past decade to meet the requirements for safety, efficiency, manufacturability, durability and quality at a low cost. AHSS provide high-strength and other advantageous properties, while maintaining key criteria including crash performance, stiffness and forming requirement. In spite of the advantages of AHSS, low formability is a primary drawback. Forming limit by necking or instability have been of interest to sheet metal forming because once necking occurs, thinning will progress rapidly under decreasing loads or pressures until the sheet cracks. Forming limit diagram (FLD) is widely used in deep-drawing industry as a useful tool for predicting limits of sheet forming operations. Analytical models were proposed for calculating limit strains and constructing FLDs of sheet metals, such as Hill's localized necking model (Hill, 1952), Swift's diffuse necking model (Swift, 1952), and Marciniak-Kuczynski (M-K) model (Marciniak & Kuczyński, 1967; Marciniak, Kuczyński, & Pokora, 1973) based on thickness imperfection. However, under some

circumstances (e.g. deep drawn and stretched parts with complex geometries), FLD cannot indicate whether the sheet failure occurs by local necking or fracture, whereas ductile fracture is the main factor that limits the attainable deformation of metal sheets (Atkins, 1996).

Numerous studies have been conducted on ductile fracture of metals such as steel and aluminum alloys over the last few decades. One large group of research is on physically based fracture models, based on mechanisms of nucleation, growth and coalescence of micro-voids (Tvergaard & Needleman, 1984). In parallel, there has been a growing interest in developing phenomenological models (Bai & Wierzbicki, 2008, 2010, 2015) which can be calibrated from adequate number of tests on bulk and/or sheet metals. In this paper, the modified Mohr–Coulomb (MMC) failure criterion proposed by Bai and Wierzbicki (2010) is used as an original fracture locus in the space of stress triaxiality, Lode angle parameter and equivalent plastic strain. The MMC fracture model covers a wide range of loading conditions. It does not only include uniaxial tension to equi-biaxial tension as in conventional FLD, but also enables to predict shear and compressive failure (Kim, Sung, Piao, & Wagoner, 2011; Li, Luo, Gerlach, & Wierzbicki, 2010). There are only four parameters in MMC fracture criterion and it is hence a good choice for industrial applications (Jia & Bai, 2016a, 2016b; Li et al., 2010).

6.1 Formability and Fracture tests

6.1.1 Square Punch Tests

The AHSS sheet is 1.58 mm thick DP780 from ArcelorMittal. The square punch tests were conducted to obtain fracture strain at different critical locations. For all tests, the sheets are in square shape with initial side length $D_0 = 7.50$ inch. The radius of the die entry r_d is 0.258 inch.

The punch features a square cross-section with edge length of $d = 3.50$ inch. The radius of the square punch head r_p is 0.468 inch. Corresponding blank-holders were employed to match the punch geometry. In order to investigate different fracture behavior, the sheet was arranged at two orientations (0° and 45°) by rotating the rolling direction of the sheet with respect to the coordinate system of the punch. The velocity of the punch travel is 5 mm/s. The schematic diagram of the square punch test is shown in Figure 6-1.

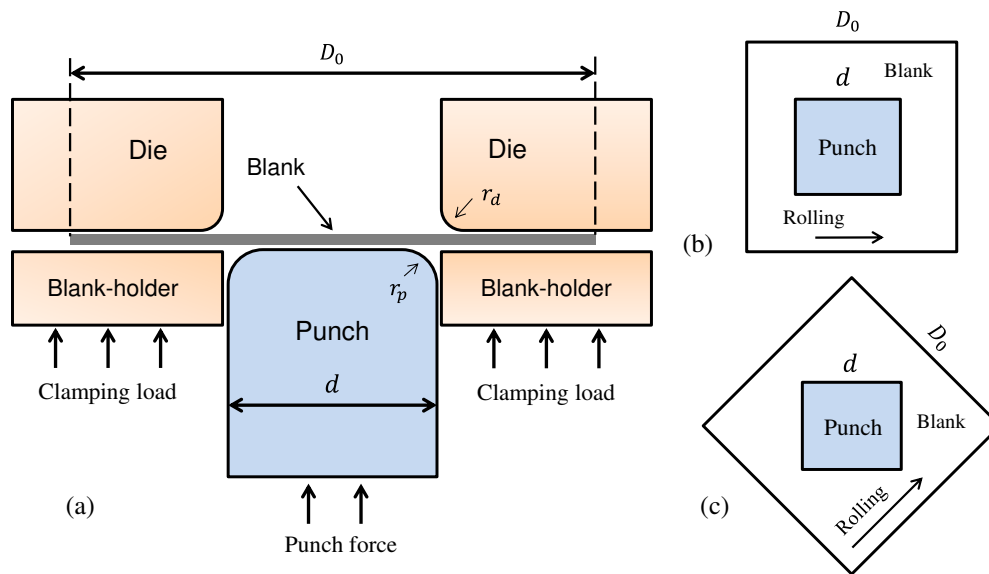


Figure 6-1. (a) Schematic diagram of the square punch test (front view) (b) top view of square punch test with 0° sheet orientation (c) top view of square punch test with 45° sheet orientation

The test sheet samples were electrochemically gridded using square grids of 2.5 mm and lubricated with prelude before the tests started. During each punch test, constant clamping load was applied on the blank sheet as it drew into the die cavity. However, clamping load is different for different target fracture locations. For each test, the drawing depth was gradually increased until the first crack was observed on the sheet. The drawing depths and load–displacement responses were recorded. The samples were formed until a predefined load drop was detected.

After the test sample fractured, the strain on its fracture location was measured from the electrochemical grid. Two different fracture locations were observed: (1) at the corner of die radius for 45° oriented sheet and (2) at the corner of punch radius for 0° oriented sheet. The two test cases are named as DP-45 and DP-0 hereafter (Table 6-1). Each test case was repeated twice.

Table 6-1. Summary of square punch tests on DP780 sheet

Test	DP-45	DP-0
Blank orientation	45°	0°
Clamping load (kip)	50	130
Fracture location	Die entry	Punch corner
Major strain ε_1 at fracture	0.59 ± 0.01	0.22 ± 0.01
Minor strain ε_2 at fracture	-0.65 ± 0.01	-0.006 ± 0.001

6.1.2 Nakazima and Three-point Bending Tests

The Nakazima tests are widely used for determination of forming limit diagram (FLD) in sheet forming industrial applications. The FLD represents the intrinsic limit of a material in plastic deformation assuming a proportional strain path, and the principal of Nakazima test can be applied for construction of fracture forming limit diagram (FFLD) for less ductile AHSS sheets. The FLD is the localized necking strain limit and the FFLD is the fracture strain limit. In the present study, the Nakazima tests was carried out on QP980 sheets of 1.24 mm thickness in accordance with the ISO 12004-2. The Nakazima toolset has a die entry radius of 6.35 mm and a single circular drawbead with a height of 5.08 mm and a tight bend radius of 1.52 mm. In order to mitigate premature fracture at the drawbead during binding-closing process prior to the motion of the punch, a carrier blank was placed in between the AHSS blank and the blank holder. Oil-based lubrication

was applied in the contact areas between different parts to reduce friction. In all tests, the blank holder force was set to 400 kN and the punch velocity was set to 0.25 mm/s.

Figure 6-2 shows the strain paths at the critical location to the failure zone from DIC analysis of QP980 sheets under Nakazima tests. The diameter of the circular blank along the rolling direction is fixed at 7 inch, and different strain paths to fracture were obtained by altering the specimen width w : (1) uniaxial tension ($w = 1$ inch), (2) plane strain tension ($w = 4$ inch), (3) intermediate stretching strain state ($w = 5$ inch) and (4) equi-biaxial tension ($w = 7$ inch).

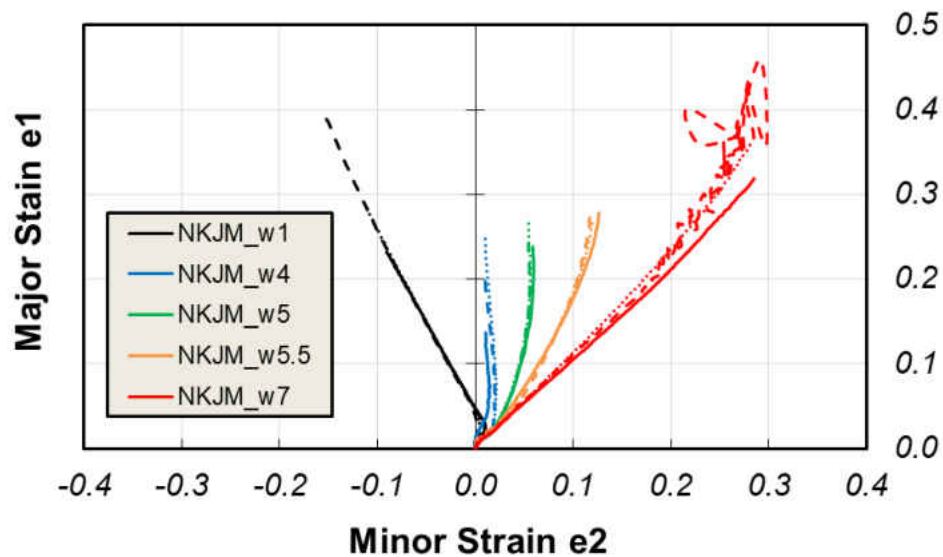


Figure 6-2. Strain paths to fracture of Nakazima tests of QP980

The 3-point-bending (3PB) tests on the hat sections of the same QP980 sheets (in Section 6.1.2) were conducted to validate the calibrated fracture models. The 3PB tests on the hat section samples are designed to simulate the side impact on automotive B-pillar structures (Figure 6-3 (a)). The experiments were conducted on a servo-hydraulic high-rate testing machine equipped with a 100 kN load cell. In each test, the anvil bent a sample by 100 mm from contact to stop at a nominal

speed of 10 mm/s. Each hat section sample has a width of 381 mm and the span of the two supporters beneath a sample was set to 305 mm. Figure 6-3(b) shows an example of the bent hat section sample – it is essentially a brake-bent top channel spot-welded to a base panel.



Figure 6-3. (a) B-pillar bending example (2016 Tesla Model S side IIHS crash test) (b) an example of three-point bending test on a hat section sample

6.2 Material Model Calibration

6.2.1 Isotropic Plasticity and Fracture Model

The present AHSS sheets are nearly isotropic. For plane stress condition, von Mises yield criterion is in the form of

$$\sigma_1^2 + \sigma_2^2 - \sigma_1\sigma_2 = \sigma_Y^2 \quad (6-1)$$

where σ_1 , σ_2 are two principal stresses on the sheet plane, and σ_Y is the von Mises equivalent yield stress.

Proper identification of the strain hardening after the onset of necking is very important for reliable determination of the fracture strains. Two approaches are suggested for extrapolate the hardening curve in the post-necking regime from recent studies. The first approach is to use an

inverse method of manually adjusting the true stress-strain data in the post-necking regime until force-displacement curve from simulation agrees well with that from the experiment (e.g. (Luo et al., 2012)). The second approach is to use a linear combination of a power hardening and saturation type of hardening law, inspired by the work in (Sung et al., 2010) and followed-up by Mohr and co-workers (Marcadet & Mohr, 2015; Mohr & Marcadet, 2015; Roth & Mohr, 2014). The combined Swift-Voce hardening function ensures a smooth piece-wise increasing curve and improves the efficiency of model calibration compared to the inverse method. The second approach is adopted in the present study. The combined isotropic strain hardening function is represented as

$$k(\bar{\varepsilon}_p) = \alpha k_s(\bar{\varepsilon}_p) + (1 - \alpha)k_v(\bar{\varepsilon}_p) \quad (6-2)$$

where the Swift law is a power law function

$$k_s(\bar{\varepsilon}_p) = A(\varepsilon_0 + \bar{\varepsilon}_p)^n \quad (6-3)$$

and the Voce law is an exponential function

$$k_v(\bar{\varepsilon}_p) = k_0 + Q \left(1 - \exp(-\beta \bar{\varepsilon}_p) \right) \quad (6-4)$$

The parameters of the Swift and Voce hardening law are calibrated separately from curve fitting of the true stress-plastic strain up to necking. The weighting factor α was determined iteratively by comparison with engineering stress-strain curve in the post-necking regime. The material hardening parameters are summarized in Table 6-2. The extrapolated combined Swift-Voce hardening curve is illustrated in Figure 6-4.

Table 6-2. Isotropic hardening parameters of DP780 and QP980

Parameter	A	n	ε_0	α	k_0	Q	β
DP780	1180	0.12	0.001	0.6	595	316	28
QP980	1749.6	0.215	0.008	0.6	654.6	559.5	14.98

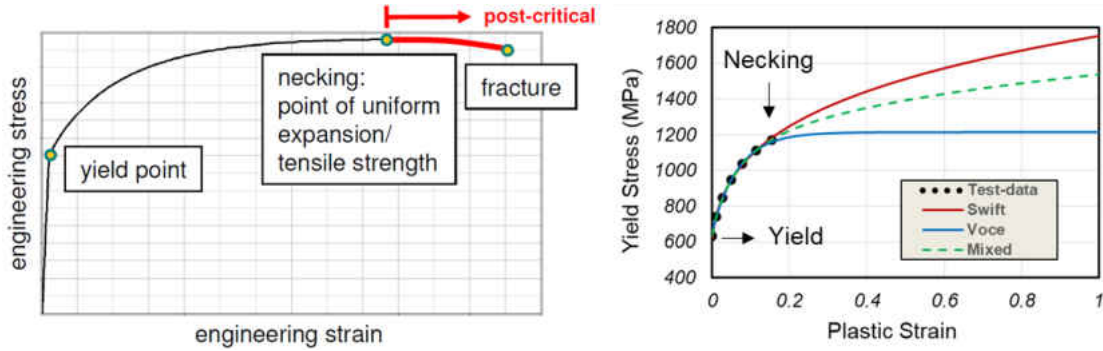


Figure 6-4. (a) Illustration of the post-critical regime after necking in the engineering stress-strain curve (b) an example of post-necking extrapolation by combined Swift-Voce law

The modified Mohr-Coulomb (MMC) phenomenological model was applied for modeling ductile fracture locus. The MMC fracture criterion reads

$$\bar{\varepsilon}_f(\eta, \bar{\theta}) = \left\{ \frac{A}{C_2} \left[C_\theta^s + \frac{\sqrt{3}}{2 - \sqrt{3}} (C_\theta^{\alpha x} - C_\theta^s) \left(\sec \frac{\bar{\theta}\pi}{6} - 1 \right) \right] \left[\sqrt{\frac{1 + C_1^2}{3}} \cos \frac{\bar{\theta}\pi}{6} + C_1 \left(\eta + \frac{1}{3} \sin \frac{\bar{\theta}\pi}{6} \right) \right] \right\}^{\frac{1}{n}} \quad (6-5)$$

Here, η is the stress triaxiality; $\bar{\theta}$ is Lode angle parameter; A , n , C_1 , C_2 , C_θ^s and $C_\theta^{\alpha x}$ are the MMC fracture model parameters. Note that the fracture model parameters A and n are decoupled from the Swift hardening model, but the same values can be chosen as initial estimations.

In the case of plane stress, the stress triaxiality η and Lode angle parameter $\bar{\theta}$ are uniquely related by Bai and Wierzbicki (2008)

$$-\frac{27}{2} \eta \left(\eta^2 - \frac{1}{3} \right) = \sin \left(\frac{\pi}{2} \bar{\theta} \right) \quad (6-6)$$

The original MMC fracture model is stress-based because the fracture strain is a function of two stress invariants - stress triaxiality and Lode angle parameter. However, the stress-based

parameters are difficult to measure in practical applications, and the model calibration relies on the inverse method from finite element simulations. It is therefore desired to develop an all-strain-based ductile fracture model directly applicable for model calibration. For metal sheet applications, under the plane stress condition and associated flow rule, the stress invariant based MMC fracture locus can be transferred into the fracture forming limit diagram (FFLD) defined in the space of principal strains. The transformation from MMC to FFLD is shown in the following.

The transformation from stress-based MMC to strain-based FFLD are related to the strain incremental ratio α and stress ratio β , defined as

$$d\varepsilon_2 = \alpha d\varepsilon_1, \quad \sigma_2 = \beta \sigma_1 \quad (6-7)$$

Assuming the Mises-Levy flow rule, it can be derived that

$$\alpha = \frac{2\beta - 1}{2 - \beta} \quad (6-8)$$

The relationship between the stress triaxiality η and the stress ratio β is

$$\eta(\beta) = \frac{\sigma_m}{\bar{\sigma}} = \frac{\sigma_1 + \sigma_2}{3\sqrt{\sigma_1^2 + \sigma_2^2 - \sigma_1\sigma_2}} = \frac{\beta + 1}{3\sqrt{\beta^2 - \beta + 1}} \quad (6-9)$$

Using the relation between the strain incremental ratio α and stress ratio β in Eq.(6-8), there is a unique relation between η and α

$$\eta(\alpha) = \frac{\alpha + 1}{\sqrt{3}\sqrt{\alpha^2 + \alpha + 1}} \quad (6-10)$$

The equivalent plastic strain incremental $d\bar{\varepsilon}$ can be expressed in the form of

$$d\bar{\varepsilon} = \frac{2d\varepsilon_1}{\sqrt{3}} \sqrt{\alpha^2 + \alpha + 1} \quad (6-11)$$

Both the stress-based original MMC fracture locus and the strain-based FFLD describe the fracture limit based on proportional loading under linear strain path. The integral of Eq.(6-11) until fracture gives the relation between fracture strain $\bar{\epsilon}_f$ and maximum principal strain ϵ_1 :

$$\bar{\epsilon}_f = \frac{2\epsilon_1}{\sqrt{3}} \sqrt{\alpha^2 + \alpha + 1} \quad (6-12)$$

The 2D MMC fracture locus can be transformed to the space of principal strains using Eq.(6-12). Using the transformation equations of (6-7) to (6-12), the calibrated fracture locus in form of stress-based MMC and strain-based FFLD are shown in Figure 6-5 and Figure 6-6.

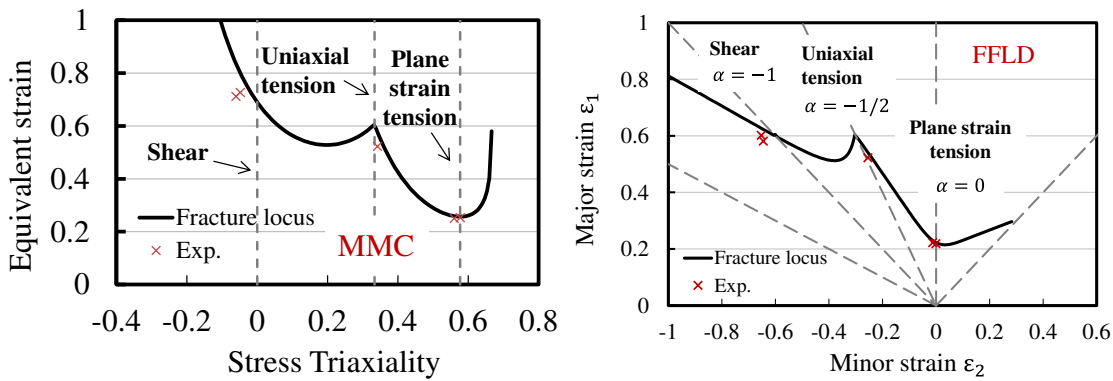


Figure 6-5. The MMC fracture locus and the fracture forming limit diagram (FFLD) calibrated from uniaxial tension and square punch tests of DP780 sheets.

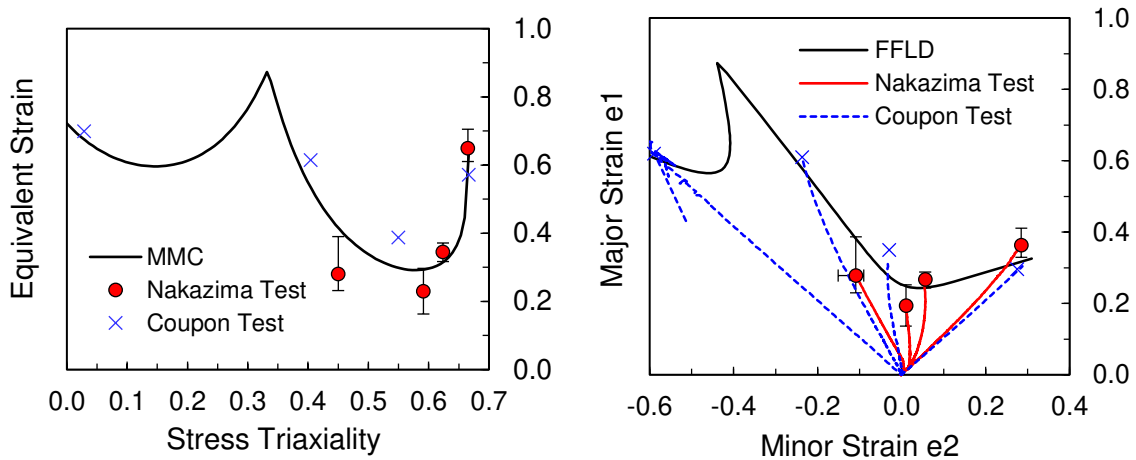


Figure 6-6. The MMC fracture locus and the fracture forming limit diagram (FFLD) of QP980 sheets.

All the parameters in the MMC fracture model are decoupled from the plasticity model. The parameters are free to adjust with the best fit of the fracture data points. The calibrated fracture parameters for DP780 and QP980 are listed in Table 6-3.

Table 6-3. MMC fracture model parameters for DP780 and QP980

Parameter	A	n	c_1	c_2	C_θ^s	C_θ^s
DP780	1180	0.120	0.127	630.6	0.960	1.000
QP980	1750	0.215	0.220	1059.2	1.098	1.062

6.2.2 GISSMO Fracture Model in LS-DYNA

In LS-DYNA, GISSMO is the “Generalized Incremental Stress-State dependent Damage Model”. The GISSMO damage model is a phenomenological formulation that allows for an incremental description of damage accumulation including softening and failure (Manual, 2017). It can be used in combination with a variety of material cards available for metallic materials.

The incremental formulation of damage accumulation in GISSMO reads:

$$\Delta D = \frac{nD^{(1-1/n)}}{\varepsilon_f} \Delta \varepsilon_p \quad (6-13)$$

Where D is the damage variable ($0 \leq D \leq 1$), $\Delta \varepsilon_p$ is the equivalent plastic strain increment, n is the exponent for nonlinear damage accumulation, and ε_f is the equivalent plastic strain to failure determined as a function of the current triaxiality value η .

GISSMO allows stress softening from material instability up to the load-bearing capacity completely vanishing as D reaches unity. The model assumes damage coupling with stress once the material instability criterion is reached. The material instability criterion can be defined as an analytical instability model (e.g., Swift, Hill, Marciniak-Kuczynski, etc.), or an actual forming limit curve (FLC) measured from experiments. Similar to the definition of damage variable D , the

instability measure F is accumulated using the following relation and the instability curve is used as an input (Manual, 2017):

$$\Delta F = \frac{nF^{(1-1/n)}}{\varepsilon_{p,loc}} \Delta \varepsilon_p \quad (6-14)$$

Where $\varepsilon_{p,loc}$ defines the instability curve similarly as the fracture locus defined by ε_f in Eq.(6-13). When the instability measure F reaches unity, the current value of damage D in the respective element is stored as a critical damage D_{CRIT} . Damage from this point on will be coupled to the flow stress using the relation (Manual, 2017):

$$\sigma = \tilde{\sigma} \left[1 - \left(\frac{D - D_{CRIT}}{1 - D_{CRIT}} \right)^{FADEXP} \right] \quad (6-15)$$

Where $FADEXP$ refers to an exponent for damage-related stress fadeout. The GISSMO damage model is demonstrated by a simplified process as shown in Figure 6-7. The model was simplified using (1) constant critical plastic strain $E_{CRIT} = 0.16$ and (2) constant fracture strain $\varepsilon_f = 0.4$. Figure 6-7 illustrates the damage accumulation with evolution of plastic strain according to Eq. (6-13), and stress softening effect after material instability according to Eq. (6-15).

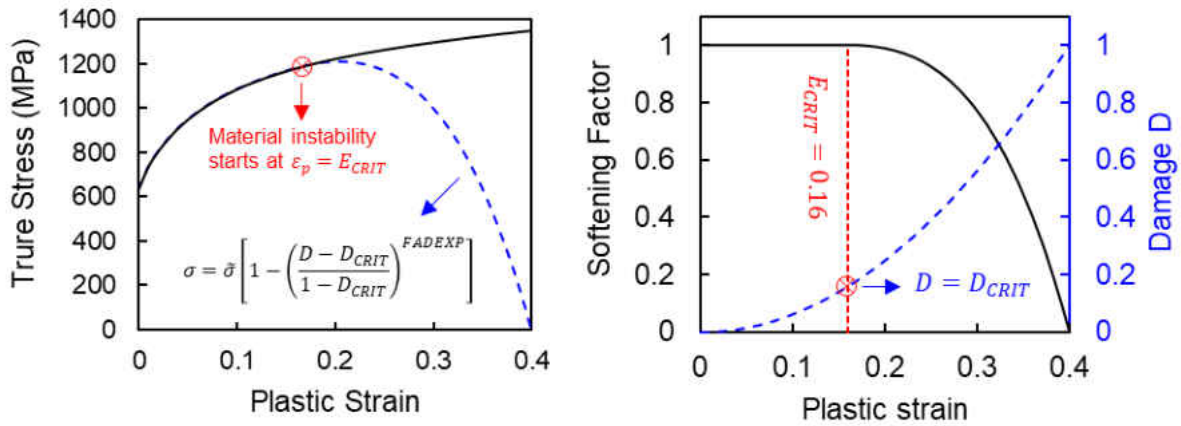


Figure 6-7. Demonstration of a simplified stress softening and damage accumulation for QP980 in GISSMO. The material instability and fracture strain are simplified as a fixed value of $E_{CRIT} = 0.16$ and $\epsilon_f = 0.4$. Non-linear damage accumulation exponent $n = 2$ and exponent for damage-related stress fadeout $FADEXP = 2$. The softening factor is the term in the bracket of Eq. (6-15).

Figure 6-8 illustrates an example of fracture locus and material instability curve defined for QP980. The fracture locus was calibrated from coupon test results in the last section, and the material instability curve was converted from the analytical Swift instability model using necking strain of 0.16. Note that for QP980, the post-necking regime, which is referred as the region between the fracture locus and the instability curve, indicates that material fracture is preceded by necking. At low triaxiality region ($\eta < 0.1$), necking is suppressed by fracture. Failure with strain localization or not prior to fracture is material dependent. Note that the choice of the instability curve is determined by the user. For real applications of forming or crashworthiness simulations using larger mesh sizes, the instability curve is not the only factor influencing the simulation results. The fading exponent in the damage coupling and regularization factor constitutes another two elements of the fracture strain regularization procedures.

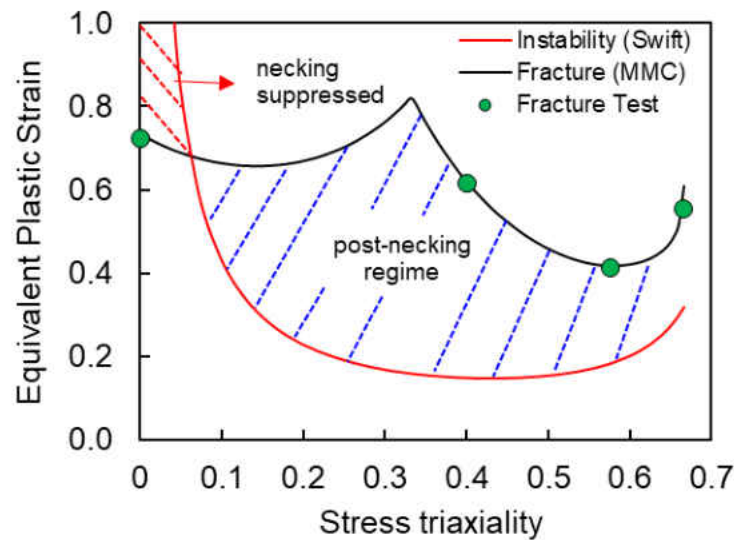


Figure 6-8. An example of MMC fracture locus and Swift instability curve of QP980 in GISSMO

6.3 Finite Element Simulations

6.3.1 Finite Element Model Setup

Finite element simulations of square punch tests were performed in ABAQUS/Explicit. The punch, the die and the blank-holder were modeled as discrete rigid bodies using 4-node 3D bilinear rigid quadrilateral elements (R3D4). The rigid bodies were discretized using global mesh size of 5 mm in the edge region and local meshes as fine as 1 mm at contact region. The square sheet was meshed by four-node, reduced integration points shell elements (S4R) with mesh size of 1 mm \times 1 mm. For all models, 5 Simpson integration points through the thickness of shell elements were assigned to obtain reliable simulation results which involve bending features.

Modeling metal forming process is a highly nonlinear problem which involves contact and large deformations. In order to obtain economical quasi-static solutions using an explicit dynamics solver, an appropriate mass scaling factor was applied during the explicit analysis. In the initial

step, a small gap between the blank-holder and the sheet was set up to avoid numerical oscillation caused by potential initial penetration during contact. The numerical analysis of the punching process was divided into two steps: In the first step, a blank-holder force was applied as a ramp load to establish contact between the blank-holder and the sheet. In the second step, the punch moved vertically at a constant velocity of 5 mm/s. During both steps, the die was fixed; the blank-holder and the sheet were given free boundaries. The punch was fixed in the first step and allowed for only vertical movement in the second step. The fracture initiation and crack propagation were modeled using element deletion technique. The element would be deleted when all integration points through thickness reach unity.

In the finite element analysis, penalty friction formulation was used to model the tangential behavior between contact surfaces. The friction coefficient was assumed constant in the contact areas between the interactions of the rigid tool and the blank. Since there is no direct method for determining the friction coefficients in the square punch test, an inverse method was adopted here to adjust friction coefficient to best correlate the experimental load-displacement curves. The load-displacement response of the punch is very sensitive to the friction coefficient. It is well known that friction changes the state of stress and strain in sheets (Lee, Woertz, & Wierzbicki, 2004). During the punch test, friction from the punch corner radius prevents tension across the face of the punch from increasing sufficiently to stretch the material over the face of the punch. At the corner of die radius, the contact friction also restricts material flow, thereby hinders the development of large tensile strain. The force acting on the punch is in equilibrium with the tension on the side-wall. The higher the friction, the tension is larger on the side wall. Friction also plays a key role of deciding the formation of neck and location of the fracture initiation. With high friction, fracture

tends to initiate near the contact with the punch, where the deformation is in plane strain tension because of the circumferential direction constraint from the neighboring material in contact with the punch. With lower friction, the maximum punch stroke increases, and the failure site moves toward the die corner.

6.3.2 FE Simulations of Square Punch Tests

Figure 6-9 and Figure 6-10 show the comparison between finite element analysis and test results for the two square punch test cases. For case DP-0, the crack is located at the punch radius of the sheet and propagated circumferentially, while the crack for the case of DP-45 is located at the die radius of the sheet and propagated circumferentially. The crack location and propagation for both cases are well captured by FE simulations.

The experimental and numerically predicted force-displacement curves for test case DP-0 and DP-45 are shown in Figure 6-11. The punch loads are predicted accurately for given clamping load and adjusted friction coefficients. The initially calibrated fracture locus almost predicts the accurate moment of fracture initiation. Fracture in simulations occurred slightly early but if the fracture parameters were fine-tuned, the simulation would give more accurate results. However, the most important is that by calibrating the original MMC fracture locus in the all-strain-based space, only one-time calibration is adequate for giving satisfactory results. No tedious iterations of FE simulations are needed. This is because the deformation at these two critical locations in square punch tests was dominated by proportional loading under linear strain path.

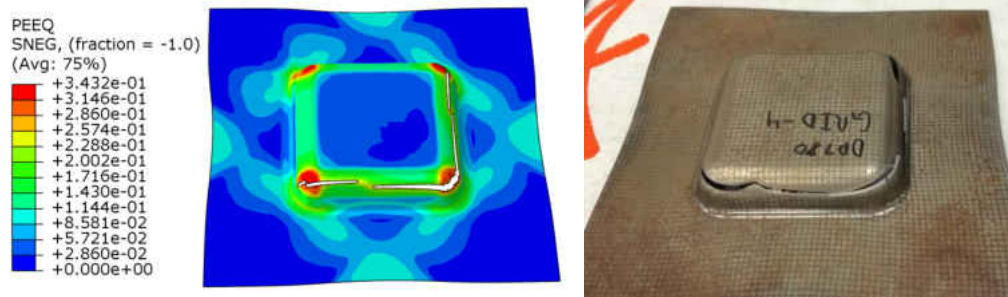


Figure 6-9. Finite element analysis and experimental results of square punch tests for case DP-0. Fracture initiates at the corner of punch radius. PEEQ denotes the equivalent plastic strain.

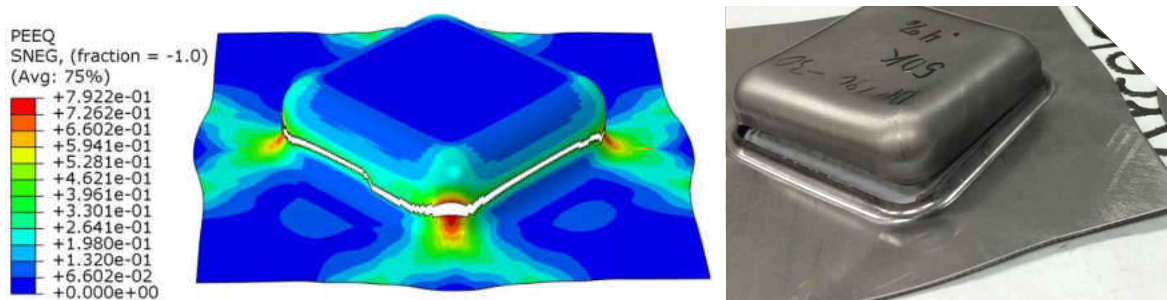


Figure 6-10. Finite element analysis and experimental results of square punch tests for case DP-45. Fracture initiates at the corner of die radius. PEEQ denotes the equivalent plastic strain.

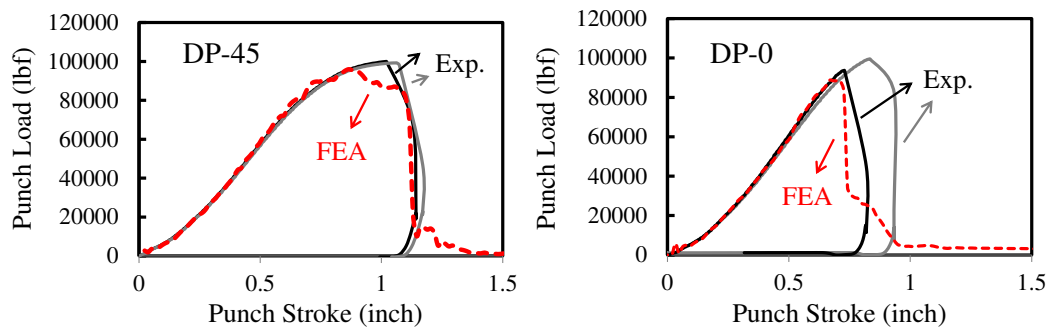


Figure 6-11. Experimental and numerically predicted force-displacement curves for test case DP-45 and DP-0.

During square punch test, material points at different locations on the sheet have different strain paths. The element at the corner of the punch radius is under a combined biaxial tension and bending. On the other hand, the element at the corner of the die radius experiences a combined bending and in-plane shear. The mechanism of generating in-plane shear at the corner of the die

radius is illustrated in Figure 6-12. The material point located at the intersection of two bending surface pairs is under combined tension and compression, which generates in-plane shear deformation at the corner. The relative amount of tension and compression under certain experiment conditions determines how close to pure shear it is. It was found in experiments that for DP780, it is possible to generate in-plane shear by rotating the sheet 45° with respect to the square punch when applying certain clamping load and sufficient lubrication.

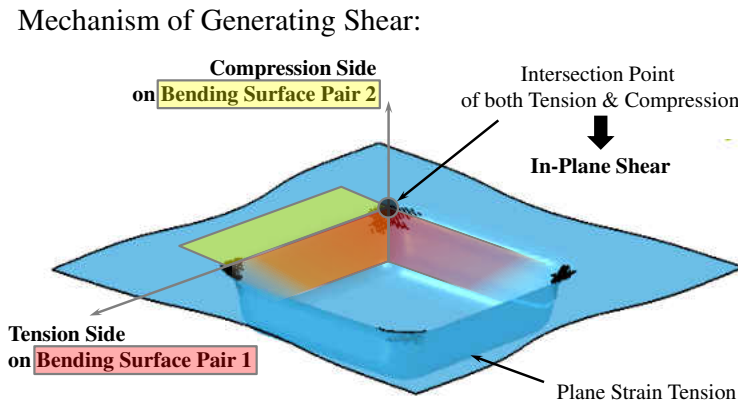


Figure 6-12. Illustration of the mechanism of generating in-plane shear in square punch test.

Figure 6-13 shows the strain histories extracted from the critical element at fracture initiation site (within the red regions in the contour plot of FE simulations) for each case. Strain paths of 3 integration points (5 used in analysis and 3 used for output) on the negative, middle, and positive surfaces are present in the figure. The strain path of the integration point on the middle surface is very close to proportional loading: (1) pure shear at the die radius for DP-45 and (2) plane strain tension at the punch radius for DP-0. For the outer surfaces, there are bending history effects so that the strain paths are not strictly linear. For the critical element at the corner of punch radius in case of DP-0, the material located on the positive surface is in equi-biaxial tension first and then shift to plane strain tension, while the material located on the negative surface is in

compression first and then shift to plane strain tension. Similarly, for the critical element at the corner of die radius in case of DP-45, the material located on the positive surface is in uniaxial tension first and shift to pure shear, while the material located on the negative surface is in compression first and then shift to pure shear.

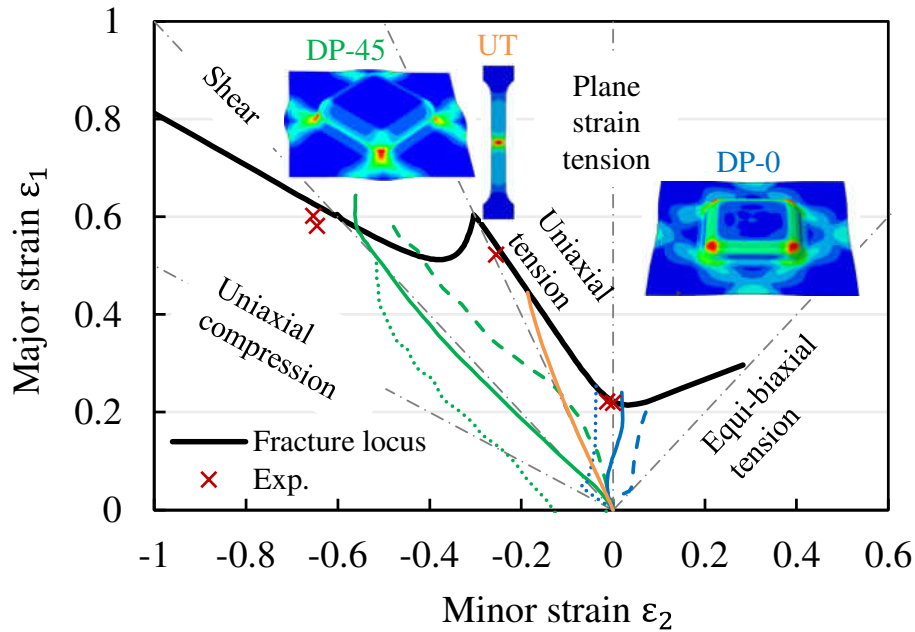


Figure 6-13. Strain histories extracted from the critical element at fracture initiation site for the case of (a) green: DP-45 (b) blue: DP-0 (c) orange: uniaxial tension in the space of principal strain. The solid, dashed and dotted lines represent the integration point on the middle, positive and negative surface, respectively.

Figure 6-14 shows damage evolution of the three integration points through thickness of the critical element for DP-0 and DP-45 during square punch test. Linear damage evolution law was used in Abaqus built-in damage model. Integration point fails when the damage indicator $D = \int_0^{\bar{\epsilon}_p} \frac{d\bar{\epsilon}_p}{\epsilon_f(\eta)} = 1$, where $\epsilon_f(\eta)$ is the fracture strain as function of stress triaxiality under different loading conditions. The damage evolution rule takes strain history effect and non-proportional loading into consideration. Elements are deleted if all integration points through thickness fail.

Fracture initiation site is identified as the crack position where the first element is deleted. Different than FLD determined by necking, the MMC fracture locus is not only as a strain limit, but also as an integral part of damage evolution rule.

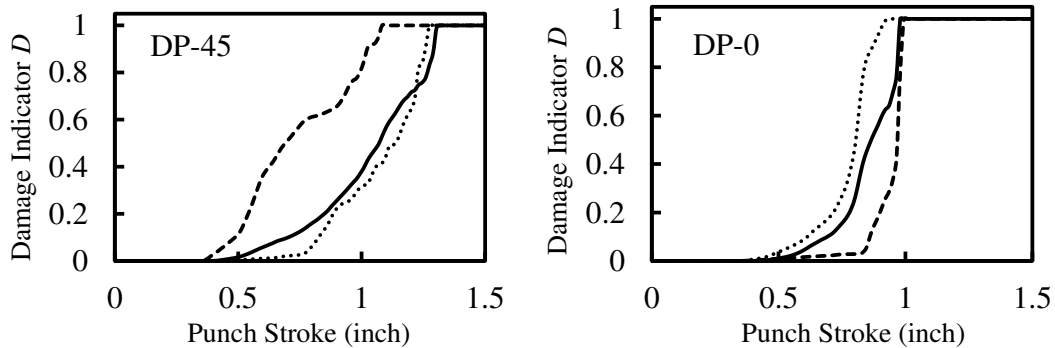


Figure 6-14. Damage evolution of the three integration points through thickness extracted from the critical element for case DP-45 and DP-0. The solid, dashed and dotted lines represent the integration point on the middle, positive and negative surface, respectively.

For case DP-0, the integration point on the negative surface of the critical element at the punch corner failed first, and the other two integration points failed rapidly thereafter. All the three integration points through thickness experienced similar proportional loading paths of plane strain tension. In Figure 6-15, it can be seen that the critical element experienced continuous thinning before it failed. Bending history effect on damage evolution of the critical element is not that significant. When the strain paths reach the FFLD in the space of principal strains, the damage indicator D reaches unity almost at the same time.

For case DP-45, the integration point on the positive surface of the critical element at the die corner failed first, but failure was delayed for the other two integration points. The three different damage evolution curves are attributed to bending effect. The strain path for the middle integration point is nearly linear under pure shear at all time, but the strain paths for the surface integration points are not strictly linear. Damage accumulation for the integration point on the

positive surface starts early from uniaxial tension and continues under pure shear, while it starts late for the integration point on the negative surface because it deformed first from compression, which features a very high fracture limit. In Figure 6-15, it can be seen that after the critical element started to flow into the die cavity, it was thickened first and then thinned, indicating a transition from compression to tension dominant state through pure shear. It is noted that if linear damage evolution rule was used as in this study, unless the strain path is strictly linear, whether it reaches the FFLD or not does not necessarily indicate the damage indicator D reaches unity simultaneously.

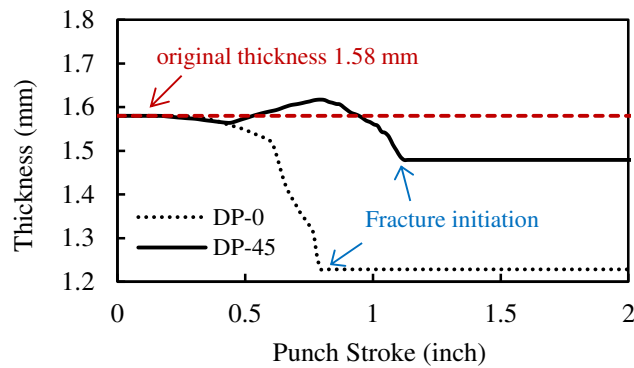


Figure 6-15. Thickness history of the critical element for case DP-0 and DP-45.

6.3.3 FE Simulations of Nakazima and Three-point Bending Tests

Figure 6-16 shows the force-displacement curve from FE analysis of the Nakazima tests and its comparison with experimental results. The force was measured from load sensors of the hydraulic press and the displacement is the punch stroke after the contact with the blank. The FE results agree very well with the experiments for uniaxial tension test ($w = 1$ inch) and equi-biaxial tension test ($w = 7$ inch). For plane strain tension ($w = 4$ inch) and intermediate stretching ($w = 5$ inch), some discrepancy is seen in the results. This is mainly caused by the use of an isotropic yield function. The global force and displacement at fracture can be better correlated with the test results

if an anisotropic yield function (e.g. Yld2000-2d) was employed for more accurate description of plastic flow and yield stress.

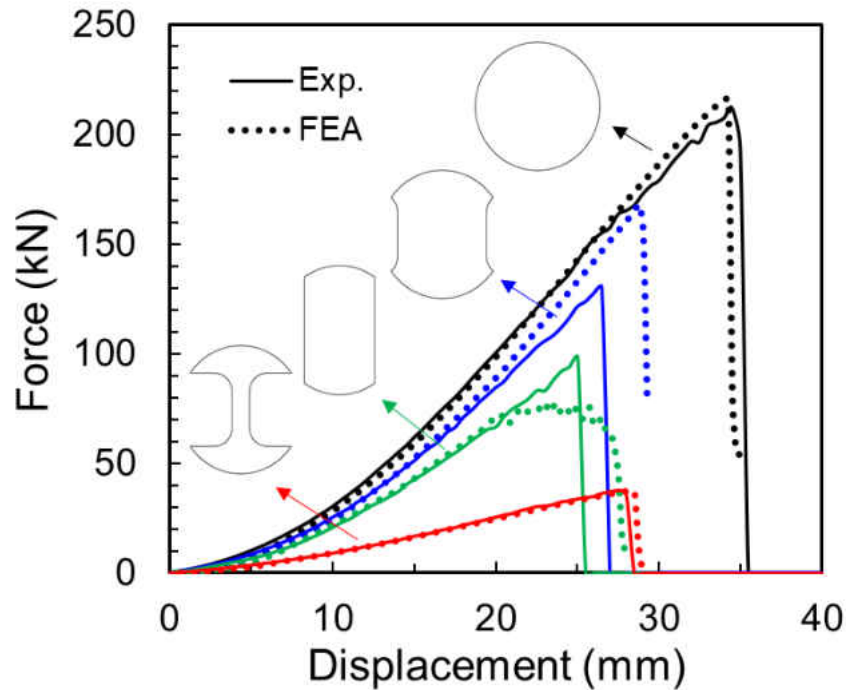


Figure 6-16. FE simulation results of Nakazima Tests of QP980 sheets

Figure 6-17 shows Nakazima test samples after fracture in both experiments and FE simulations. The fracture locations in the experiments are near the dome center and are well captured by the FE simulations except for the case of intermediate stretching. As discussed earlier, the friction effect influences the fracture location. In stretching over a hemispherical punch, the effect of friction is to reduce tension at the dome center and spread the strain over a greater area. The critical potential failure location is at some distance from the pole with the friction effect due to the relocation of maximum circumferential strain component. The strain distributions in Figure 6-17 (c) suggest that the fracture strain follows the fracture locus calibrated in Figure 6-6.

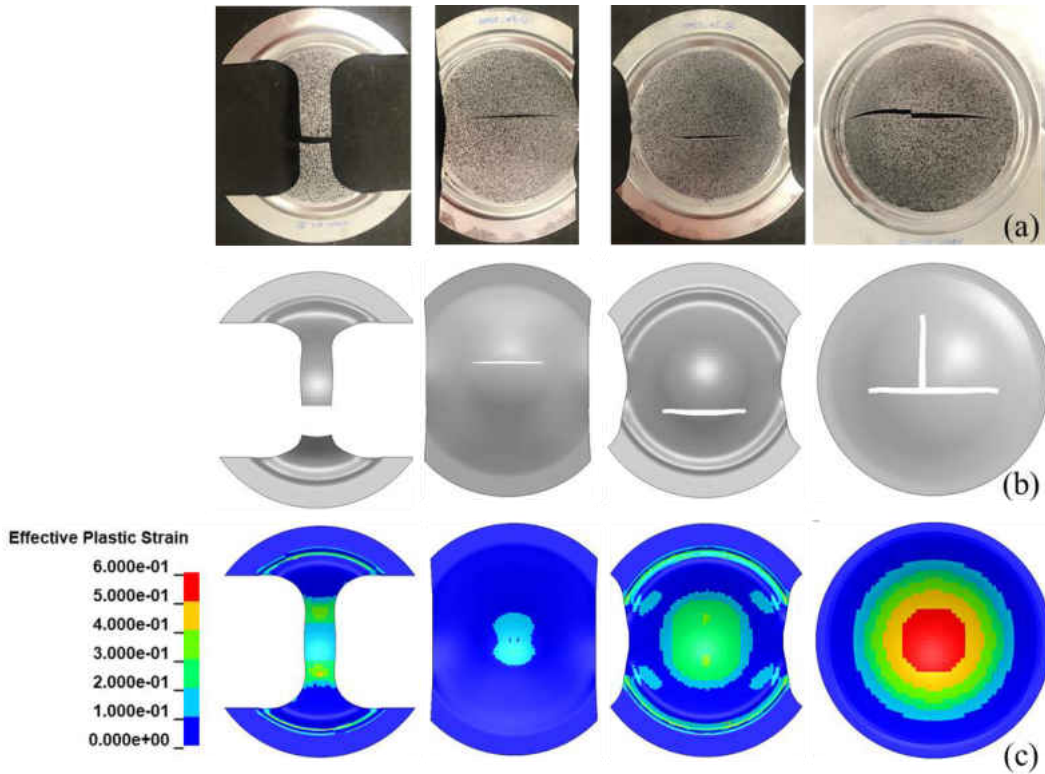


Figure 6-17. (a) Fracture samples in Nakazima Test (b) Fracture in FE simulations (c) Equivalent plastic strain contour plot before fracture

The three-point bending crash tests were used to demonstrate the application of ductile fracture modeling. Figure 6-18 shows the test and simulation results of three point bending samples with hat section. Two punch design was used: cylinder punch and cross punch. In the case of using cylinder punch, both the constant fracture strain criterion and the GISSMO predicted the same fracture locations as in the tests (Figure 6-18 (a)). The advantage of GISSMO is demonstrated in Figure 6-18 (b) using the cross-punch design. The fracture location was correctly predicted along the longitudinal direction. GISSMO covers a wide range of stress states which allow for failure prediction of complex loading conditions considering damage histories.

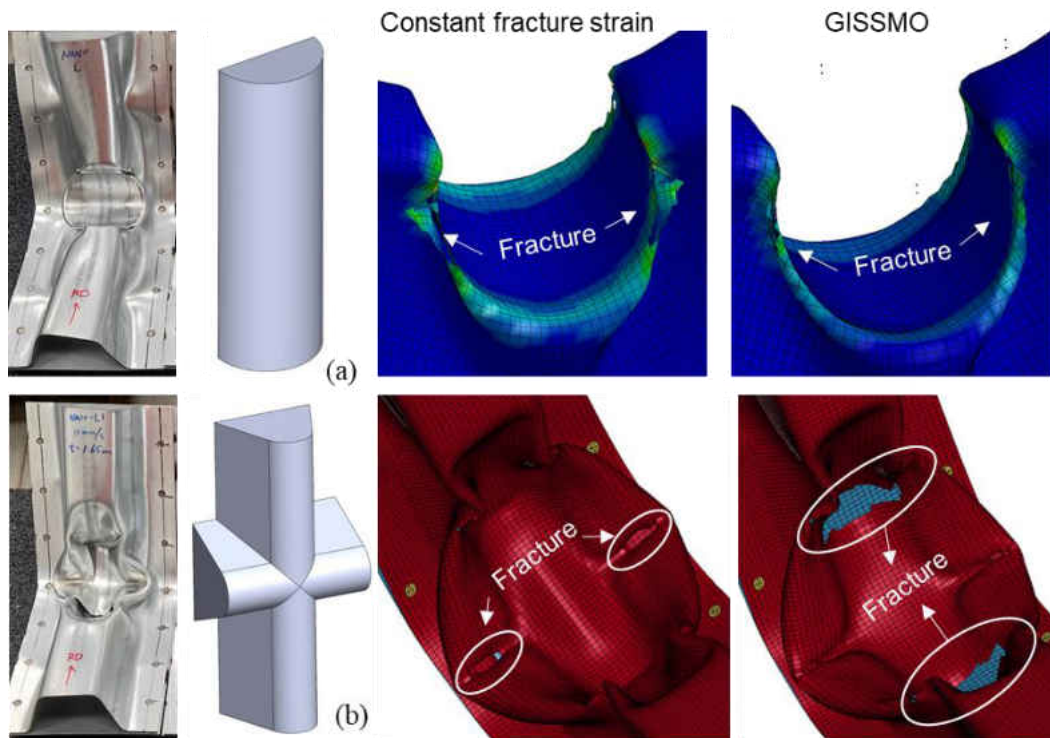


Figure 6-18. Three-point bending of hat section (a) using cylinder punch (b) using cross-punch. The different punch design demonstrates the use of GISSMO damage model for stress state dependent fracture modeling in LS-DYNA

CHAPTER 7 CONCLUSIONS AND FUTURE STUDIES

This work proposed a new modeling framework for solving anisotropic plasticity and anisotropic fracture problems under plane stress conditions, which offers simple and efficient solution for model calibration in the forming process design stage. The test results suggest strong anisotropic effect of 7075 aluminum alloy sheets only under uniaxial tension for both plasticity and fracture. The anisotropic plasticity was modeled by the Yld2000-2d yield function with flow stress correction by Lode angle dependence. A new all-strain based anisotropic fracture model eMMC-Srp was proposed based on the strain rate potential functions and the methodology of linear transformation. The FE simulation results demonstrate the capability of the current model.

Static and dynamic fracture tests were performed on AHSS sheets to investigate the strain rate effect on fracture under four loading conditions. The experimental results demonstrated that for the present material, significant ductility loss was observed for uniaxial tension, but strain rate effect on fracture appears to be insensitive for other loading conditions. The quasi-static MMC fracture model was extended to a fully uncoupled rate-dependent MMC fracture model $\bar{\epsilon}_f(\eta)g(\dot{\epsilon})$ and coupled rate-dependent MMC fracture model $\bar{\epsilon}_f(\eta)g(\dot{\epsilon}, \bar{\theta})$.

The FE simulations of orthogonal cutting using the Johnson-Cook fracture model explain that the works of plasticity, friction and separation are essentially uncoupled with formation of continuous chips. The simulations predicted quasi-linear relation between cutting force and depth of cut at large positive rake angles. The size of the highly deformed boundary layer is related to the fracture toughness. The associated plastic work within the boundary layers appears to be independent of chip thickness and rake angle over the range of investigation. The single shear

plane algebraic model gives satisfactory quantitative agreement with the shear angle, fracture toughness and shear yield stress as compared to the simulation results.

The material ductile fracture was investigated by real applications in formability and component tests. A new practical calibration approach of ductile fracture locus was introduced by square punch tests. The original stress based MMC fracture model was transformed into strain-based FFLD defined by principal strains under plane stress condition. The strain and damage evolution histories of the two critical locations in the square punch tests reveal that material experienced shear-induced fracture at the die entry and plane-strain tension dominated fracture at the corner of the punch radius. Shear failure was able to be predicted in which conventional FLD cannot tackle. The material models calibrated from coupon tests were also validated by Nakazima and three-point bending tests. The FE modeling results at component level testing demonstrate that the present ductile fracture modeling approach has significant benefits in predicting material formability and fracture by considering complex part loading conditions.

The following topics are suggested for future studies.

- Temperature effect in plasticity and fracture. The current study shed light on ductile fracture with strain rate effect under multi-axial stress state and contributes to a better understanding of the coupling effect between strain rate and stress state. At large deformation under high speed loading conditions, significant increase in temperature is induced by local plastic work, leading to thermal softening in material constitutive behavior. In this work, temperature effect was accounted by the strain rate effect and not discussed separately. Further investigation is recommended to explore the temperature effects on constitutive modeling and fracture analysis during dynamic loading events. This requires

an extra dimension of experimental test program under isothermal conditions and through investigation of temperature coupling/decoupling with strain rates and stress states.

- Anisotropic hardening. Most studies on anisotropic plasticity in the last few decades focus on developing anisotropic yield functions. Hardening is more critical to describe the plastic flow behavior under complex deformation path. The present solution provides a generalized anisotropic hardening framework under proportional loading conditions. More sophisticated constitutive models considering distortional hardening and Bauschinger effect under stress reversal conditions deserve further exploration.
- Size effect in ductile fracture modeling. The phenomenological ductile fracture models are developed from mechanical tests of small test coupons with FE simulation correlations using small mesh sizes (0.1-1 mm). Mesh size effect arises for modeling large deformation at large scales (mesh size > 5 mm) such as forming and crashworthiness simulations. Future research into the area of gradient plasticity theory may be useful for solving the problem of using shell elements.
- Statistical analysis for ductile fracture modeling. In order to account for the stochastic behavior of material fracture from the manufacturing processes, the probabilistic fracture limit band with safety margin levels are suggested rather than conventional fracture locus. An example work of statistical analysis of ductile fracture analysis using Gaussian and Weibull probability functions can be found from (Teng, Mae, Bai, & Wierzbicki, 2008). The uncertainty of fracture data from physical or DIC measurements can be also evaluated by the reliability of the fracture limit band from statistical analysis.

REFERENCES

- Abedini, A., Butcher, C., Rahmaan, T., & Worswick, M. J. (2018). Evaluation and calibration of anisotropic yield criteria in shear Loading: Constraints to eliminate numerical artefacts. *International Journal of Solids and Structures*, *151*, 118-134.
- Abedini, A., Butcher, C., & Worswick, M. J. (2017). Fracture characterization of rolled sheet alloys in shear loading: studies of specimen geometry, anisotropy, and rate sensitivity. *Experimental Mechanics*, *57*(1), 75-88.
- Arminjon, M., Bacroix, B., Imbault, D., & Raphanel, J. (1994). A fourth-order plastic potential for anisotropic metals and its analytical calculation from the texture function. *Acta Mechanica*, *107*(1-4), 33-51.
- Asad, M., Girardin, F., Mabrouki, T., & Rigal, J.-F. (2008). Dry cutting study of an aluminium alloy (A2024-T351): a numerical and experimental approach. *International Journal of Material Forming*, *1*(1), 499-502.
- Astakhov, V. P. (1998). *Metal cutting mechanics*: CRC press.
- Atkins, A. (1996). Fracture in forming. *Journal of Materials Processing Technology*, *56*(1-4), 609-618.
- Atkins, A. (2003). Modelling metal cutting using modern ductile fracture mechanics: quantitative explanations for some longstanding problems. *International Journal of Mechanical Sciences*, *45*(2), 373-396.
- Atkins, A. (2005). Toughness and cutting: a new way of simultaneously determining ductile fracture toughness and strength. *Engineering Fracture Mechanics*, *72*(6), 849-860.
- Atkins, T. (2009). *The science and engineering of cutting: the mechanics and processes of separating, scratching and puncturing biomaterials, metals and non-metals*: Butterworth-Heinemann.
- Atkins, T. (2015). Prediction of sticking and sliding lengths on the rake faces of tools using cutting forces. *International Journal of Mechanical Sciences*, *91*, 33-45.
- Bai, Y. (2007). Effect of loading history on necking and fracture. *PhD. Massachusetts Institute of Technology, Cambridge, USA*.
- Bai, Y., & Wierzbicki, T. (2008). A new model of metal plasticity and fracture with pressure and Lode dependence. *International journal of plasticity*, *24*(6), 1071-1096.

- Bai, Y., & Wierzbicki, T. (2010). Application of extended Mohr–Coulomb criterion to ductile fracture. *International Journal of Fracture*, *161*(1), 1.
- Bai, Y., & Wierzbicki, T. (2015). A comparative study of three groups of ductile fracture loci in the 3D space. *Engineering Fracture Mechanics*, *135*, 147-167.
- Bao, Y., & Wierzbicki, T. (2004). On fracture locus in the equivalent strain and stress triaxiality space. *International Journal of Mechanical Sciences*, *46*(1), 81-98.
- Bao, Y., & Wierzbicki, T. (2005). On the cut-off value of negative triaxiality for fracture. *Engineering Fracture Mechanics*, *72*(7), 1049-1069.
- Barge, M., Hamdi, H., Rech, J., & Bergheau, J.-M. (2005). Numerical modelling of orthogonal cutting: influence of numerical parameters. *Journal of Materials Processing Technology*, *164*, 1148-1153.
- Barlat, F., Aretz, H., Yoon, J. W., Karabin, M., Brem, J., & Dick, R. (2005). Linear transformation-based anisotropic yield functions. *International journal of plasticity*, *21*(5), 1009-1039.
- Barlat, F., Becker, R., Hayashida, Y., Maeda, Y., Yanagawa, M., Chung, K., . . . Murtha, S. (1997). Yielding description for solution strengthened aluminum alloys. *International journal of plasticity*, *13*(4), 385-401.
- Barlat, F., Brem, J., Yoon, J. W., Chung, K., Dick, R., Lege, D., . . . Chu, E. (2003). Plane stress yield function for aluminum alloy sheets—part 1: theory. *International journal of plasticity*, *19*(9), 1297-1319.
- Barlat, F., & Chung, K. (1993). Anisotropic potentials for plastically deforming metals. *Modelling and Simulation in Materials Science and Engineering*, *1*(4), 403.
- Barlat, F., & Chung, K. (2005). *Anisotropic strain rate potential for aluminum alloy plasticity*. Paper presented at the Proc. 8th ESAFORM Conference on Material Forming. Cluj-Napoca April.
- Barlat, F., Chung, K., & Richmond, O. (1993). Strain rate potential for metals and its application to minimum plastic work path calculations. *International journal of plasticity*, *9*(1), 51-63.
- Barlat, F., Gracio, J. J., Lee, M.-G., Rauch, E. F., & Vincze, G. (2011). An alternative to kinematic hardening in classical plasticity. *International journal of plasticity*, *27*(9), 1309-1327.

- Barlat, F., Ha, J., Grácio, J. J., Lee, M.-G., Rauch, E. F., & Vincze, G. (2013). Extension of homogeneous anisotropic hardening model to cross-loading with latent effects. *International journal of plasticity*, 46, 130-142.
- Barlat, F., Lege, D. J., & Brem, J. C. (1991). A six-component yield function for anisotropic materials. *International journal of plasticity*, 7(7), 693-712.
- Barlat, F., & Lian, K. (1989). Plastic behavior and stretchability of sheet metals. Part I: A yield function for orthotropic sheets under plane stress conditions. *International journal of plasticity*, 5(1), 51-66.
- Barlat, F., Maeda, Y., Chung, K., Yanagawa, M., Brem, J., Hayashida, Y., . . . Hattori, S. (1997). Yield function development for aluminum alloy sheets. *Journal of the Mechanics and Physics of Solids*, 45(11-12), 1727-1763.
- Barlat, F., Yoon, J. W., & Cazacu, O. (2007). On linear transformations of stress tensors for the description of plastic anisotropy. *International journal of plasticity*, 23(5), 876-896.
- Beese, A. M., Luo, M., Li, Y., Bai, Y., & Wierzbicki, T. (2010). Partially coupled anisotropic fracture model for aluminum sheets. *Engineering Fracture Mechanics*, 77(7), 1128-1152.
- Benson, D. J., & Okazawa, S. (2004). Contact in a multi-material Eulerian finite element formulation. *Computer methods in applied mechanics and engineering*, 193(39-41), 4277-4298.
- Carroll, J. T., & Strenkowski, J. S. (1988). Finite element models of orthogonal cutting with application to single point diamond turning. *International Journal of Mechanical Sciences*, 30(12), 899-920.
- Cazacu, O., Ionescu, I. R., & Yoon, J. W. (2010). Orthotropic strain rate potential for the description of anisotropy in tension and compression of metals. *International journal of plasticity*, 26(6), 887-904.
- Cazacu, O., Plunkett, B., & Barlat, F. (2006). Orthotropic yield criterion for hexagonal closed packed metals. *International journal of plasticity*, 22(7), 1171-1194.
- Ceretti, E., Fallböhmer, P., Wu, W., & Altan, T. (1996). Application of 2D FEM to chip formation in orthogonal cutting. *Journal of Materials Processing Technology*, 59(1-2), 169-180.
- Ceretti, E., Lucchi, M., & Altan, T. (1999). FEM simulation of orthogonal cutting: serrated chip formation. *Journal of Materials Processing Technology*, 95(1-3), 17-26.

- Childs, T. (2013). Ductile shear failure damage modelling and predicting built-up edge in steel machining. *Journal of Materials Processing Technology*, 213(11), 1954-1969.
- Childs, T. H., Maekawa, K., Obikawa, T., & Yamane, Y. (2000). *Metal machining: theory and applications*: Butterworth-Heinemann.
- Chung, K., Lee, S., Barlat, F., Keum, Y., & Park, J. (1996). Finite element simulation of sheet forming based on a planar anisotropic strain-rate potential. *International journal of plasticity*, 12(1), 93-115.
- Cook, N., Finnie, I., & Shaw, M. (1954). Discontinuous chip formation. *Trans. ASME*, 76(2), 153.
- Cottrell, A. (1964). *The Mechanical Properties of Matter*. In: Wiley, New York.
- Dirikolu, M., Childs, T., & Maekawa, K. (2001). Finite element simulation of chip flow in metal machining. *International Journal of Mechanical Sciences*, 43(11), 2699-2713.
- Ducobu, F., Rivière-Lorphèvre, E., & Filippi, E. (2014). Numerical contribution to the comprehension of saw-toothed Ti6Al4V chip formation in orthogonal cutting. *International Journal of Mechanical Sciences*, 81, 77-87.
- Ducobu, F., Rivière-Lorphèvre, E., & Filippi, E. (2015). On the introduction of adaptive mass scaling in a finite element model of Ti6Al4V orthogonal cutting. *Simulation Modelling Practice and Theory*, 53, 1-14.
- Dunand, M., & Mohr, D. (2017). Predicting the rate-dependent loading paths to fracture in advanced high strength steels using an extended mechanical threshold model. *International Journal of Impact Engineering*, 108, 272-285.
- Erice, B., Roth, C. C., & Mohr, D. (2018). Stress-state and strain-rate dependent ductile fracture of dual and complex phase steel. *Mechanics of Materials*, 116, 11-32.
- Fleck, N., Kang, K., & Williams, J. (1996). The machining of sintered bronze. *International Journal of Mechanical Sciences*, 38(2), 141-156.
- Gu, B., He, J., Li, S., & Lin, Z. (2020). Anisotropic fracture modeling of sheet metals: From in-plane to out-of-plane. *International Journal of Solids and Structures*, 182, 112-140.
- Gu, G., & Mohr, D. (2015). Anisotropic Hosford–Coulomb fracture initiation model: Theory and application. *Engineering Fracture Mechanics*, 147, 480-497.
- Ha, J., Baral, M., & Korkolis, Y. P. (2018). Plastic anisotropy and ductile fracture of bake-hardened AA6013 aluminum sheet. *International Journal of Solids and Structures*, 155, 123-139.

- Hashemi, J., Tseng, A., & Chou, P. (1994). Finite element modeling of segmental chip formation in high-speed orthogonal cutting. *Journal of materials engineering and performance*, 3(6), 712.
- Hill, R. (1948). *A theory of the yielding and plastic flow of anisotropic metals*. Paper presented at the Proceedings of the Royal Society of London. Series A. Mathematical and Physical Sciences.
- Hill, R. (1952). On discontinuous plastic states, with special reference to localized necking in thin sheets. *Journal of the Mechanics and Physics of Solids*, 1(1), 19-30.
- Hill, R. (1979). *Theoretical plasticity of textured aggregates*. Paper presented at the Mathematical Proceedings of the Cambridge Philosophical Society.
- Hill, R. (1987). Constitutive dual potentials in classical plasticity. *Journal of the Mechanics and Physics of Solids*, 35(1), 23-33.
- Hill, R. (1990). Constitutive modelling of orthotropic plasticity in sheet metals. *Journal of the Mechanics and Physics of Solids*, 38(3), 405-417.
- Hill, R. (1993). A user-friendly theory of orthotropic plasticity in sheet metals. *International Journal of Mechanical Sciences*, 35(1), 19-25.
- Hosford, W. (1972). A generalized isotropic yield criterion.
- Hua, J., & Shivpuri, R. (2004). Prediction of chip morphology and segmentation during the machining of titanium alloys. *Journal of Materials Processing Technology*, 150(1-2), 124-133.
- Huang, J., & Black, J. (1996). An evaluation of chip separation criteria for the FEM simulation of machining.
- Iwata, K., Osakada, K., & Terasaka, Y. (1984). Process modeling of orthogonal cutting by the rigid-plastic finite element method.
- Jia, Y., & Bai, Y. (2016a). Ductile fracture prediction for metal sheets using all-strain-based anisotropic eMMC model. *International Journal of Mechanical Sciences*, 115, 516-531.
- Jia, Y., & Bai, Y. (2016b). Experimental study on the mechanical properties of AZ31B-H24 magnesium alloy sheets under various loading conditions. *International Journal of Fracture*, 197(1), 25-48.
- Johnson, G. R., & Cook, W. H. (1983). *A constitutive model and data for metals subjected to large strains, high strain rates and high temperatures*. Paper presented at the Proceedings of the 7th International Symposium on Ballistics.

- Joshi, V., Dixit, P., & Jain, V. (1994). Viscoplastic analysis of metal cutting by finite element method. *International Journal of Machine Tools and Manufacture*, 34(4), 553-571.
- Karafillis, A., & Boyce, M. (1993). A general anisotropic yield criterion using bounds and a transformation weighting tensor. *Journal of the Mechanics and Physics of Solids*, 41(12), 1859-1886.
- Keeler, S., & Kimchi, M. (2015). *Advanced high-strength steels application guidelines V5: WorldAutoSteel*.
- Khan, A. S., & Liu, H. (2012). Strain rate and temperature dependent fracture criteria for isotropic and anisotropic metals. *International journal of plasticity*, 37, 1-15.
- Kim, D., Barlat, F., Bouvier, S., Rabahallah, M., Balan, T., & Chung, K. (2007). Non-quadratic anisotropic potentials based on linear transformation of plastic strain rate. *International journal of plasticity*, 23(8), 1380-1399.
- Kim, J. H., Lee, M.-G., Barlat, F., Wagoner, R., & Chung, K. (2008). An elasto-plastic constitutive model with plastic strain rate potentials for anisotropic cubic metals. *International journal of plasticity*, 24(12), 2298-2334.
- Kim, J. H., Sung, J. H., Piao, K., & Wagoner, R. (2011). The shear fracture of dual-phase steel. *International journal of plasticity*, 27(10), 1658-1676.
- Kim, K. W., Lee, W. Y., & Sin, H.-c. (1999). A finite element analysis for the characteristics of temperature and stress in micro-machining considering the size effect. *International Journal of Machine Tools and Manufacture*, 39(9), 1507-1524.
- Kim, K. W., Lee, W. Y., & Sin, H. C. (1999). A finite-element analysis of machining with the tool edge considered. *Journal of Materials Processing Technology*, 86(1-3), 45-55.
- Knott, J. F. (1973). *Fundamentals of fracture mechanics: Gruppo Italiano Frattura*.
- Kopalinsky, E., & Oxley, P. (1987). Predicting the effects of cold working on the machining characteristics of low carbon steels.
- Korkolis, Y. P., & Kyriakides, S. (2008a). Inflation and burst of aluminum tubes. Part II: an advanced yield function including deformation-induced anisotropy. *International journal of plasticity*, 24(9), 1625-1637.
- Korkolis, Y. P., & Kyriakides, S. (2008b). Inflation and burst of anisotropic aluminum tubes for hydroforming applications. *International journal of plasticity*, 24(3), 509-543.

- Lee, Y.-W., Woertz, J. C., & Wierzbicki, T. (2004). Fracture prediction of thin plates under hemi-spherical punch with calibration and experimental verification. *International Journal of Mechanical Sciences*, 46(5), 751-781.
- Lei, S., Shin, Y., & Incropera, F. (1999). Thermo-mechanical modeling of orthogonal machining process by finite element analysis. *International Journal of Machine Tools and Manufacture*, 39(5), 731-750.
- Leseur, D. (1999). *Experimental investigations of material models for Ti-6Al-4V and 2024-T3*. Retrieved from
- Li, K., Gao, X.-L., & Sutherland, J. (2002). Finite element simulation of the orthogonal metal cutting process for qualitative understanding of the effects of crater wear on the chip formation process. *Journal of Materials Processing Technology*, 127(3), 309-324.
- Li, S., He, J., Gu, B., Zeng, D., Xia, Z. C., Zhao, Y., & Lin, Z. (2018). Anisotropic fracture of advanced high strength steel sheets: Experiment and theory. *International journal of plasticity*, 103, 95-118.
- Li, Y., Luo, M., Gerlach, J., & Wierzbicki, T. (2010). Prediction of shear-induced fracture in sheet metal forming. *Journal of Materials Processing Technology*, 210(14), 1858-1869.
- Liang, R., & Khan, A. S. (1999). A critical review of experimental results and constitutive models for BCC and FCC metals over a wide range of strain rates and temperatures. *International journal of plasticity*, 15(9), 963-980.
- Lin, Z.-C., & Lo, S.-P. (2001). 2-D discontinuous chip cutting model by using strain energy density theory and elastic-plastic finite element method. *International Journal of Mechanical Sciences*, 43(2), 381-398.
- Lin, Z.-C., & Pan, W.-C. (1993). A thermoelastic-plastic large deformation model for orthogonal cutting with tool flank wear—Part I: Computational procedures. *International Journal of Mechanical Sciences*, 35(10), 829-840.
- Lin, Z., & Lin, S. (1992). A coupled finite element model of thermo-elastic-plastic large deformation for orthogonal cutting.
- Liu, J., Bai, Y., & Xu, C. (2014). Evaluation of ductile fracture models in finite element simulation of metal cutting processes. *Journal of Manufacturing Science and Engineering*, 136(1).
- Lo, S.-P. (2000). An analysis of cutting under different rake angles using the finite element method. *Journal of Materials Processing Technology*, 105(1-2), 143-151.

- Lou, Y., & Yoon, J. W. (2017). Anisotropic ductile fracture criterion based on linear transformation. *International journal of plasticity*, 93, 3-25.
- Lou, Y., Yoon, J. W., & Huh, H. (2014). Modeling of shear ductile fracture considering a changeable cut-off value for stress triaxiality. *International journal of plasticity*, 54, 56-80.
- Luo, M., Dunand, M., & Mohr, D. (2012). Experiments and modeling of anisotropic aluminum extrusions under multi-axial loading—Part II: Ductile fracture. *International journal of plasticity*, 32, 36-58.
- Mabrouki, T., Girardin, F., Asad, M., & Rigal, J.-F. (2008). Numerical and experimental study of dry cutting for an aeronautic aluminium alloy (A2024-T351). *International Journal of Machine Tools and Manufacture*, 48(11), 1187-1197.
- Mabrouki, T., & Rigal, J.-F. (2006). A contribution to a qualitative understanding of thermo-mechanical effects during chip formation in hard turning. *Journal of Materials Processing Technology*, 176(1-3), 214-221.
- Mamalis, A., Horvath, M., Branis, A., & Manolakos, D. (2001). Finite element simulation of chip formation in orthogonal metal cutting. *Journal of Materials Processing Technology*, 110(1), 19-27.
- Manual, L.-D. K. U. s. (2017). Vol. II Material Models. *Livermore Software Technology Corporation (LSTC), Darft, Livermore, CA, USA*.
- Marcadet, S. J., & Mohr, D. (2015). Effect of compression–tension loading reversal on the strain to fracture of dual phase steel sheets. *International journal of plasticity*, 72, 21-43.
- Marciniak, Z., & Kuczyński, K. (1967). Limit strains in the processes of stretch-forming sheet metal. *International Journal of Mechanical Sciences*, 9(9), 609-620.
- Marciniak, Z., Kuczyński, K., & Pokora, T. (1973). Influence of the plastic properties of a material on the forming limit diagram for sheet metal in tension. *International Journal of Mechanical Sciences*, 15(10), 789-800.
- Marusich, T., & Ortiz, M. (1995). Modelling and simulation of high-speed machining. *International Journal for Numerical Methods in Engineering*, 38(21), 3675-3694.
- McClain, B., Batzer, S. A., & Maldonado, G. I. (2002). A numeric investigation of the rake face stress distribution in orthogonal machining. *Journal of Materials Processing Technology*, 123(1), 114-119.

- Mohr, D., & Marcadet, S. J. (2015). Micromechanically-motivated phenomenological Hosford–Coulomb model for predicting ductile fracture initiation at low stress triaxialities. *International Journal of Solids and Structures*, 67, 40-55.
- Movahhedy, M., Gadala, M., & Altintas, Y. (2000). Simulation of the orthogonal metal cutting process using an arbitrary Lagrangian–Eulerian finite-element method. *Journal of Materials Processing Technology*, 103(2), 267-275.
- Ng, E.-G., El-Wardany, T. I., Dumitrescu, M., & Elbestawi, M. A. (2002). Physics-based simulation of high speed machining. *Machining science and technology*, 6(3), 301-329.
- Obikawa, T., & Usui, E. (1996). Computational machining of titanium alloy—finite element modeling and a few results.
- Ohbuchi, Y., & Obikawa, T. (2005). Adiabatic shear in chip formation with negative rake angle. *International Journal of Mechanical Sciences*, 47(9), 1377-1392.
- Olovsson, L., Nilsson, L., & Simonsson, K. (1999). An ALE formulation for the solution of two-dimensional metal cutting problems. *Computers & structures*, 72(4-5), 497-507.
- Özel, T. (2006). The influence of friction models on finite element simulations of machining. *International Journal of Machine Tools and Manufacture*, 46(5), 518-530.
- Pantalé, O., Bacaria, J.-L., Dalverny, O., Rakotomalala, R., & Caperaa, S. (2004). 2D and 3D numerical models of metal cutting with damage effects. *Computer methods in applied mechanics and engineering*, 193(39-41), 4383-4399.
- Park, N., Huh, H., Lim, S. J., Lou, Y., Kang, Y. S., & Seo, M. H. (2017). Fracture-based forming limit criteria for anisotropic materials in sheet metal forming. *International journal of plasticity*, 96, 1-35.
- Park, N., Huh, H., & Yoon, J. W. (2018). Anisotropic fracture forming limit diagram considering non-directionality of the equi-biaxial fracture strain. *International Journal of Solids and Structures*, 151, 181-194.
- Park, N., Stoughton, T. B., & Yoon, J. W. (2020). A new approach for fracture prediction considering general anisotropy of metal sheets. *International journal of plasticity*, 124, 199-225.
- Peirs, J., Verleysen, P., & Degrieck, J. (2012). Novel technique for static and dynamic shear testing of Ti6Al4V sheet. *Experimental Mechanics*, 52(7), 729-741.

- Rabahallah, M., Balan, T., Bouvier, S., Bacroix, B., Barlat, F., Chung, K., & Teodosiu, C. (2009). Parameter identification of advanced plastic strain rate potentials and impact on plastic anisotropy prediction. *International journal of plasticity*, 25(3), 491-512.
- Raczy, A., Elmadagli, M., Altenhof, W., & Alpas, A. (2004). An Eulerian finite-element model for determination of deformation state of a copper subjected to orthogonal cutting. *Metallurgical and materials transactions a*, 35(8), 2393-2400.
- Rahmaan, T., Abedini, A., Butcher, C., Pathak, N., & Worswick, M. J. (2017). Investigation into the shear stress, localization and fracture behaviour of DP600 and AA5182-O sheet metal alloys under elevated strain rates. *International Journal of Impact Engineering*, 108, 303-321.
- Rakotomalala, R., Joyot, P., & Touratier, M. (1993). Arbitrary Lagrangian-Eulerian thermomechanical finite-element model of material cutting. *Communications in Numerical Methods in Engineering*, 9(12), 975-987.
- Roth, C. C., & Mohr, D. (2014). Effect of strain rate on ductile fracture initiation in advanced high strength steel sheets: Experiments and modeling. *International journal of plasticity*, 56, 19-44.
- Rousselier, G., Barlat, F., & Yoon, J. W. (2009). A novel approach for anisotropic hardening modeling. Part I: Theory and its application to finite element analysis of deep drawing. *International journal of plasticity*, 25(12), 2383-2409.
- Rousselier, G., Barlat, F., & Yoon, J. W. (2010). A novel approach for anisotropic hardening modeling. Part II: Anisotropic hardening in proportional and non-proportional loadings, application to initially isotropic material. *International journal of plasticity*, 26(7), 1029-1049.
- Sasahara, H., Obikawa, T., & Shirakashi, T. (1996). FEM analysis of cutting sequence effect on mechanical characteristics in machined layer. *Journal of Materials Processing Technology*, 62(4), 448-453.
- Shaw, M. C., & Cookson, J. (2005). *Metal cutting principles* (Vol. 2): Oxford university press New York.
- Shet, C., & Deng, X. (2003). Residual stresses and strains in orthogonal metal cutting. *International Journal of Machine Tools and Manufacture*, 43(6), 573-587.
- Shi, G., Deng, X., & Shet, C. (2002). A finite element study of the effect of friction in orthogonal metal cutting. *Finite Elements in Analysis and Design*, 38(9), 863-883.

- Shih, A. J. (1995). Finite element analysis of the rake angle effects in orthogonal metal cutting. *International Journal of Mechanical Sciences*, 38(1), 1-17.
- Shih, A. J. (1996). Finite element analysis of orthogonal metal cutting mechanics. *International Journal of Machine Tools and Manufacture*, 36(2), 255-273.
- Shih, A. J., & Yang, H. T. (1993). Experimental and finite element predictions of residual stresses due to orthogonal metal cutting. *International Journal for Numerical Methods in Engineering*, 36(9), 1487-1507.
- Shirakashi, T., & Usui, E. (1974). *Simulation analysis of orthogonal metal cutting mechanism*. Paper presented at the Proceedings of the International Conference on Production Engineering.
- Soo, S., Aspinwall, D., & Dewes, R. (2004). 3D FE modelling of the cutting of Inconel 718. *Journal of Materials Processing Technology*, 150(1-2), 116-123.
- Steglich, D., Tian, X., Bohlen, J., & Kuwabara, T. (2014). Mechanical testing of thin sheet magnesium alloys in biaxial tension and uniaxial compression. *Experimental Mechanics*, 54(7), 1247-1258.
- Stephenson, D. A., & Agapiou, J. S. (2016). *Metal cutting theory and practice*: CRC press.
- Stoughton, T. B. (2002). A non-associated flow rule for sheet metal forming. *International journal of plasticity*, 18(5-6), 687-714.
- Stoughton, T. B., & Yoon, J. W. (2009). Anisotropic hardening and non-associated flow in proportional loading of sheet metals. *International journal of plasticity*, 25(9), 1777-1817.
- Stoughton, T. B., & Yoon, J. W. (2011). A new approach for failure criterion for sheet metals. *International journal of plasticity*, 27(3), 440-459.
- Strenkowski, J., & Athavale, S. (1997). A partially constrained Eulerian orthogonal cutting model for chip control tools.
- Sung, J. H., Kim, J. H., & Wagoner, R. (2010). A plastic constitutive equation incorporating strain, strain-rate, and temperature. *International journal of plasticity*, 26(12), 1746-1771.
- Swift, H. (1952). Plastic instability under plane stress. *Journal of the Mechanics and Physics of Solids*, 1(1), 1-18.
- Teng, X., Mae, H., Bai, Y., & Wierzbicki, T. (2008). Statistical analysis of ductile fracture properties of an aluminum casting. *Engineering Fracture Mechanics*, 75(15), 4610-4625.

- Teng, X., & Wierzbicki, T. (2006). Evaluation of six fracture models in high velocity perforation. *Engineering Fracture Mechanics*, 73(12), 1653-1678.
- Trent, E. M., & Wright, P. K. (2000). *Metal cutting*: Butterworth-Heinemann.
- Tvergaard, V., & Needleman, A. (1984). Analysis of the cup-cone fracture in a round tensile bar. *Acta metallurgica*, 32(1), 157-169.
- Tyan, T., & Yang, W. H. (1992). Analysis of orthogonal metal cutting processes. *International Journal for Numerical Methods in Engineering*, 34(1), 365-389.
- Usui, E., & Shirakashi, T. (1982). Mechanics of machining—from descriptive to predictive theory. *on the art of cutting metals-75 years later*, 7(1), 13-55.
- Vaz, M., Owen, D., Kalhori, V., Lundblad, M., & Lindgren, L.-E. (2007). Modelling and simulation of machining processes. *Archives of computational methods in engineering*, 14(2), 173-204.
- Wagoner, R. H., & Chenot, J.-L. (1996). *Fundamentals of metal forming*: John Wiley & Sons Inc.
- Walters, C. L. (2009). *Development of a punching technique for ductile fracture testing over a wide range of stress states and strain rates*. Massachusetts Institute of Technology,
- Wierzbicki, T., Bao, Y., Lee, Y.-W., & Bai, Y. (2005). Calibration and evaluation of seven fracture models. *International Journal of Mechanical Sciences*, 47(4-5), 719-743.
- Williams, J., Patel, Y., & Blackman, B. (2010). A fracture mechanics analysis of cutting and machining. *Engineering Fracture Mechanics*, 77(2), 293-308.
- Wu, J.-S., Dillon Jr, O., & Lu, W.-Y. (1996). Thermo-viscoplastic modeling of machining process using a mixed finite element method.
- Wyeth, D., & Atkins, A. (2009). Mixed mode fracture toughness as a separation parameter when cutting polymers. *Engineering Fracture Mechanics*, 76(18), 2690-2697.
- Yang, X., & Liu, C. R. (2002). A new stress-based model of friction behavior in machining and its significant impact on residual stresses computed by finite element method. *International Journal of Mechanical Sciences*, 44(4), 703-723.
- Yoon, J.-W., Barlat, F., Dick, R. E., Chung, K., & Kang, T. J. (2004). Plane stress yield function for aluminum alloy sheets—part II: FE formulation and its implementation. *International journal of plasticity*, 20(3), 495-522.

- Yoon, J. W., Song, I., Yang, D.-Y., Chung, K., & Barlat, F. (1995). Finite element method for sheet forming based on an anisotropic strain-rate potential and the convected coordinate system. *International Journal of Mechanical Sciences*, 37(7), 733-752.
- Zhang, B., & Bagchi, A. (1994). Finite element simulation of chip formation and comparison with machining experiment.
- Zhang, Y., Mabrouki, T., Nelias, D., & Gong, Y. (2011). Chip formation in orthogonal cutting considering interface limiting shear stress and damage evolution based on fracture energy approach. *Finite Elements in Analysis and Design*, 47(7), 850-863.